Dissertation

submitted to the

Combined Faculties for the Natural Sciences and for Mathematics

of the Ruperto-Carola University of Heidelberg, Germany

for the degree of

Doctor of Natural Sciences

presented by

Diplom-Phys. Thomas Walter Cornelius

born in: Mannheim

Oral examination: 5th July, 2006

FABRICATION AND CHARACTERISATION OF BISMUTH NANOWIRES

Referees: Prof. Dr. Reinhard Neumann

Prof. Dr. Annemarie Pucci

Zusammenfassung

Ein- und polykristalline Wismut-Nanodrähte wurden elektrochemisch in geätzten Ionenspurmembranen abgeschieden. Mittels konstanter Spannung hergestellte Drähte zeigen eine starke <110>-Textur. Diese ist umso stärker ausgeprägt, je geringer die Spannung und höher die Temperatur während der Abscheidung und je dünner die Poren sind. Mit Wechselspannung lassen sich <100>-texturierte Drähte herstellen, wobei diese Textur verstärkt wird für Abscheidungen mittels kürzerer Pulse und Anlegen eines höheren Anodenpotentials. Infrarotspektroskopie an einzelnen Nanodrähten zeigt eine Absorption, deren Kante mit abnehmendem Drahtdurchmesser blauverschoben wird. Als Ursache kommen Quanteneffekte in Frage, welche die direkte Bandlücke am L-Punkt der Brillouin-Zone vergrößern oder auch zusätzliche aus Defekten stammende Ladungszustände an der Drahtoberfläche, die die Plasmafrequenz erhöhen. Weiterhin wurden einzelne im Templat eingebettete Wismut-Nanodrähte elektrisch kontaktiert und ihr Widerstand als Funktion der Kristallinität und Temperatur charakterisiert. Die Messungen zeigen bestimmte spezifische elektrische Widerstände abhängig von der mittleren Korngröße. Untersuchungen des Widerstandes als Funktion der Temperatur demonstrieren, dass die Beweglichkeit der Ladungsträger bei tiefen Temperaturen, aufgrund von Streuprozessen an Korngrenzen, in Sättigung geht. Experimente an Vieldrahtproben bezüglich des elektrischen Widerstandes als Funktion des magnetischen Feldes zeigen einen ansteigenden Magnetwiderstand mit zunehmendem Drahtdurchmesser und wachsender Korngröße.

Abstract

Single- and polycrystalline bismuth nanowires were created by electrochemical deposition in ion track-etched polycarbonate membranes. Wires fabricated potentiostatically possess a strong <110> texture which becomes more pronounced for wires deposited at lower overpotentials, at higher temperatures, and in nanopores of smaller diameters. By applying reverse pulses, wires that are <100> textured can be grown where the texture increases for shorter pulses and higher anodic potentials. Infrared spectroscopic microscopy on single bismuth nanowires reveals an absorption whose onset is blueshifted with decreasing wire diameter. The observed effect may be attributed either to an increase of the direct band gap at the L-point of the Brillouin zone caused by quantum-size effects, or to a blueshift of the plasma frequency produced by surface defects acting as dopants. In addition, electrical resistance of single bismuth nanowires, embdedded in the template, has been measured as a function of both wire crystallinity and temperature. The results demonstrate that finite-size effects affect the wire resistivity which is higher than the bulk value and depends on the mean grain size. Measurements as a function of temperature demonstrate that the charge carrier mobility saturates at low temperatures because of electron scattering at grain boundaries, resulting in a non-monotonic resistance versus temperature behaviour. Further, measurements of the electrical resistance of wire arrays as a function of the magnetic field show a rising magnetoresistance with increasing diameter and growing mean grain size.

TABLE OF CONTENTS

Chapter I

INTRODUCTION

I.1 Motivation

Over the past decades the miniaturization of electronic devices has strongly influenced the technological evolution. Moore's law, for instance, which has been valid for the last three decades, states that roughly every eighteen months the number of transistors on an integrated circuit is doubled. The ongoing process requires a further reduction of feature sizes. The scaling down will change the performance of the components because their sizes become comparable to intrinsic length scales such as the electron mean free path and the Fermi wavelength. Speaking in a simplified manner, the former is the mean distance an electron can travel before being scattered. The latter is the de Broglie wavelength of electrons that travel with the Fermi velocity at the Fermi edge of a solid.

Nanostructured materials attract enormous interest due to both proceeding miniaturization and investigation of new physical phenomena. For more than half a century, researchers all over the world have been focusing on the properties of solid-state material whose size is in the same range as intrinsic length scales. From the 1930s on, mostly theoretical work has been performed on this topic [1, 2]. Later on, experiments on thin films as well as on whiskers have been undertaken and for about one decade also on nanowires. The latter are regarded as promising research objects due to their possible application for future devices in optoelectronics, as interconnects, biosensors [3], and field emitters [4, 5].

When the obejct size is comparable to the electronic mean free path l_e and Fermi wavelength λ_F, mesoscopic and quantum-size effects occur [6]. The former includes electron scattering at both wire surface and grain boundaries involving a higher specific electrical

resistivity than in bulk material. Analogously, the same behaviour is expected for phonons and hence for the thermal resistivity [7]. Due to size confinement of sufficiently small samples, a restricted number of phonons can be excited depending on their energy. Additionally, since the surface-to-volume ratio increases with decreasing object size, the surface becomes more important. For instance, metallic nanowires with diameter of few ten nanometers become thermally instable far below the melting point due to Rayleigh instability [8]. The wires fragment in order to minimize the surface energy, an effect that is rather important for future devices.

Nanowires, in particular bismuth nanowires, have been investigated intensively in recent years due to their remarkable transport properties and potential applications in future thermoelectric devices. Bi is an interesting material because both intrinsic length scales – $\lambda_F \sim$ 40 nm [9] and $l_e \sim 100$ nm at room temperature – are large compared to conventional metals, quantum size and mesoscopic effects are expected in wires of relatively large.

In most cases, bismuth nanowire arrays have been grown in pores of anodic aluminium oxide (AAO) templates by high-pressure injection [10, 11], vapour-phase deposition technique [12], and electrochemically [13, 14, 15]. Also, a low-temperature solvothermal process has been applied [16]. Single wires have been prepared by low-energy electron beam lithography using a shadow-mask technique [17], by electrochemical deposition in ion track-etched membranes [18], and by the so-called Taylor process. During the latter process, molten Bi is forced into glass capillaries which are subsequently heated up to the softening point of glass and then rapidly pulled [19]. Concerning the fabrication, both single-crystalline wires and the controlled growth of wires exhibiting various crystallinities has been aimed at, because the wire properties are a function of the inner structure as well as the crystalline direction. These wires have been characterized with regard to their electrical transport properties as a function of temperature and magnetic field [12, 13, 19, 20, 21, 22, 23, 24]. In the case of fabrication of wire arrays, either many wires were contacted while left embedded in the template, or the template was dissolved and, subsequently, single wires were contacted lithographically [25]. Both approaches have their respective advantages and disadvantages. In the literature, only very few experiments on single bismuth nanowires can be found. Furthermore, the thermoelectric power of Bi wires has been in the focus of theoretical [26] and experimental [27, 28] studies of recent years. Besides transport properties, the band structure of bismuth wires depending on the diameter has been investigated theoretically and experimentally where the experiments focused on infrared absorption and reflection spectroscopy [29, 30]. Some investigations also include doped bismuth wires, e.g. Sn and Te

doped bismuth [31, 32]. Additionally, wires of bismuth alloys such as $Bi_{1-x}Sb_x$ [33, 34] have been created and characterized.

The present work addresses the controlled fabrication of poly- and single-crystalline bismuth nanowires as well as the influence of wire size and morphology on the electrical transport and infrared absorption properties of single nanowires. Studies on single wires give access to absolute values which is impossible investigations on wire arrays. The wires are created by the template method employing ion track-etched polymer membranes [35, 36]. For this purpose, polymer films are irradiated by swift heavy ions which create latent tracks of a few nanometers in diameter. The tracks are chemically etched to pores and, subsequently, wires are deposited electrochemically into the nanopores. Earlier experiments with copper have shown that this technique allows the fabrication of poly- and single-crystalline copper nanowires [37].

I.2 The element bismuth

Bismuth is an element of the fifth group in the periodic table, thus possessing the following electronic configuration: [Xe] $4f^{14}$ $5d^{10}$ $6s^2$ $6p^3$, i.e. Bi has five valence electrons. In most cases it appears in chemical reactions as Bi^{3+}, in some rare cases also as Bi^{5+}. In nature it exists mostly as Bi_2S_3, Bi_2O_3, and in ore [38]. Bismuth has only one metastable isotope, $^{209}_{83}Bi$, whose halflife amounts to about 10^{19} years, i.e. about one million times longer than the age of the universe [39]. For our purposes it can be regarded as a stable element. Bismuth crystallizes in a rhombohedral lattice structure which belongs to the $R\bar{3}m$ space group with two atoms per unit cell. Alternatively, the structure can be described as hexagonal with six atoms per unit cell. The relation between these different unit cells is shown in Fig. 1 [40]. The dashed bold and thin lines indicate the rhombohedral and hexagonal unit cell, respectively. Directions in the bismuth crystal are specified with respect to three mutually perpendicular directions which are marked by C_1, C_2, and C_3; C_2 – one of the three axes of twofold symmetry (binary direction), C_3 – the axes of threefold symmetry (trigonal direction), C_1 – an axis perpendicular to C_2 and C_3 forming a right-hand triad in the order 1-2-3 (bisectrix direction). The trigonal direction of the rhombohedral structure is the c-axis of the hexagonal lattice.

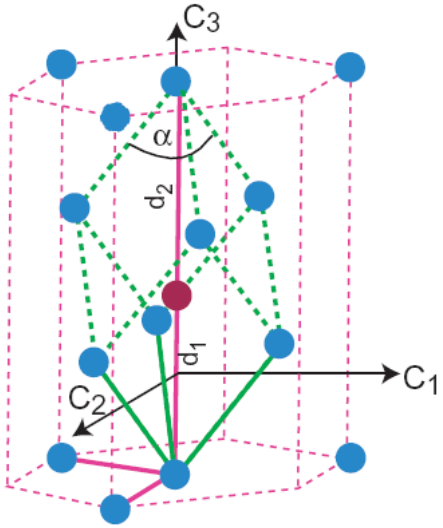

Figure 1: Schematic of the rhombohedral lattice structure (dashed bold lines) of bismuth belonging to space group $R\bar{3}m$ (taken from ref. [40]) together with the hexagonal unit cell (dashed thin lines). The solid bold and thin lines are the vectors spanning the rhombohedral and hexagonal lattice, respectively. C_1, C_2, and C_3 are the bisectrix, binary, and trigonal axes.

Melting and boiling temperatures of Bi are comparatively low, amounting to 271 and 1560 °C, respectively. Bismuth has a density of 9.8 g cm^{-3} and a specific thermal capacity of 0.122 J g^{-1} K^{-1} [41]. It exhibits highly anisotropic Fermi surfaces, and thus all transport properties (electrical and thermal conductivities) and the effective masses of charge carriers depend on the crystalline orientation. Both thermal and electrical conductivities of bulk Bi are small compared to metals. The specific electrical resistivity amounts to about 135 and 110 μΩ cm at 300 K parallel and normal to the trigonal axis, respectively. At room temperature the thermal conductivity is about 10 and 6 W m^{-1} K^{-1} parallel and perpendicular to the trigonal direction, respectively [42]. In order to characterize the transport properties of nanowires, their crystalline structure must be well defined. Therefore, wires of controlled crystallinity have to be fabricated.

The mean free path of electrons l_e amounts to 100 nm at room temperature and increases to 400 μm when cooling Bi down to 4 K [25]. When the wire diameter is in the same range as l_e, finite-size effects occur influencing the electric transport properties due to scattering processes of charge carriers at both wire surface and grain boundaries [2, 43]. Because of the large l_e, these effects are expected in Bi nanowires with diameter of few hundred nanometers. Moreover, the Fermi wavelength of the electrons amounts to about 40 nm with the consequence that quantum-size effects (QSE) may occur already in Bi wires with a diameter of ~ 100 nm. The appearance of QSE is enhanced in Bi by the very small electron effective mass m^* ranging from 0.001 to 0.3 m_e [44]. The holes exhibit larger masses of 0.06 - 0.6 m_e [26]. Bismuth possesses three electron pockets and one hole pocket which are located at the L- and at the T-point of the Brillouin zone, respectively. It is a semimetal with a small indirect band overlap and two direct band gaps at the L- and at the T- point of the Brillouin zone. Due to the small band overlap, the charge carrier density is four to five orders of magnitude smaller than in metals, amounting to $3*10^{18}$ and $3*10^{17}$ cm^{-3} at 300 and 4 K, respectively. On one hand, it has been predicted that this band overlap decreases and existing direct band gaps increase with diminishing specimen size. This involves a semimetal-to-semiconductor transition for films and wires of sufficiently small thickness and diameter, respectively [45]. This transition is assumed to take place at 77 K for nanowires of diameter d = 45, 44, 33 and 20 nm oriented along $[10\bar{1}1]$, bisectrix, trigonal and binary axis, respectively [26]. On the other hand, studies on thin films suggested that additional surface charge states, whose number increases with diminishing thickness, increase the charge carrier density, and may inhibit the observation of this transition [46].

Bi possesses a high thermopower making it a suitable candidate for novel future thermoelectric (TE) applications. TE devices are employed for the direct conversion of heat into electrical energy. They can be used for power generation and/or for refrigeration. The efficiency of such a TE device is expressed by the dimensionless figure of merit ZT which is a function of the Seebeck coefficient S (also called thermopower), the absolute temperature T, the thermal conductivity κ, and the electrical conductivity σ [47]:

$$ZT = S^2 T \frac{\sigma}{\kappa} \qquad \textbf{(1)}$$

The Seebeck coefficient amounts to about -100 and -50 μV K^{-1} in bulk Bi at room temperature parallel and normal to the trigonal direction. Since the transport properties (κ, σ, S) are a function of the crystalline direction, the same is true for ZT where the figure of merit is highest along the trigonal axes [42]. The state-of-the-art thermoelectric materials are semiconductor alloys, based for instance on Bi_2Te_3 with S = 220 μV/K and Z = 0.003, i.e. ZT ~ 1 at room temperature [48]. In order to improve the figure of merit, both Seebeck coefficient and specific electrical conductivity should be increased while the specific thermal conductivity should be diminished. As the characterization length of materials is reduced to be comparable with the wavelength of electrons, the motion of carriers (electrons or holes) is confined within one direction, leading to a change in the shape of the electronic density of states $D(E)$. In contrast to the parabolic shape of $D(E)$ for bulk materials, the spike-like shape of $D(E)$ for one-dimensional materials, e.g. nanowires, implies states whose electronic density near the Fermi level increases, resulting in an increased thermal power factor $S^2\sigma$. The thermal conductivity is composed by contributions from both phonons and charge carriers. It is theoretically predicted that ZT may be enhanced to ~ 6 for 5-nm wide Bi nanowires being n-doped to 10^{18} electrons cm^{-3} and oriented along the trigonal axis [26].

Chapter II

NANOWIRE FABRICATION

Ion track-etched polymer membranes are employed as templates for the fabrication of nanowires. In a first step, polymer films are irradiated by heavy ions. The damage zones (called latent tracks) are then etched chemically. Subsequently, bismuth is deposited electrochemically into the nanopores. This technique is known as template-based method.

II.1 Heavy ion irradiation

In the present work, polymer foils of thickness 30 μm are irradiated by heavy ions such as ^{197}Au, ^{206}Pb, and ^{238}U. The ions are highly positively charged and are accelerated up to 11.4 MeV per nucleon (MeV/u) in the UNILAC linear accelerator of GSI. The ion fluence applied is varied from a single ion per sample to up to 10^9 ions per cm^2. When charged particles penetrate a solid, they lose their energy by various interaction processes with the target:

- bremsstrahlung
- Cherenkov radiation
- electronic energy loss
- nuclear energy loss

For heavy ions with specific energies of several MeV/u, no bremsstrahlung occurs, due to the large mass of the ion. Also, Cherenkov radiation is negligible since the ion velocity is about 5 % of the velocity of light, thus excluding relativistic effects. The most dominant contribution results from Coulomb interaction between the ions and the target material. The interaction cross-section is a function of the ion velocity. At low ion velocities (≤ 0.01 MeV/u), the interaction is dominated by elastic collissions between the projectile and the target atoms (nuclear energy loss). For larger velocities (> 0.1 MeV/u) electronic excitation and ionization processes are dominant (electronic energy loss) which are described by the Bethe-Bloch formula [49]

$$\frac{dE}{dx} = \frac{4\pi \cdot e^2 \cdot Z_{eff}^2 \cdot Z_t \cdot N}{m_e \cdot v^2}\left[\ln\left(\frac{2m_e \cdot c^2 \cdot \beta^2}{I}\right) - \beta^2 - \delta - U\right]$$

$$\frac{dE}{dx} \propto \frac{Z_{eff}^2}{E} \cdot \ln\left(\frac{E}{I}\right) \qquad \textbf{(2)}$$

where e is the elementary charge, m_e the electron mass, Z_{eff} the effective charge of the projectile, Z_t the atomic number, N the density of the target atoms, I the ionisation energy, v the ion velocity, β the ion velocity with respect to the velocity of light c, δ a term correcting for relativistic effects, and U takes into account the influence of the electrons in inner atomic shells which do not contribute to the process.

After entering the target, the ion may either capture or loose electrons depending on its velocity compared to the orbital velocity of the electrons. This leads to a change of the charge state making it necessary to use an effective charge Z_{eff} being a function of the ion velocity and the atomic number [50].

$$Z_{eff} = Z\left[1 - \exp\left(-\frac{130\beta}{Z^{2/3}}\right)\right] \qquad \textbf{(3)}$$

At high velocities $Z_{eff} \approx Z$, while the lower β is the smaller becomes the net positive charge of the incident ion.

The energy loss of uranium ions in polycarbonate as a function of the specific energy calculated by means of the SRIM2003 code [51] is displayed in Fig. 2(a). The solid curve

represents the total energy loss while the dashed and dotted curves illustrate the nuclear and electronic energy loss, respectively.

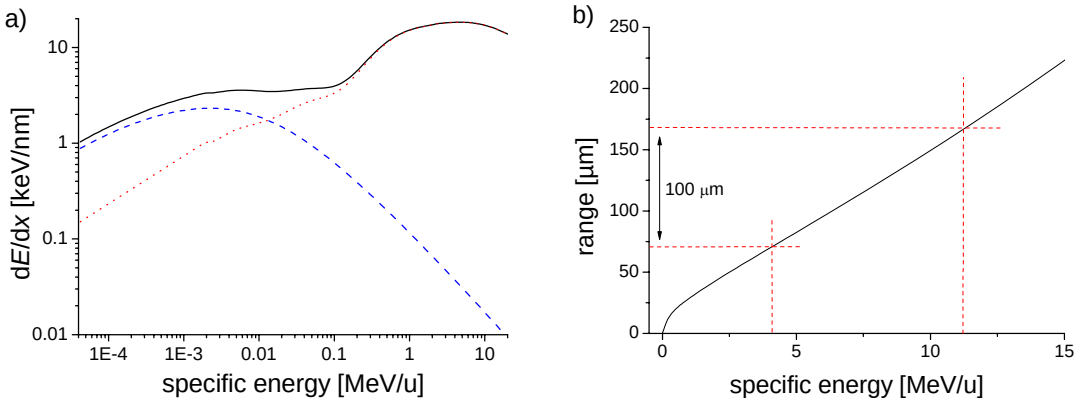

Figure 2: a) Energy loss and b) range of uranium ions in polycarbonate as a function of the specific kinetic energy calculated by using the SRIM2003 code [51].

The ion range is determined by the initial kinetic energy E_0 and the energy loss dE/dx as expressed by the following integral:

$$R = \int_0^{E_0} \left(\frac{dE}{dx} \right)^{-1} dE \qquad \textbf{(4)}$$

Heavy ions with initial specific kinetic energy of 11.4 MeV/u, as they are used at the UNILAC, have a projected range of about 170 µm in polycarbonate. After passing through 100 µm PC the remaining specific energy is still 4.2 MeV/u (Fig. 2(b)). The energy transfer per ion-path unit is rather constant of about 18 keV/nm (Fig. 2(a)). Since the energy loss is radially isotropic around the ion trajectory, a constant dE/dx involves a cylindrical volume surrounding the ion trajectory in which the structure of the solid is more or less strongly damaged. This damage zone is named latent track.

In polymers, the electronic excitation and ionisation processes induced by the incident ions lead predominantly to the destruction of chemical bonds (degradation) [52, 53], modification by the creation of unsaturated bonds, and amorphisation in the case of semi-crystalline material. Small volatile fragments can outgas causing a reduction of the mass density in the track [54, 55].

II.2 Chemical etching of latent tracks

In order to create pores, the latent-track material is removed selectively by means of an etching solution. The process can be described by the competition of the etch rates occurring along the latent track and isotropically at the non-irradiated bulk material, as displayed schematically in Fig. 3. The corresponding etch velocities are called track- and bulk-etching rates (v_T and v_B). The resulting pore shape depends on the ratio of these two etching velocities. In case the track etching rate is much higher than the bulk etching rate, the resulting pore can be treated as cylindrical, whereas it becomes the more conical the smaller the etching rate ratio is. The opening angle α of the cone is given by

$$\alpha = \arctan\left(\frac{v_B}{v_T}\right) \qquad \textbf{(5)}$$

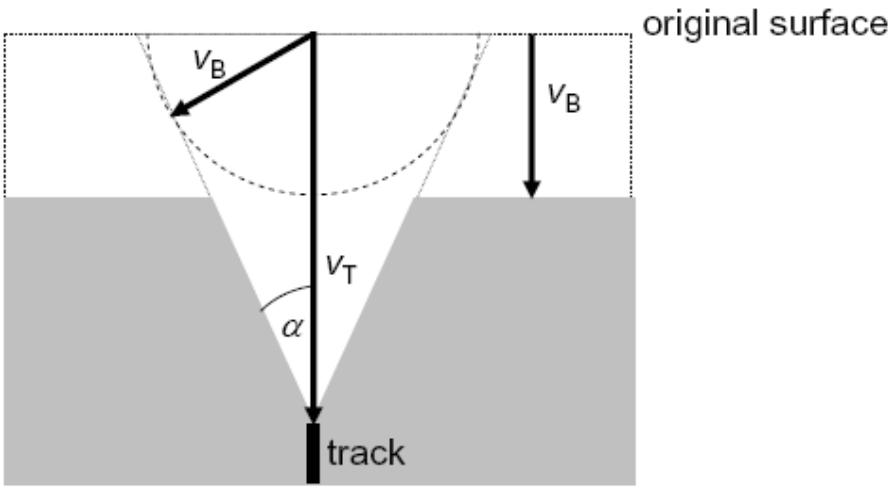

Figure 3: Schematic of bulk- and track-etching rate (v_B and v_T).

Taking advantage of various etching velocity ratios by employing different etchants and by etching either from one or both sides of the polymer foil, diverse pore shapes can be obtained as illustrated in Fig. 4. In this layout cylindrical (a), conical (b), bi-conical (c), and funnel-shaped pores (d) are depicted.

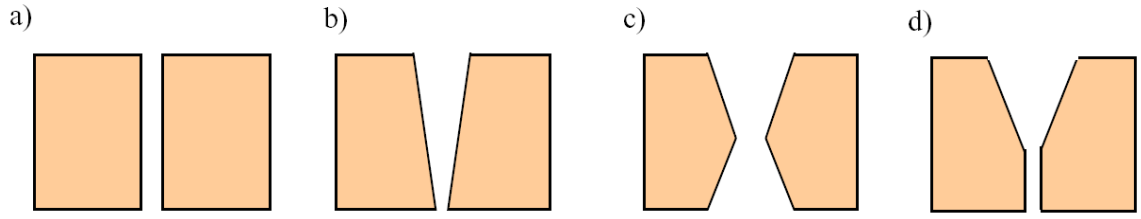

Figure 4: Variation of the etching parameters allows the generation of different pore shapes: a) cylindrical, b) conical, c) bi-conical, and d) funnel-shaped nanopore.

The ratio v_T/v_B is a function of both the ion used for the irradiation and the etching conditions (temperature, composition, and concentration of the etchant). A suitable etchant for tracks in polycarbonate (PC, Makrofol N) and polyethyleneterephthalate (PET, Hostaphan) foils is aqueous sodium hydroxide (NaOH) solution. All irradiated foils are treated by UV light prior to etching in order to increase v_T.

II.2.a Multi-pore membranes

Multi-track foils, i.e. membranes irradiated with a certain number of heavy ions per cm^2, are etched in a big beaker containing the etching solution which is stirred during the etching. In Fig. 5(a) and (b), a scanning electron microscopy image of two circular pores in a 30 µm polycarbonate membrane and the pore diameter versus etching time curve are displayed, respectively. The etching has been performed at 50 °C with 6 M NaOH. The radial etching rate amounts to about 13 nm/min being deduced from the slope of the linear fit.

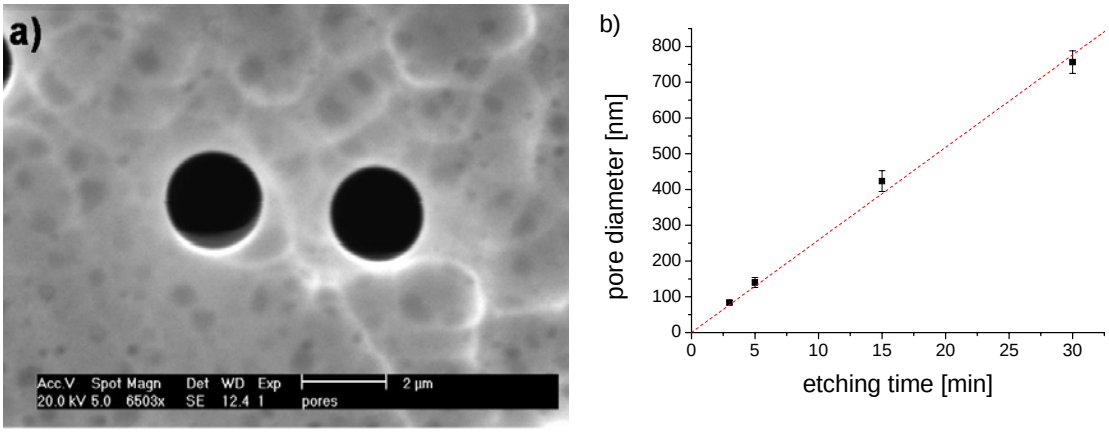

Figure 5: a) Scanning electron microscopy image of micropores created by chemical etching of latent tracks in polycarbonate (MAKROFOL N) employing 6 M NaOH at 50 °C. In order to image the pores by means of a SEM, a thin gold layer is sputtered on one side of the membrane. b) Pore diameter as a function of etching time.

II.2.b Single-pore membranes

Etching of single tracks is performed in a conductometric electrochemical cell which is presented schematically in Fig. 6. On both sides of the polymer membrane, the NaOH solution is introduced into the cell compartments. On each side a Au electrode is immersed, and a constant voltage of U = 400 mV is applied [56]. In order to avoid leakage currents, the cell is sealed by means of tightening a screw on one end of the cell.

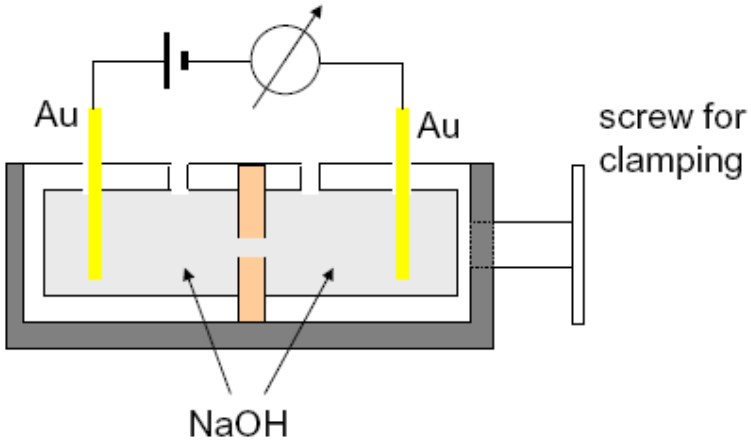

Figure 6: Scheme of a conductometric electrochemical cell for chemical etching of single latent tracks in polymer films.

During the etching procedure the current through the membrane is recorded. The effective pore diameter d_{eff} is determined assuming a cylindrical pore geometry, and using equation (6)

$$d_{eff} = \sqrt{\frac{4\,L\,I}{\pi\,\sigma\,U}} \qquad (6)$$

where L is the pore length, i.e. the foil thickness, I the measured current, U the applied voltage, and σ the specific conductivity of the etchant. It is presumed that the conductivity of the etchant is independent of the pore size, i.e. charges on the pore walls are neglected. Furthermore, it is assumed that the amount of etching products originating from a single track are insufficient to influence the etchant concentration. Additionally, the radial etching rate $\Delta r/\Delta t$ is calculated by differentiating the d_{eff}-t curve.

II.2.b.i Etching of single ion tracks

Conductometric etching of single tracks allows the monitoring of the pore evolution by recording the electric current as a function of etching time. Changes in etching rate with increasing pore diameter reflect the spatial distribution of chemical and physical modifications of the polymer. The recorded current versus time curve of the etching of a single track with 2 M NaOH at $T = 60$ °C, applying $U = 400$ mV is displayed in Fig. 7(a). The latent track was created by irradiation with a single Xe ion having a specific energy of 11.4 MeV/u. In part (b), the first ten minutes of the etching process are depicted. The corresponding calculated effective pore diameter and radial etching rate as a function of time are displayed in Figs. 7(c) and (d), respectively. During the etching process four different stages are observed:

I. The first one, in which no current is recorded, corresponds to the diffusion of the etchant in the latent track. As soon as an open channel through the membrane is established, a finite current is measured. This moment is denoted as break-through time $t_{b.t.}$, being marked by an arrow in Fig. 7(b). Here the radial etching rate $\Delta r/\Delta t$ "jumps" to a finite value, in this case ~ 3.9 nm/min.

II. The second stage is defined by a decrease of $\Delta r/\Delta t$ (Fig. 7(d)). The end of this decrease is taken as borderline to section III.

III. During this part the d_{eff}-vs-time curve shows a concave shape (Fig. 7(c)) where the radial etching rate recovers (Fig. 7(d)). The maximum $\Delta r/\Delta t$ is taken as the borderline between the third and fourth stage corresponding to the point of inflection of the d_{eff}-vs-time curve.

IV. During the last section $\Delta r/\Delta t$ decreases once more and reaches a constant value of about 1.7 nm/min which should in principle correspond to the bulk etch rate of the undamaged matrix.

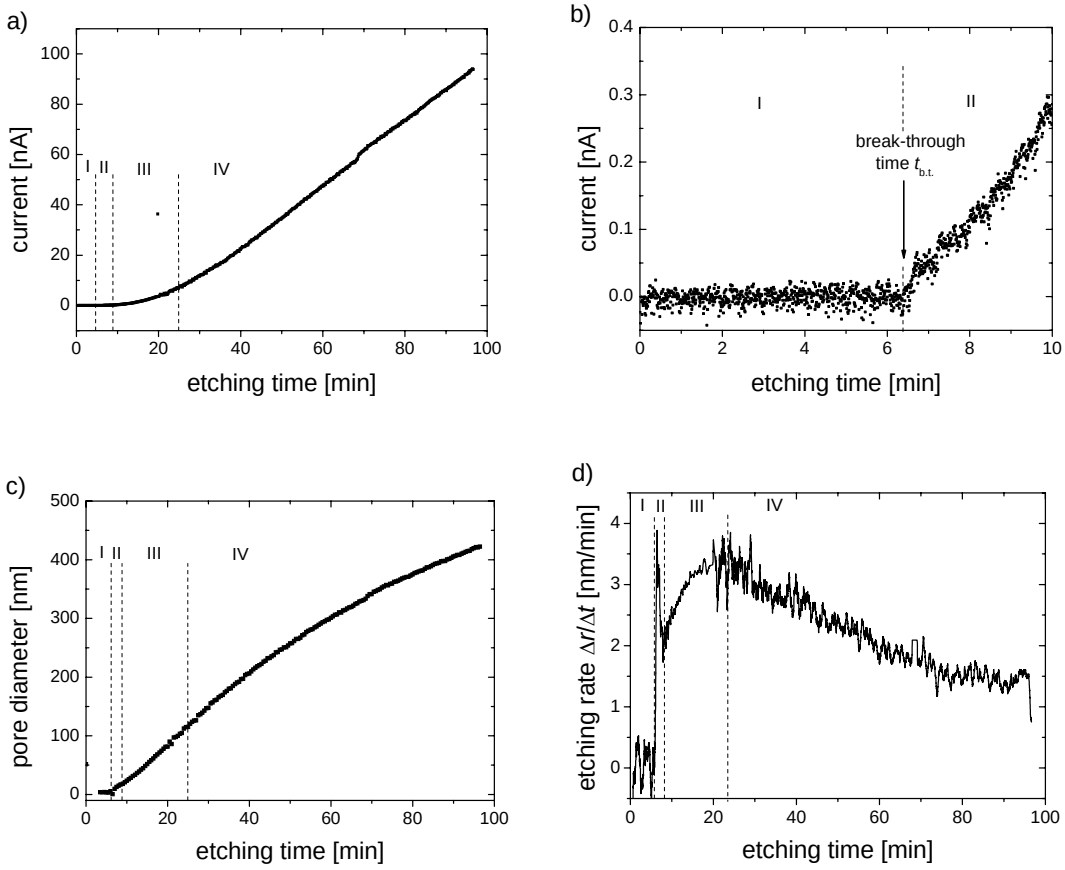

Figure 7: Chemical etching of a single latent track created by a Xe ion in MAKROFOL N employing 2 M NaOH at 60 °C and applying 400 mV. a) current, b) magnification of initial stage of part (a), c) effective pore diameter d_{eff}, and d) radial etching rate $\Delta r/\Delta t$ as a function of etching time.

The track-etching rate is derived by means of the following equation

$$v_T = \frac{D}{2t_{b.t.}} \tag{7}$$

where D is the membrane thickness. The factor ½ originates from the fact that the sample is etched simultaneously from both sides. The track-etching rate as a function of dE/dx for single tracks created by single Ni, Xe, and U ions with an initial specific energy of 11.4 MeV/u and etched in 2 M NaOH at 60 °C is displayed in Fig. 8. v_T increases with rising energy loss due to the higher damage along the ion trajectory. In the energy loss range of these investigations, the track-etching rate is directly proportional to dE/dx. The dashed line in Fig. 8 represents the best linear fit having a slope of 0.17 nm^2 eV^{-1} min^{-1}. Besides the dependence on the energy loss, v_T is also affected by the concentration and the temperature of

the etchant. The track-etching rate rises with both elevating temperature and increasing etchant concentration.

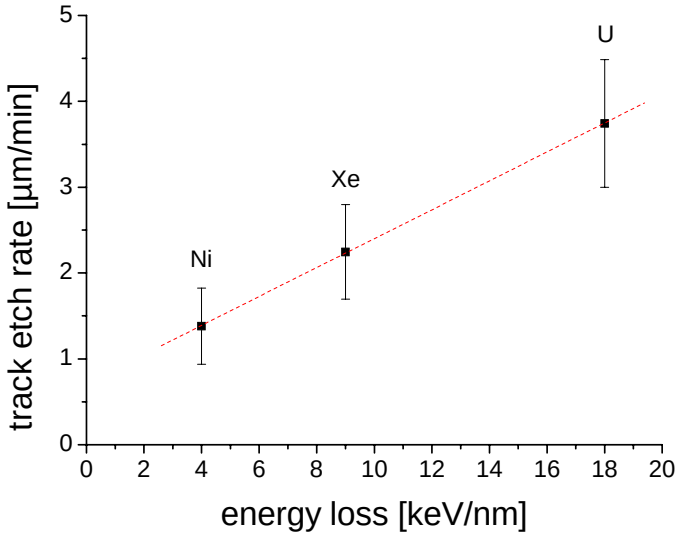

Figure 8: Track-etching rate as a function of the energy loss for single ion tracks in Makrofol N of thickness 30 µm etched in 2 M NaOH at 60 °C. The ions possess an initial specific energy of 11.4 MeV/u. The dashed line corresponds to the best linear fit.

Concerning the evolution of the nanopores during etching contradictory results can be found in the literature. For ion tracks in polycarbonate, the behavior of the local etch rate in the halo was found either similar or different to the results presented above. While Apel et al. [57] report the same etching behaviour as the present work, in Refs. [58] and [59] there is no indication for a reduced etching rate in the track halo. Most of these experiments were performed using alkaline etchants containing surfactants [60]. Surface-active substances are often used to improve wetting and obtain more uniform etching. However, it was shown that the presence of a surfactant significantly alters the shape of etching curves which might lead to wrong conclusions about the distribution of the damage in the tracks [61].

In principle, it is expected that at $t_{b.t.}$ the etching rate "jumps" to a finite value. The rapid dissolution is ascribed to the severe damage in the core of the track. It is supposed that the radial damage profile is proportional to the dose deposited by the incident ion scaling with $1/r^2$. That means that the radial etch rate is also expected to follow approximately a $1/r^2$ law. It is therefore surprising to see that in the stages II and III the radial etching rate exhibits a dip-like reduction. This behaviour is tentativley ascribed to a zone containing cross-linked polymer chains which hamper the chemical etching. At larger distances from the ion trajectory, the radial etch rate recovers indicating that the cross-linking process is limited to a

specific radius, i.e. dose range. Finally, the etching rate flattens and reach a constant value – the bulk-etching rate.

The decrease of $\Delta r/\Delta t$ observed in stage IV can be caused by at least three different effects:

1. It could be an artifact originating from polarisation of the Au electrodes. Polarisation can be avoided by applying an alternating potential. Apel et al. performed their measurements by applying an AC voltage with a frequency of 10 kHz and obtained similar results as in the present work [57]. Thus, electrode polarisation can be excluded.
2. It has been shown that the etching of polycarbonate is accompanied by compaction of the polymer [62]. The compaction hampers the diffusion of the etchant into the polymer foil, thus slowing down the etching process that involves the renewed decrease of the etching rate.
3. Dissolved polymer products originating from the etching process might change the etchant and thus influence the chemical etching. These waste products may either get stuck inside the nanopore, be adsorbed at the pore surface, or affect the etchant concentration, and thus alter the etching velocity. For instance, it has been found that the etching rate decreases when adding Bisphenol A to the etching solution because the molecules are adsorbed at the surface.

In conclusion, there are several indications that the radial etching rate is affected by the etchant concentration, the applied potential, and the energy loss but in general, the etching process is not fully understood yet. In order to illucidate both the spatial distribution of the polymer modifications surrounding the track and the evolution of the etching process in more detail, all parameters have to be varied in a systematic way.

II.2.b.ii Track-to-bulk etch velocity ratio of single tracks

The following histogram (Fig. 9) represents the track-to-bulk etch velocity ratio of single tracks in Makrofol N of thickness 30 µm created by different ions (Ni, Xe, U) with an initial specific energy of 11.4 MeV/u. The solid curves correspond to the respective best fits by a Gaussian. The etching is performed at 60 °C applying 400 mV in 2 M NaOH. In order to exclude any influences of waste products or electrode polarizations, the pores are rinsed immediately after etching and the effective pore diameter is determined by means of a 1 M KCl solution (σ = 10 S m^{-1} at 20 °C). On both sides of the membrane, the potassium chloride

solution and a Ag/AgCl electrode is introduced, and a constant potential U = 2 V is applied. The effective pore diameter is calculated using equation (6). The track- and bulk-etch velocities are derived from the break-through time during the etching process and from the pore diameter determined by the KCl measurement, respectively. The mean v_T/v_B, which is indicated by dashed lines in Fig. 9, increases from 420 to 820, and further to 1270 for Ni, Xe, and U ions, respectively. The corresponding standard deviations amount to 62, 90, and 150. The rise of the etching velocity ratio with increasing ion mass is ascribed to a higher electronic energy loss which involves a more severe damage inside the latent tracks. The higher v_T/v_B implies that the resulting pores are the more cylindrical the heavier the ion used for irradiation. Note that the ratio amounts to a few hundred even for Ni irradiated samples indicating that the pores exhibit an opening angle of less than 0.3°, i.e. they can be regarded as cylindrical.

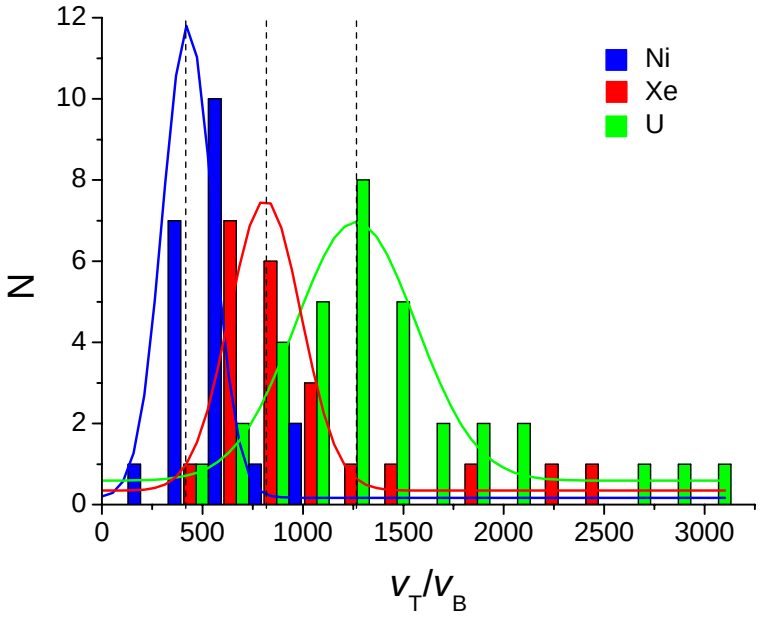

Figure 9: Histogram of etching velocitiy ratio v_T/v_B for single tracks in MAKROFOL N of thickness 30 µm etched in 2 M NaOH at 60 °C and 400 mV. The irradiation was performed with single Ni, Xe, and U ions of 11.4 MeV/u. The curves correspond to the respective best fits by a Gaussian. The dashed lines indicate the mean v_T/v_B ratio for the different irradiations.

II.3 Electrochemical wire growth

Galvanic depositions are based on standard potentials of metal ions and electrodes. In the cathodic part of the reaction, metal ions are reduced and deposited on the electrode, whereas the anode is dissolved and metal ions go into solution. By electrochemical deposition in pores, the ions pass through the pores and are reduced at the cathode on the other side of the pore. Thus, metal is deposited inside the pore forming a wire.

II.3.a Experimental setup for electrochemical wire fabrication

In order to deposit nanowires electrochemically in the etched nanopores, one side of the membrane is covered by a conductive layer (Fig. 10(a)). Therefore, a gold film of thickness 100 to 200 nm is sputtered on one side of the polymer foil by means of an Edwards Sputter Coater. The Au layer is contacted by a copper ring. Both, to ensure that the pores are completely closed on one end and for mechanical stabilisation of the membrane, an additional copper layer of a thickness of several micrometers is deposited electrochemically on the gold film. The electrochemical deposition of the copper layer as well as the subsequent fabrication of the nanowires is performed in an electrochemical cell, depicted schematically in Figs. 10(d) and (e), respectively. A copper and a bismuth rod are used as anodes. The Cu layer deposition is carried out at room temperature, applying a constant voltage of -500 mV, and using a commercial electrolytic copper bath Cupatierbad (Riedel company). During this deposition, a 1 % HCl solution is introduced into the compartment on the opposite side of the membrane.

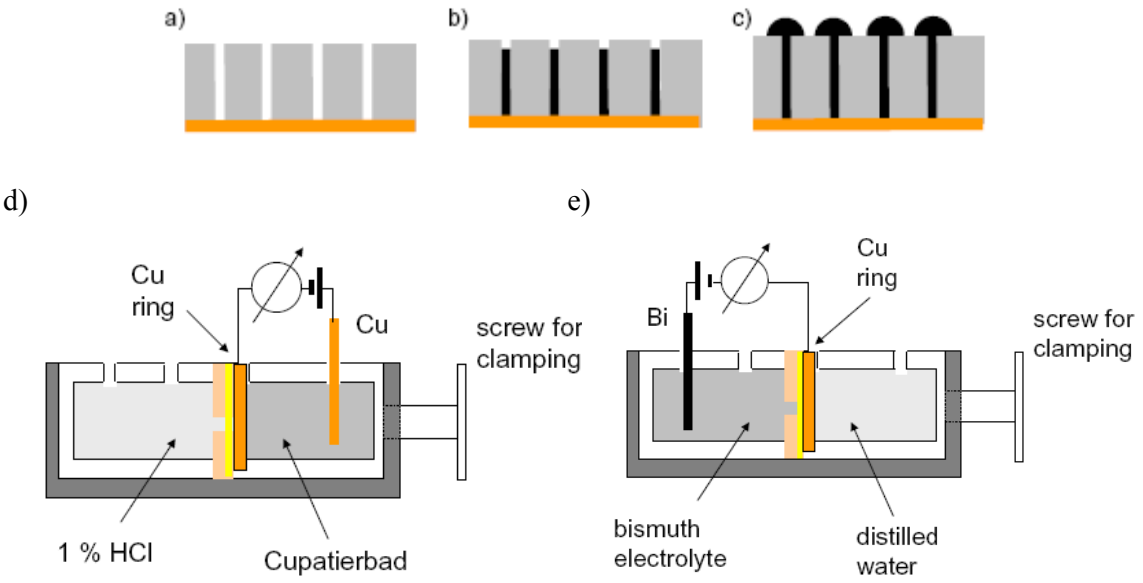

Figure 10: Schematics of the template-based method for nanowire fabrication: a) polymer membrane having nanopores covered by a conductive layer build up by Au and Cu, b) electrochemical deposition of metal inside the nanopores, and c) cap growth on top of the wires. d) and e) display the experimental setup for depositing the backing layer and the nanowires, respectively.

After depositing the Cu layer, the copper electrolyte and HCl solutions are exchanged by distilled water and the Bi electrolyte, respectively. Before deposition, the beaker containing the Bi electrolyte is evacuated to several millibars in order to reduce the air inside the electrolyte and minimize the risk that an air bubble may block nanopores. According to Dobrev et al. [63] a Bi solution containing following ingredients is used:

- 0.2 mol/l NaCl
- 1.1 mol/l glycerol
- 0.3 mol/l tartaric acid
- 1.3 mol/l HCl
- 0.2 mol/l $BiCl_3$

The purposes of these ingredients are [64]:

- NaCl promotes the deposition in $BiCl_3$ electrolytes.
- Glycerol facilitates smooth depositions in bismuth chloride solutions.
- HCl prevents the passivation of the Bi anode.

II.3.b Electrochemical deposition of bismuth nanowires

Bismuth is deposited into the nanopores (Fig. 10(b)) at constant temperature and applying both constant (DC) and alternating voltage (AC). In Fig. 11(a) and (b), the recorded deposition current versus time during fabrication of a multi-wire and a single-wire sample is displayed, respectively. The *I*-*t*-curves exhibit three sections: (I) at the very beginning of the deposition, a current peak is observed that is in the case of a single wire much less pronounced than for arrays. When introducing an electrode into an aqueous solution, there will be an exchange of metal ions at the metal-solution interface. Some metal ions leave the lattice structure of the electrode while some ions from the solution enter the crystal lattice. The simplest model of the metal-ion interface is the Helmholtz double layer which consists of two equal and opposite layers of charges - one on the metal and the other in the solution. This double layer is equivalent to a parallel plate capacitor. The layer in the solution is lined up at a fixed distance being determined by the hydration sphere of hydrated ions [65]. The current peak at the deposition beginning originates from this electrical double layer at the metal-electrolyte interface which is discharged during the very first seconds of the deposition. In a few cases, instead of the current peak a plateau is observed whose length in time varies. This plateau originates most probably from a bad adhesion of the backing layer. As a consequence, a cave may have formed in between the conductive layer and the membrane which is filled during the very beginning of the deposition process. Subsequently, the deposition current remains constant for a longer period of time (II), until it starts to increase and finally saturates (III). In the case of potentiostatic depositions the current density j, i.e., current per area ($j = I/A$), is constant. Therefore, a steady current is recorded during deposition in cylindrical pores. The deposition current for single wires of diameter few hundred nanometers amounts to less than 100 pA. As soon as the metal reaches the opposite side of the membrane and the deposition process is not any longer constricted by the pore geometry, a cap is formed on top of the wire (Fig. 10(c)). The start of the cap growth becomes apparent by a significant increase of the current due to both the larger deposition area during the cap formation and the constant current density. This current rise is much more pronounced for single-wire depositions where the current increases by three to four orders of magnitude within less than a minute (see inset of Fig. 11(b)). Since the current is a function of the deposition area, the current gain indicates that the size of the cap grown on top of a single wire is up to hundred times larger than the wire diameter, i.e., of the order of 10 μm for a 100 nm wire.

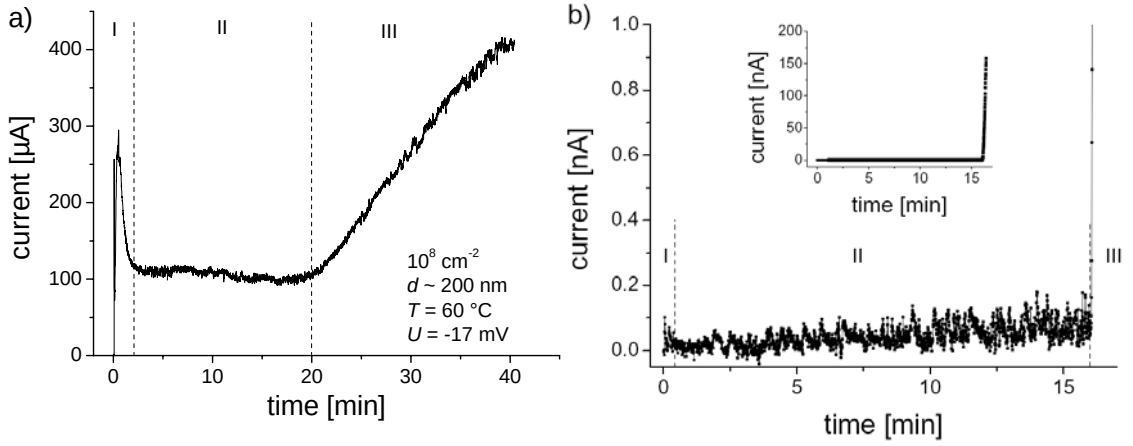

Figure 11: Deposition current as a function of time for electrochemical fabrication of bismuth nanowires. a) Deposition in a template possessing a pore density of 10^8 cm^{-2} with diameter 200 nm applying -17 mV at 60 °C. b) Single wire deposition in a pore with diameter 360 nm at 50 °C and -25 mV. The inset shows the complete *I*(*t*) curve.

Figure 12 displays the current versus deposition time for various potentials. The depositions are performed in polycarbonate membranes that were irradiated by 10^9 ions per cm^2 and subsequently etched for 80 s in 6 M NaOH at 50 °C in a big beaker. The higher the potential is the shorter becomes the deposition time. In the case of the lowest potential (U = -17 mV), only a faint current increase is observable starting after ~ 70 min of deposition, while the current rises in the case of the highest overpotential (U = -50 mV) already after ~ 3 min. The deposition current rises from ~ 30 to ~ 400 µA, when increasing the potential from -17 to -50 mV. Thus, the current density increases with growing overpotential and induces a higher charge deposition rate. According to Faraday's law (equation (8a)) where Z is the ion charge, e the elementary charge, A the number of nucleons contained in the ion, and m_u the proton mass, charge Q is equivalent to the deposited mass m. Thus more mass is deposited at higher current densities in the same time leading to a faster growth of the nanowires. Hence, the time needed for growing a wire of certain size reduces with increasing overpotential. By integrating the area beneath the deposition current-versus-time curve before the start of the cap growth, the total amount of deposited charge and hence, by means of Faraday's law, the filled volume is obtained. In the case of multi-pore samples, the exact number of pores is uncertain and the electric field may vary across the sample leading to slight variations of the growth velocity. Thus, the exact number of fabricated wires cannot be determined but only the fraction of pore volume that is filled with metal. For single-pore membranes the calculation of the filled volume $V = \rho\pi r^2 l$ allows the computation of the diameter of the created wire and thus a control of the KCl measurement of the pore size. Within their uncertainties both values are in very good agreement.

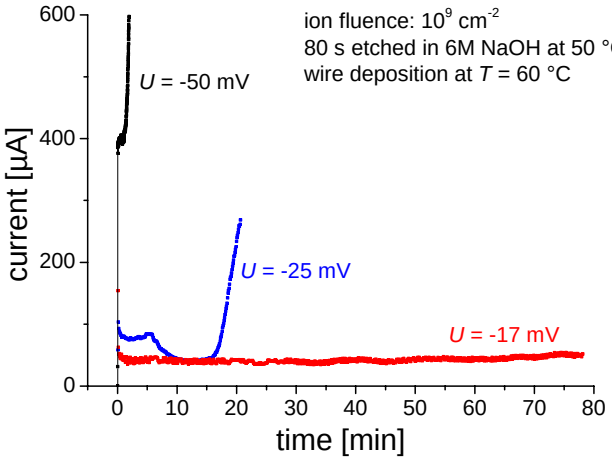

Figure 12: Deposition current as a function of time for electrochemical fabrication of bismuth nanowires applying various overpotentials at 60 °C.

$$Q = \int I \, dt = \frac{Z \cdot e}{A \cdot m_u} \cdot m \qquad \textbf{(8a)}$$

$$\text{for a single wire: } Q = \frac{Z \cdot e}{A \cdot m_u} \cdot \rho \cdot \pi \cdot r^2 \cdot l \qquad \textbf{(8b)}$$

Fig. 13(a) shows a detail of the deposition current-versus-time graph for wires fabricated by means of reverse pulses. As potential, square pulses of -20 and +10 mV with a length of 10 and 1 s, respectively, were applied. At each reversal of polarity, a negative or positive current peak is observed depending on whether an anodic or cathodic cycle started. Those peaks are caused by double layers which are discharged during each cycle. During reverse pulse depositions, metal is deposited during the cathodic cycle while it is partially dissolved again during the anodic one. By this method the amount of defects in the deposit can be reduced [66]. In order to clarify whether the same characteristics as for potentiostatic wire fabrication are valid for reverse pulse depositions, the recorded *I*-*t*-curve has been smoothed as displayed in Fig. 13(b). It is observed that the smoothed graph shows the same features as for potentiostatic depositions, namely a peak caused by the electric double layer, nearly constant deposition current, and a current increase originating from cap growth. Due to the partial dissolution in each cycle, the elapsed time before a cap starts to grow is longer than for potentiostatic depositions.

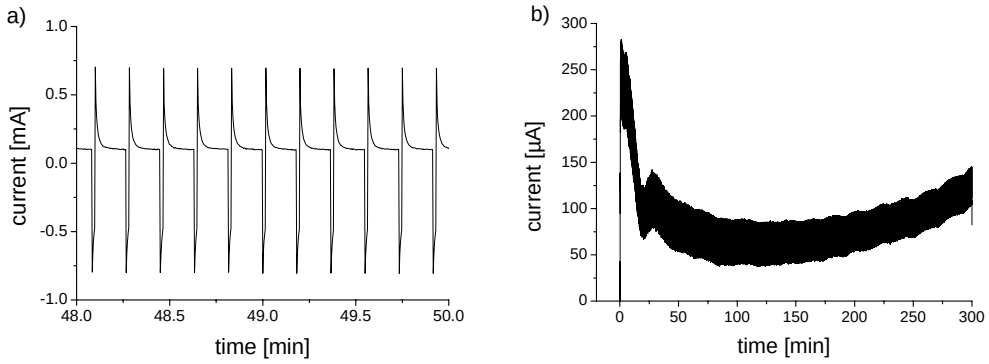

Figure 13: Current as a function of time for electrochemical deposition carried out with reverse pulses. a) Detail of the deposition curve that is shown in part b).

After wire deposition, the Bi electrolyte is replaced by a 1 % HCl solution in order to clean the sample surface. Rests of the electrolyte are dissolved in the HCl solution and, thus the sample is rinsed.

Figures 14(a) and (b) show scanning electron micropscopy images of Bi nanowires with a diameter of 150 and 800 nm, respectively. In the case of part (b) the sample is tilted by 20° in order to image the standing wires. The wires are grown in ion track-etched polycarbonate membranes that have been etched for 5 and 30 min, respectively. After depositing the wires, the template has been dissolved in dimethyformamide (DMF).

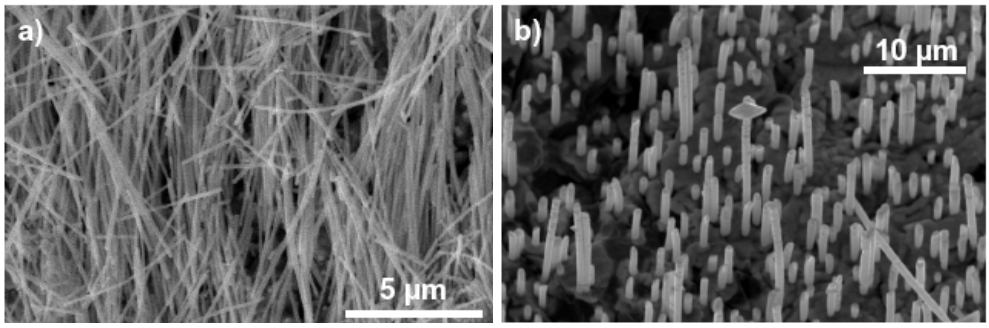

Figure 14: SEM images of bismuth nanowires of different diameter: a) *d* = 150 nm, b) *d* = 800 nm

A limiting factor of the deposition of single Bi nanowires is the hydrophobicity of the template material that hinders a liquid to penetrate into a nanopore. For instance, the thinnest single nanowire deposited in polycarbonate (Makrofol N) exhibits a diameter of about 150 nm, while in polyethylentherephthalate (Hostaphan) single wires with diameters down to 20 nm can be fabricated [67]. This problem does not occur in the case of multi-pore membranes; probably because the electric field can reach through more easily in the case of a bigger number of pores. A drawback of PET in comparison to PC is the rougher surface of the pore walls.

Chapter III

MORPHOLOGY AND CRYSTALLOGRAPHIC PROPERTIES

The morphology and crystallographic orientation of the nanowires depends on the deposition conditions (electrolyte, temperature and overpotential) as well as on the substrate. In a polycrystalline material crystallographic axes of individual grains are randomly oriented. If one or more crystallographic axes of grains constituting a polycrystal have a preferred orientation, the polycrystalline material exhibits a preferred texture. The development of texture is based on the different growth rates of various crystal faces. During the deposition process, ad-atoms are attached on the surface of an already existing crystal. Depending on their mobility, they may move to vacant positions of the crystal and build it up further or may act as starting nuclei for a new crystal. Higher mobilities of the ad-atoms lead to a more pronounced texture. The higher the number of ad-atoms per time on a given surface area, i.e. higher current densities, the smaller is their mobility due to interaction between them. Hence, increased j leads to nucleation and thus to polycrystalline wires. Higher mobilities of the ad-atoms lead to a more pronounced texture. The mobility of ad-atoms is increased by higher temperature because diffusion on the crystal surface becomes enhanced. This induces the growth of single-crystalline wires. In summary, lower current densities and higher temperatures facilitate the deposition of single-crystalline wires while converse conditions favour the growth of polycrystalline ones [66].

In order to find out the conditions for growth of single-crystalline bismuth nanowires, wires were generated under different deposition conditions and subsequently investigated by

various techniques. In this chapter, the results on the morphology of both caps and nanowires, as well as the crystalline structure of the wires are discussed and linked to each other. The cap morphology was imaged by means of scanning electron microscopy (SEM), while the wire shape was examined by transmission electron microscopy (TEM). The wire crystallinity was studied via x-ray diffraction (XRD) and TEM including selected-area electron-diffraction (SAED) [68].

III.1 Scanning electron microscopy of wire caps

Caps of nanowires grown potentiostatically in pores with diameters 100 - 200 nm under different conditions are depicted in Fig. 15. For depositions performed at room temperature applying –40 mV (Fig. 15(a)), the caps are hemispherical and formed by grains of size well below a micrometer. The crystal size increases for depositions carried out at 60 °C (Fig. 15(b)). If, in addition, a lower overvoltage is applied (U = -20 mV), the grain size becomes larger and distinct facets are formed (Fig. 15(c)). These findings indicate that the crystal size is a function of the fabrication parameters U and T. At elevated temperatures, the surface diffusion rate of ad-atoms increases and the atoms can move more easily to vacant positions, building up larger and more perfect crystals. As discussed in chapter II, increased overpotentials involve higher current densities. For depositions with -20 mV at 60 °C, j is only a few mA/cm², while it is about 20 times higher when applying -40 mV at the same temperature. Due to the lower overpotential and, thus, lower current density, the number of ad-atoms diminishes. Therefore, already existing crystals are further constructed and less nucleations occur.

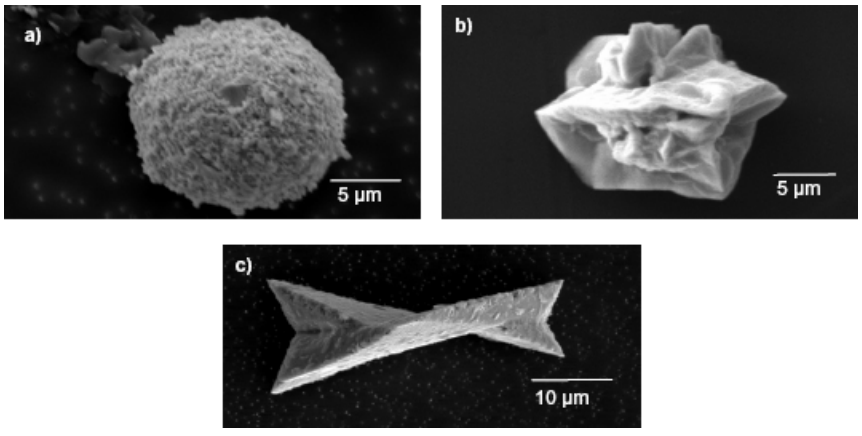

Figure 15: SEM-images of Bi nanowire caps deposited potentiostatically. a) U = -40 mV, T = room temperature, b) U = -40 mV, T = 60 °C and c) U = -20 mV, T = 60 °C

Fig. 16 depicts caps grown potentiostatically (U = -20 mV, T = 60 °C) on top of nanowires of different diameters, namely 360, 240, 160 and 35 nm. Although potential and temperature are the same for all four samples, j decreases from 23 to 3 mA/cm^2 for depositions in nanopores of diameter 360 and 35 nm, respectively. The facets of the caps become more pronounced for narrower pores and smaller j, as the deposition rate diminishes. The smooth contour and the characteristic facets of the cap on top of 35 nm diameter nanowires indicate a preferred orientation of the crystals in the wires or even nanowire single-crystallinity [69].

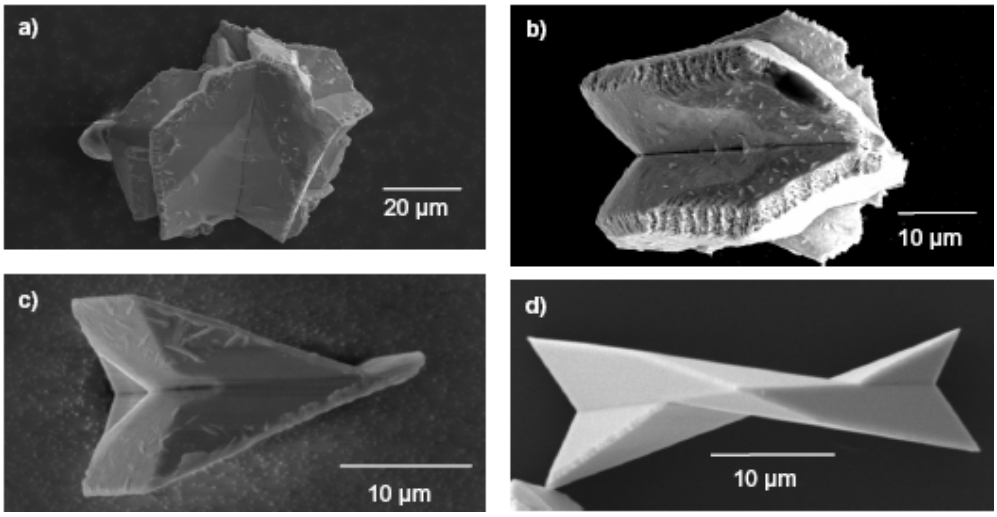

Figure 16: SEM images of caps of Bi wires deposited potentiostatically with U = -20 mV at T = 60 °C. Caps on top of a) 360 nm, b) 240 nm, c) 160 nm and d) 35 nm diameter wires.

In Fig. 17, a cap grown on top of 80 nm diameter wires deposited with reverse pulses at 60 °C is displayed. As potential, square pulses of -20 and +15 mV lasting for 1 and 0.1 s were applied, respectively. The cap possesses a smooth shape with pronounced facets of different orientations indicating another crystal orientation in the needles. The improved single-crystallinity under reverse-pulse deposition is ascribed to the fact that during the anodic pulse defect sites are preferentially dissolved.

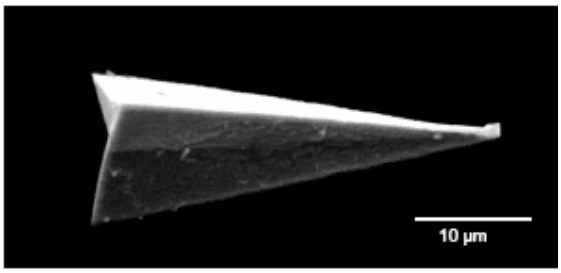

Figure 17: SEM micrograph of a Bi cap deposited at 60 °C applying reverse pulses. Cathodic pulse: -20 mV duration 1 s, anodic pulse: 15 mV duration 0.1 s

III.2 X-ray diffraction of arrays

III.2.a Four-circle diffractometry

The incoming photons are diffracted in the sample; the process must fulfill Bragg's law

$$2d \sin\theta = n\lambda \tag{9}$$

where d is the lattice plane distance, θ the diffraction angle, λ the wavelength of the x-rays, and n an integer. In the case of analysing the sample by a polychromatic beam, diverse wavelengths are diffracted at different angles (Laue diffraction). By using monochromatic x-rays, the angles of the incoming and outgoing beams are scanned. In the present work the rotating-crystal method is used. It requires that the sample is rotated with respect to the incident beam.

X-rays are produced by accelerating electrons to 6.9 keV and focusing them on a Co anode. The tube operates at 35 kV and 30 mA. Since the original radiation is polychromatic, all but one wavelength have to be eliminated. Therefore, the beam is focused on a crystal that serves as a monochromator. The incoming photons are diffracted at the crystal's lattice planes so that at a certain sample angle only one wavelength is recorded, according to Bragg's law (see Fig. 18). With graphite as monochromator, x-rays of $K_{\alpha 1}$ (λ = 1.788965 Å) and $K_{\alpha 2}$ (λ = 1.79285 Å) of cobalt are selected. Their energy difference amounts to about 20 eV which is negligible in comparison to their total energy. The advantage of using two wavelengths is the higher beam intensity. Given by a beam divergence of 0.8°, the diameter of the beam spot on the sample is approximately 2 mm.

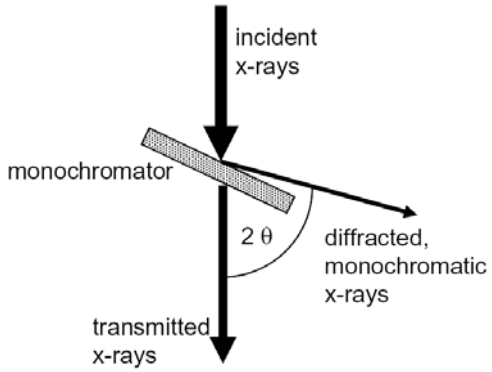

Figure 18: Schematic of an x-ray monochromator.

X-ray diffraction is performed by means of a four-circle diffractometer (Fig. 19) which allows one to rotate the sample around three axes being normal to each other.

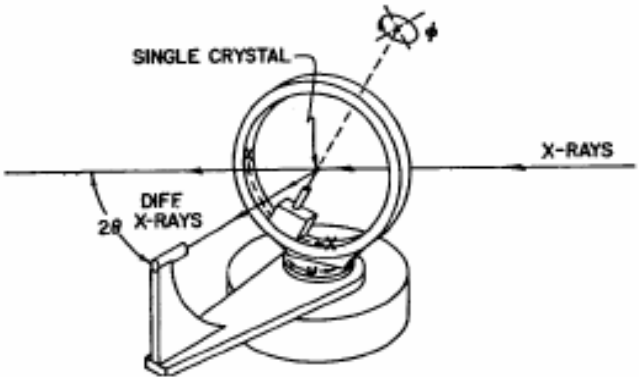

Figure 19: Schematic of a four-circle diffractometer.

The preferred crystalline orientation is determined by recording a so-called ω-2Θ scan, i.e. the sample is rotated by an angle ω while the detector is rotated by twice the angle in order to fulfil the Bragg-rule. This procedure is sketched in Fig. 20.

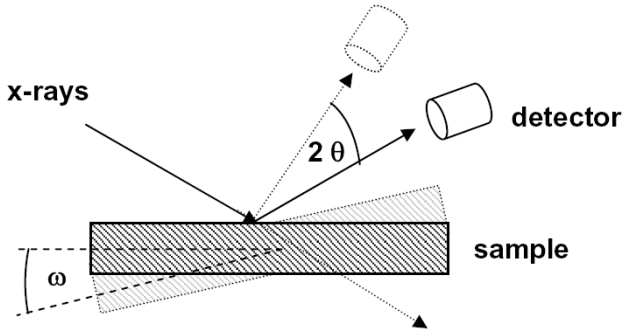

Figure 20: Schematic of recording an ω-2θ-diffractogram.

Information about preferential orientations, i.e., textures, is deduced from ω-2Θ scans by calculating their texture coefficients *TC* using the following equation:

$$TC(h_i k_i l_i) = N \frac{I(h_i k_i l_i)/I_0(h_i k_i l_i)}{\sum I(h_n k_n l_n)/I_0(h_n k_n l_n)} \qquad \textbf{(10)}$$

I_0 represents the tabulated intensities of a standard powder sample, while I stands for the measured intensities. The background has to be subtracted for each signal separately in order to obtain the correct peak height. N is the total number of signals that have been taken into

account. The parenthesized variables *(hkl)* denote the Miller indices of the lattice planes of a given signal. The index *n* runs from 1 to *N*, whereas *i* represents the atomic plane of the calculated texture coefficient.

If $TC(h_ik_il_i) > 1$, the sample exhibits a texture that becomes stronger for increasing $TC(h_ik_il_i)$, and whose maximal value is *N*. All diffractograms shown in this part are compared to the intensities of a standard bismuth powder, taken from the literature [70]. The signals of the standard powder are included at the bottom in each diffractogram. The samples under study are prepared as described in Chapter II. Because of the backing layer consisting of gold and copper, reflections of these elements are observed in the ω-2θ-scans. These signals are excluded from the calculation of the texture coefficients.

In order to analyse a texture in more detail, rocking curves are recorded. For this purpose, the detector is fixed at the reflection angle θ of the atomic plane $(h_ik_il_i)$ that is of particular interest. The sample is scanned while rotating around the chi axis that is orthogonal to both the omega axis and the longitudinal wire axis (Fig. 21). The reflection signal at χ = 90° belongs to crystals oriented thus that the normal of the $(h_ik_il_i)$ lattice plane is parallel to the wire axis. Signals outside the peak at 90° correspond to crystals which are differently oriented. If the sample does not exhibit any texture, it is assumed to be polycrystalline; signals at each tilting angle are recorded, leading to a broad distribution without any global maximum. Thus, the full width at half maximum of the rocking curve is an indication of the crystal orientation.

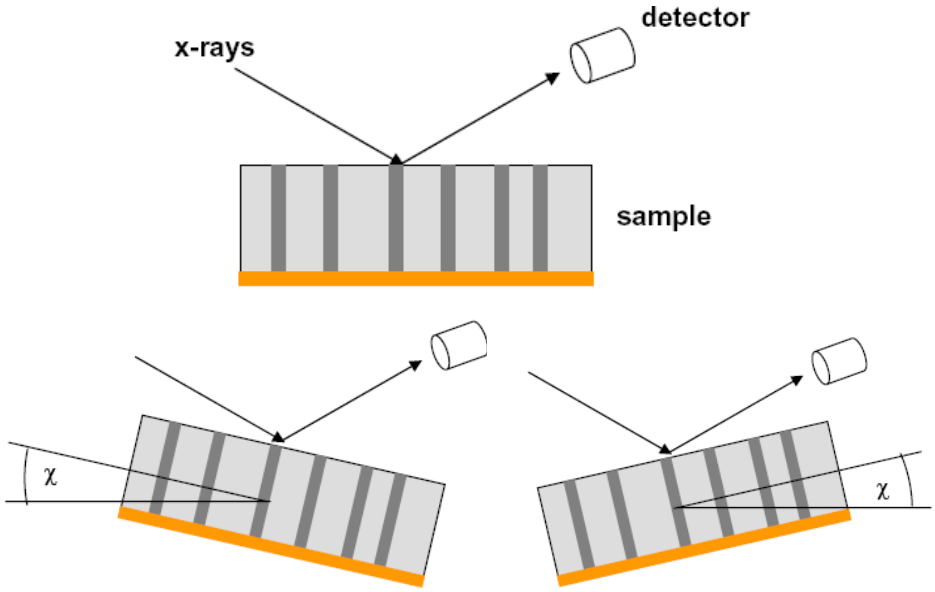

Figure 21: Schematics of recording a rocking curve by rotating the sample around the chi axis. The detector is fixed at the reflection angle θ of the atomic plane $(h_ik_il_i)$ of particular interest.

III.2.b XRD on wires deposited potentiostatically

Figure 22 shows x-ray diffractograms (a) and rocking curves on the (110)-lattice planes (b) of arrays with 80 - 100 nm diameter nanowires, prepared at various overpotentials and temperatures. In comparison to the strongest signal for a standard powder – originating from the (012)-atomic planes - the reflex of the (110)-lattice planes increases by lowering the voltage and elevating the temperature. While the (110)/(012) signal ratio is about 1/3 in poly-crystalline bismuth, it amounts to about 1 for nanowires deposited at 60 °C, applying –30 mV and at 50 °C, and –20 mV. In the case of wires prepared at 60 °C, and –20 mV, this ratio increases to 5.5. The texture coefficient of the (110)-lattice plane, taking $N = 5$ Bi-peaks into account, are 1.3, 1.8, and 4.2, respectively (Table I). The signal-to-noise ratio (Table I) of the signals of the rocking curves presented in Fig. 22(b) rises with increasing *TC(110)* from 1.8 to 3.8 and to 19.4. Because signals outside the peak at 90° belongs to different oriented crystals, a higher signal-to-noise ratio indicates a larger number of grains oriented along the <110> direction. Hence, the growing signal-to-noise ratio confirms the stronger crystal orientation for wires that possess a large texture coefficient. The slight shifts of the peak are ascribed to a misalignment of the samples mounted slightly out of the horizontal plane.

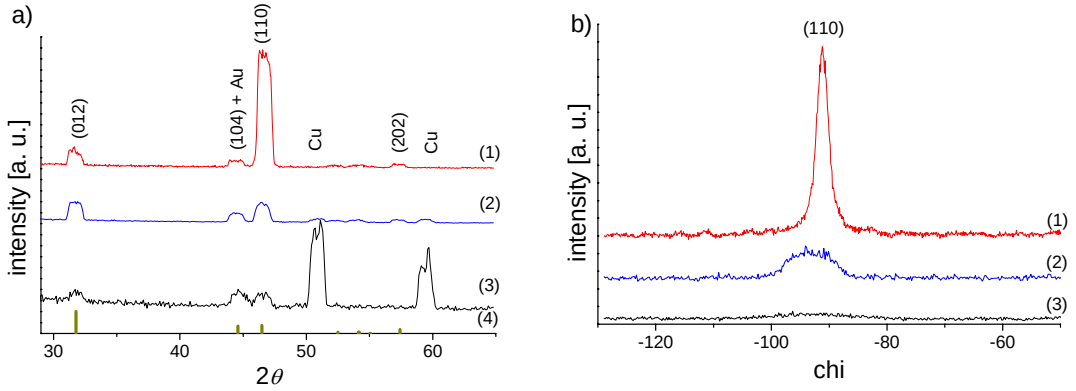

Figure 22: X-ray diffraction measurements on Bi nanowires with diameters 80 – 100 nm deposited potentiostatically at various voltages and temperatures: (1) -20 mV, 60 °C, (2) -20 mV, 50 °C, (3) -30 mV, 60 °C, (4) standard powder. a) ω-2θ scans and b) corresponding rocking curves on (110)-lattice plane.

deposition conditions (d = 80 – 100 nm)	*TC(110)* (N = 5)	rocking curve: (110)/noise
T = 60 °C, U = -30 mV	1.3	1.8
T = 50 °C, U = -20 mV	1.8	3.8
T = 60 °C, U = -20 mV	4.2	19.4

Table I: Evaluation of the x-ray diffraction curves of Fig. 22: Calculated texture coefficient of the (110)-lattice plane and signal-to-noise ratio of corresponding rocking curves.

X-ray diffractograms and rocking curves of nanowire arrays, fabricated under the same conditions (T = 60 °C, U = -20 mV) but possessing different wire diameters, are depicted in Figs. 23(a) and (b), respectively. The (110)/(012) signal ratio increases for diminishing nanowire diameter. While this ratio amounts to about 3 for 160-nm diameter wires, it increases up to 9 for 40-nm diameter needles. In the latter case, the ratio is by a factor of 25 larger than expected for a standard powder sample, implying a strong <110> texture. This indication is confirmed by the texture coefficient (N = 5), which rises from 2.8 for 160 nm diameter wires to 4.5 for the thinnest ones, as well as by the signal-to-noise ratio of the rocking curve, which is the highest (~ 26) for the thinnest wires (Table II).

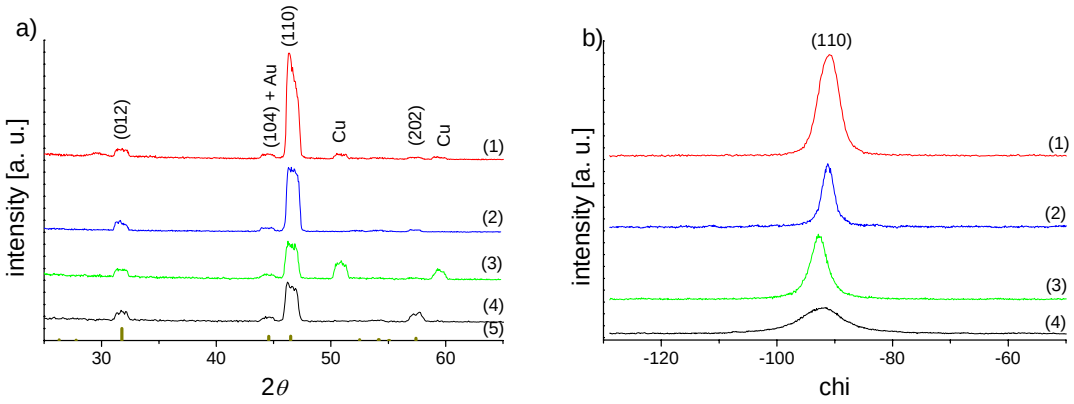

Figure 23: X-ray diffraction curves of bismuth nanowires of various diameter fabricated with fixed deposition parameters 60 °C, and –20 mV: (1) d = 40 nm, (2) d = 80 nm, (3) d = 120 nm, (4) d = 160 nm, (5) standard powder. a) ω-2θ scans and b) corresponding rocking curves on (110)-lattice plane.

wire diameter (T = 60 °C, U = -20 mV)	*TC(110)* (N = 5)	rocking curve: (110)/noise
d = 160 nm	2.8	7.4
d = 120 nm	3.8	24.1
d = 80 nm	4.2	19.4
d = 40 nm	4.5	25.9

Table II: Evaluation of the x-ray diffraction curves of Fig. 23: Calculated texture coefficient of the (110)-lattice plane and signal-to-noise ratio of corresponding rocking curves.

Figure 24(a) shows the x-ray diffractogram of an array of 35-nm diameter Bi nanowires deposited at 60 °C, and smaller overpotential than before, namely, –18 mV. The signal of the (110) lattice plane enormously surpasses all other peaks. The (110)/(012) signal ratio amounts to 64, i.e. about 180 times the value of a standard powder sample. Even the peak of the next order, namely the signal of the (220) lattice planes, that amounts to 3.6 % of the signal of the

(012) atomic planes in polycrystalline bismuth, surpasses the latter one by a factor of about five. This indicates that the wires possess a very pronounced <110> texture. The texture coefficient *TC(110)* amounts to 9.6 (N = 10). The rocking curve in Fig. 24(b) shows a full width at half maximum (FWHM) of only 1.9° and a signal-to-noise ratio of more than hundred, demonstrating a high degree of orientation of the crystals. This sample, prepared with the lowest overpotential, shows the highest (110)/(012) ratio, the largest *TC(110)* and the highest signal-to-noise ratio of the rocking curve. The fraction of crystals oriented with the normal of the (110) lattice plane parallel to the wire axis is derived by evaluating the rocking curve in more detail. All crystals whose (110) lattice planes are normal to the wire axis contribute to the peak at 90°, while all grains oriented in another manner contribute to the noise of the rocking curve. Subtracting the background from the signal results in the fraction of <110>-oriented crystals. Applying this calculation to the rocking curve presented in Fig. 24(b) shows that more than 90 % of the crystals are <110>-oriented.

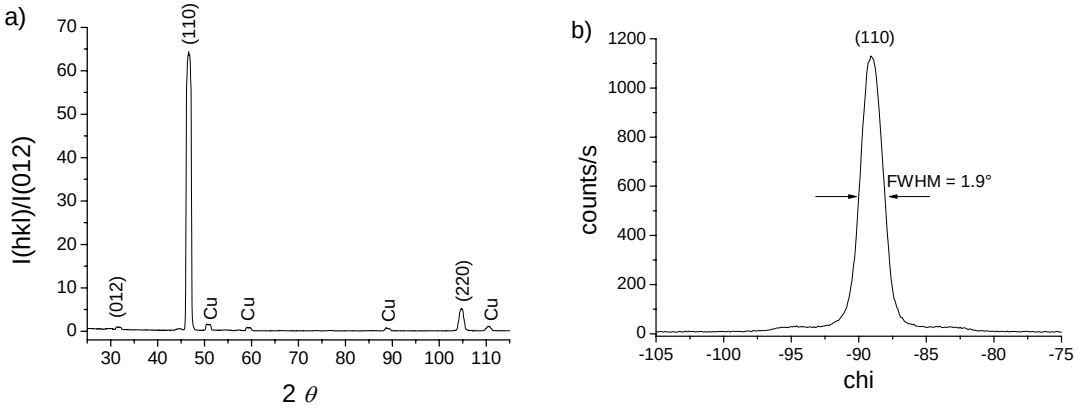

Figure 24: X-ray diffraction curves of Bi nanowires with diameter 35 nm. a) Omega-two-theta scan whose intensity is normalized to the (012) signal and b) rocking curve of the (110)-lattice plane.

III.2.c XRD on wires deposited by reverse pulses

X-ray diffractograms of nanowires with diameter 80 nm deposited with reverse pulses are presented in Figs. 25(a) and (b). In all cases, the cathodic voltage is U_c = -20 mV, and the anodic cycle lasts for t_a = 0.1 s. In part (a), the anodic voltage amounts to U_a = +15 mV, while the cathodic cycle length t_c is varied. The (110)/(012) signal ratio and the corresponding texture coefficient increase for depositions with longer cathodic cycle t_c. Taking N = 11 bismuth signals into account, *TC(110)* amounts to about 1 for depositions with t_c = 0.5 s, whereas it rises to 2.6 for depositions with longer cathodic cycles (t_c = 2 s). For shorter cathodic cycles, the (300)/(012) signal ratio and the *TC(300)* become larger (Table III). The *TC(300)* is about 0.9 for samples deposited with t_c = 2 s, whereas it increases to 4.5 for nanowires fabricated with t_c = 0.5 s.

In part (b), the cathodic cycle length is constant (t_c = 0.5 s), and the anodic voltage U_a is varied. In this case, *TC(110)* amounts to 1 for depositions with U_a = 15 mV or 10 mV, while it increases to 2.5 for depositions with a lower anodic voltage of U_a = 5 mV. For depositions at higher anodic voltage, the (300)/(012) signal ratio and the *TC(300)* become larger (Table III). The *TC(300)* is about 1.1 for samples deposited with U_a = 5 mV and increases to 4.5 for nanowires created with U_a = 15 mV.

The <300> texture corresponds to a <100> texture. The reflection signal of the (100) lattice plane cannot be detected due to destructive interferences. The findings addressed above are supported by the recorded rocking curves (Fig. 25(c)). The peak at 90° belongs to crystals whose (110) lattice plane is normal to the wire axis, while the signals at 60° and 120° belong to grains with the (100) atomic plane orthogonal to the needle axis. These additional signals are observed only when the samples are deposited with short cathodic pulses (t_c = 0.5 s) and high anodic voltage (U_a = 15 mV), whereas they are absent for wires synthesised with longer t_c or rather smaller U_a.

In summary, nanowires created with short reverse pulses and high anodic voltage possess a <100> texture, whereas longer cathodic cycles and smaller anodic voltage favour the creation of <110> textured wires.

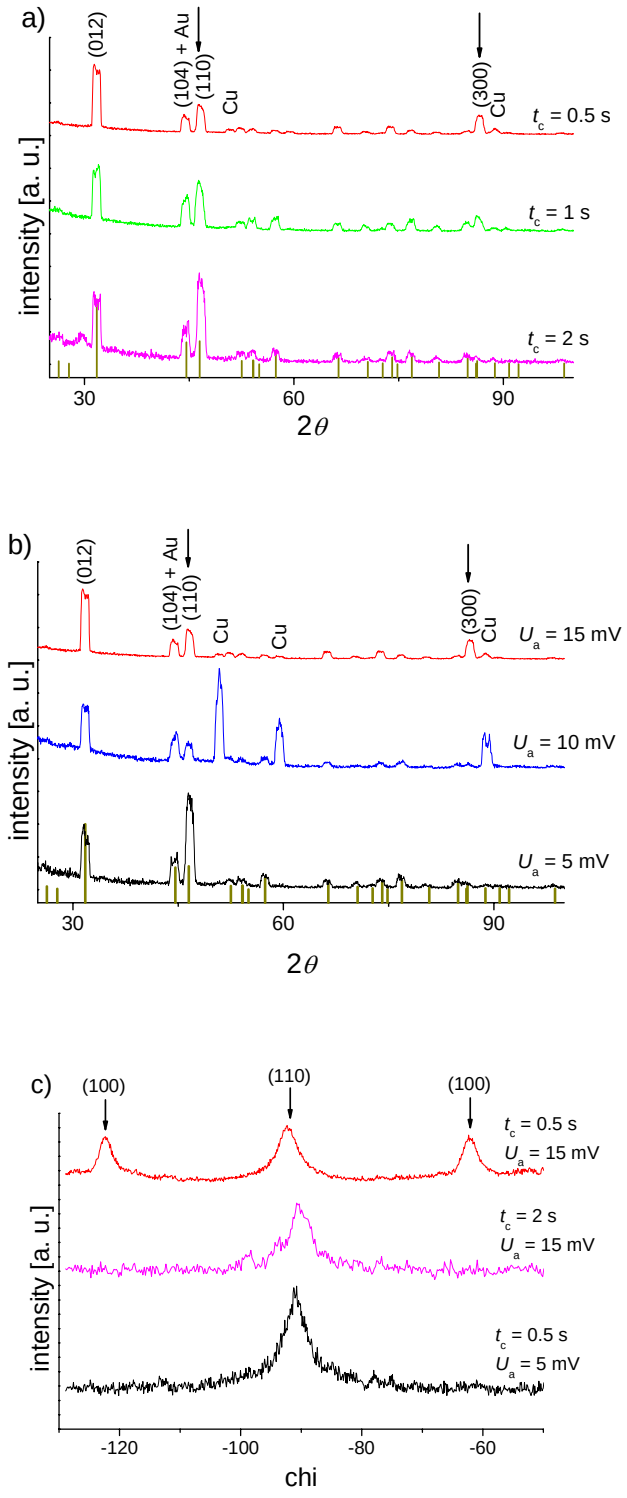

Figure 25: X-ray diffraction curves of 80-nm diameter bismuth nanowires deposited at 60 °C, applying reverse pulses. Omega-two-theta scans of nanowires deposited with a) U_a = 15 mV for t_a = 0.1 s and U_c = -20 mV of various lengths t_c and b) U_c = -20 mV for t_c = 0.5 s and for t_a = 0.1 s diverse anodic voltages U_a. c) Corresponding rocking curves of the (110) lattice plane.

deposition conditions (d = 80 nm, U_c = -20 mV, t_a = 0.1 s)	*TC(110)*	*TC(300)*
t_c = 0.5 s, U_a = 15 mV	1.0	4.5
t_c = 0.5 s, U_a = 10 mV	0.9	2.1
t_c = 1.0 s, U_a = 15 mV	1.3	2.7
t_c = 2.0 s, U_a = 15 mV	2.6	0.9
t_c = 0.5 s, U_a = 5 mV	2.5	1.1

Table III: Evaluation of x-ray diffraction curves in Figs. 25(a) and (b): Calculated texture coefficients of the (110) and (300) lattice plane.

Our investigations on electrochemically deposited wires reveal that the wire crystallinity and texture can be controlled by the deposition parameters. Wires grown potentiostatically are <110> textured in good agreement with results of Wang et al. [13]. The texture becomes more pronounced for higher deposition temperatures, smaller overpotential, and nanopores of smaller diameter. Under reverse pulses, the wire texture can be altered. Such wires grow along the <100> direction where the texture becomes more pronounced for shorter reverse pulses and higher anodic voltages.

Several other groups performed studies on the fabrication and crystallographic characterization of bismuth nanowires in which diverse growth methods have been employed. Wires created by high-pressure injection of molten bismuth into pores of anodic aluminum oxide (AAO) membranes exhibit different textures depending on the wire diameter. While wires of d = 95 nm exhibit a <202> texture, wires of d = 40 nm possess a <012> texture [20]. For pores with diameters of few ten nanometers, this technique is not suitable since the pressure needed for introducing the melt into the pores becomes too high. By the vapour-phase method, single-crystalline wires of diameters down to 7 nm have been fabricated in anodic alumina templates. For these wires, the normal of the (202) lattice planes is parallel to their longitudinal axis [12]. Thus, those wires exhibit the same crystallographic orientation as the wires of diameter 95 nm grown from the liquid phase. Single-crystalline Bi nanowires that are oriented along the [102] direction were prepared by a low-temperature solvothermal process [16]. Furthermore, <110> textured bismuth wires were grown electrochemically in AAO host material [13]. This listing indicates that the preferred orientation of crystals in Bi nanowires is obviously a function of the fabrication technique.

III.3 Transmission electron microscopy

In order to examine nanowires by means of transmission electron microscopy (TEM), the template is dissolved in an organic solvent, either dichloromethane (CH_2Cl_2) or dimethylformamide (C_3H_7NO, DMF). After dissolution, the beaker containing the solvent with the sample is introduced in an ultrasonic bath. Thereafter, few drops of the solvent containing clean nanowires are put on a carbon-covered TEM grid. The microscopic investigations are performed with a Philips CM 20 operating at 200 kV. It has a point and line resolution of 2.3 and 1.4 Å, respectively. Besides direct imaging of the samples, selected-area electron-diffraction (SAED) is performed.

The micrograph in Fig. 26 displays a pair of nanowires deposited potentiostatically (U = -19 mV, T = 60 °C) that show identical extinction contours. The identical extinction patterns of both wires demonstrate that they have been grown with the same crystalline orientation. Such wire pairs grow most probably in pores that are connected to each other, arising from overlapping of the pores during the etching process. In order to distinguish between grain boundaries and extinction contours that originate from bent wires resulting in a deformed lattice structure, the sample was tilted during the microscopy studies. Grain boundaries are characterized by being stationary, while extinction contours move during this process. These examinations did not reveal any grain boundaries within the wire sections.

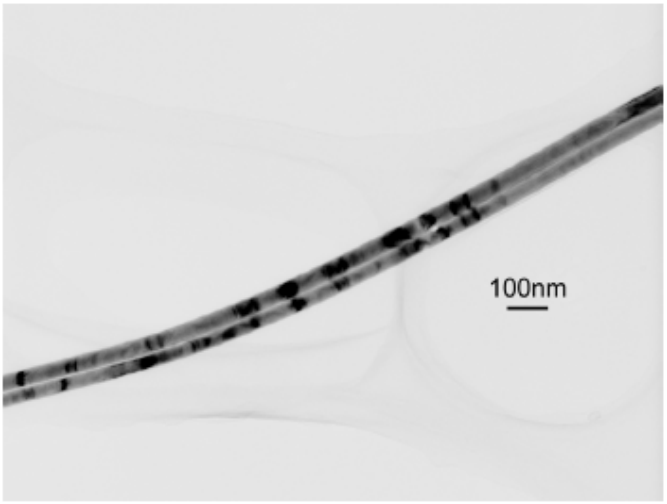

Figure 26: TEM micrograph of a pair of 50-nm diameter Bi nanowires deposited at 60 °C and -19 mV.

Fig. 27 shows a TEM image of a wire ca. 3 µm in length together with the selected-area electron-diffraction patterns from three different wire sections. The direct image displays only extinction contours, while no grain boundaries were found. The single-crystalline character of the nanowires, already indicated by XRD-measurements and SEM-images of the caps, is confirmed by the SAED pattern. The SAED patterns reveal that the wire is a single crystal twisted by less than 5.6°: The left pattern displays the fairly well orientated zone $[1\,\bar{1}\,1]$. In the right pattern, zone $[4\,\bar{4}\,5]$, being distant from $[1\,\bar{1}\,1]$ by a torsion angle of 5.6°, is indicated but not yet reached, i.e., the wire section is distorted by ~ 5°. Most probably, this distortion originates from mechanical stress during the ultrasonic treatment. The (110) reflection points in the direction of the wire. This implies that the c-axis of the rhombohedral cell is perpendicular to the longitudinal extension of the wire. These findings agree with the x-ray diffraction measurements, and with former experiments performed on epitaxial Bi films and nanowires created by pressing liquid Bi in fine Pyrex capillaries, which demonstrated that the trigonal axis is oriented along the smallest dimension [71].

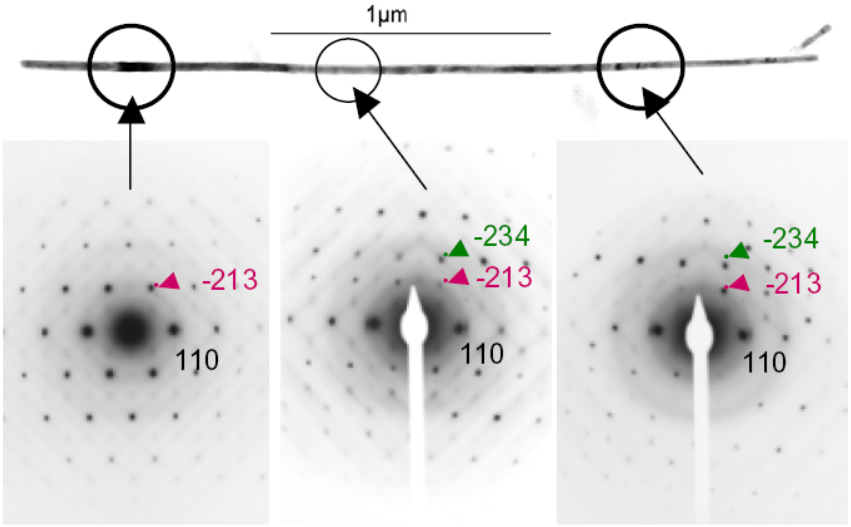

Figure 27: TEM micrograph of 50-nm diameter bismuth nanowires (top) deposited at 60 °C and -17.5 mV, and SAED patterns of three different sections as indicated. The left pattern displays the $[1\,\bar{1}\,1]$ zone, while the right one indicates the $[4\,\bar{4}\,5]$ zone. The central pattern shows an intermediate state of the transition from one to the other crystal zone.

The high-resolution transmission electron microscopy (HRTEM) image (Fig. 28) of a bismuth nanowire of diameter 40 nm deposited at 60 °C and -17 mV reveals the high quality of the single crystal and its well ordered lattice planes.

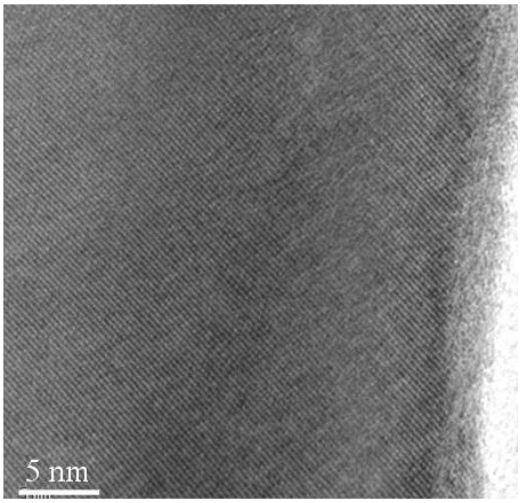

Figure 28: High-resolution TEM micrograph of Bi nanowire grown at 60 °C, applying -17 mV.

The image in Fig. 29(a) display several 80-nm diameter wires deposited with reverse pulses (U_c = -20 mV, t_c = 0.5 s, U_a = 15 mV, t_a = 0.1 s). The micrograph displays mainly extinction contours, while only few grain boundaries (KG) were found. They are about 0.6 µm distant from each other, i.e. they are much closer than in the case of potentiostatically deposited wires. The selected-area electron-diffraction pattern (Fig. 29(b)) exhibits regular Bi reflections and some additional satellite structures ascribed to a modified surface layer (see discussion below).

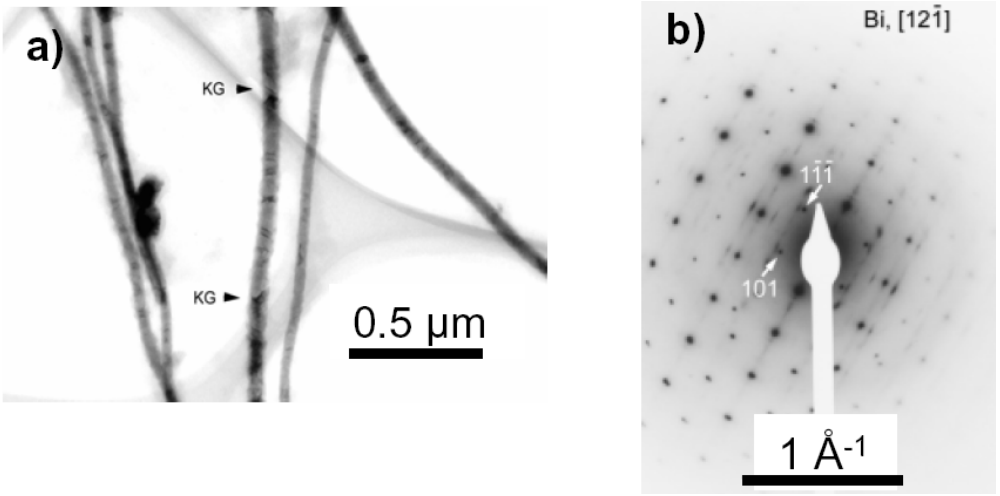

Figure 29: (a) TEM image of 80-nm diameter Bi nanowires deposited with reverse pulses and (b) corresponding SAED pattern.

The HRTEM-images presented in Figure 30 show 40-nm diameter single-crystalline nanowires deposited potentiostatically at 60 °C and –19 mV. The wire sections shown are from the same template but from two different sample areas dissolved either in dichloromethane (CH_2Cl_2) (Fig. 30(a)) or in dimethylformamide (DMF, C_3H_7NO) (Fig. 30(b)). In contrast to DMF, dichloromethane as solvent modifies the surface of the wires being marked by a bracket. The layer consists of a material that possesses a larger interlattice plane distance than bismuth. On top of this layer, an amorphous material is observed that contains most probably polymer residuals.

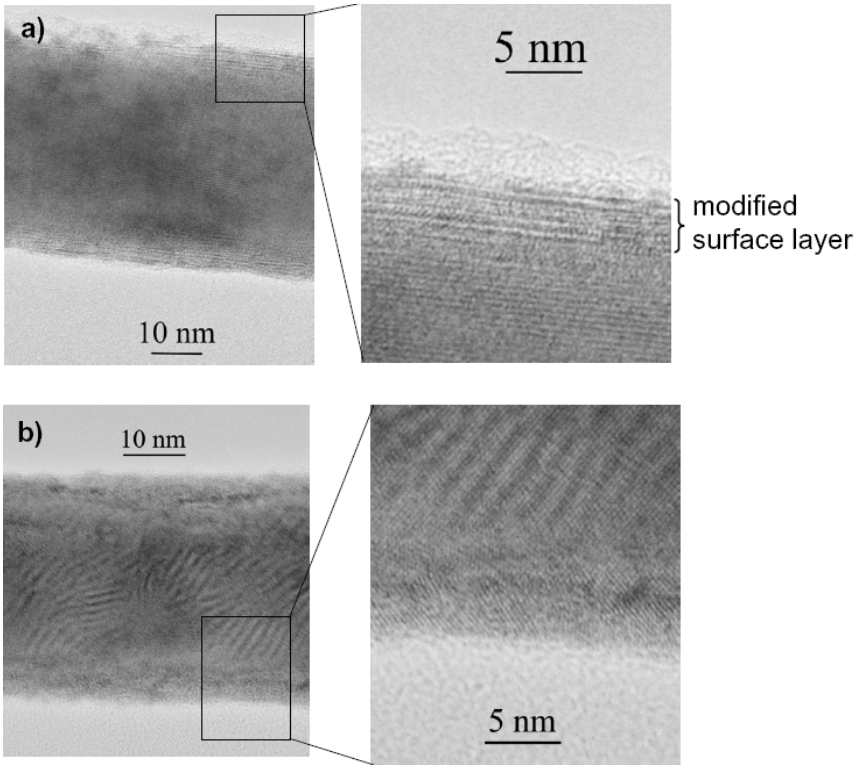

Figure 30: High-magnification TEM-micrographs of bismuth nanowires. The polymere template was dissolved in a) dichloromethane and b) dimethylformamide (DMF). The bracket in part (a) indicates a modified surface layer.

As revealed by energy-dispersive x-ray analysis (EDX) and by calculating the Fourier transform of a micrograph as shown in Figure 31, the modified surface layer consists of bismuth oxychloride (BiOCl) piling up along the c-axis, i.e., normal to the wire axis. Since the surface is not modified for samples dissolved by DMF, it is assumed that the BiOCl layer develops during or after the dissolution of the template in dichloromethane (CH_2Cl_2).

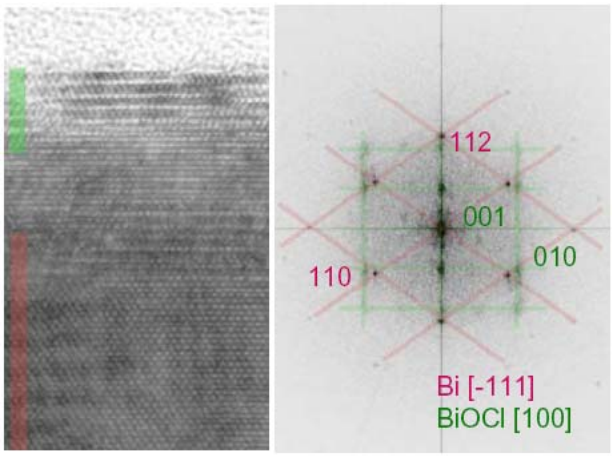

Figure 31: High-resolution TEM micrograph of 50-nm diameter Bi nanowire and Fourier transform of this image.

Results obtained by imaging bismuth nanowires by means of transmission electron microscopy and recording selected-area electron-diffraction patterns coincide with the findings of XRD investigations that the wires grow preferentially along the <110> direction. Grain sizes range from several hundred nanometers up to few micrometers. Few wires are slightly distorted, most probably due to mechanical stress during ultrasonification of the sample. High-resolution TEM micrographs reveal that a surface layer containing BiOCl is formed when dissolving the template by dichloromethane, whereas the formation of such a layer is avoided by employing dimethylformamide.

Chapter IV

INFRARED SPECTROSCOPY

IV.1 Band structure of bulk bismuth

Bulk bismuth is a semimetal with a very small indirect band overlap (E_0 = 98 meV at 300 K [72]) and two direct band gaps at the L- and at the T-point of the Brillouin zone, where electrons and holes are located, respectively. The reduced Brillouin zone [73] and a schematic of the band structure of bismuth are depicted in Figs. 32(a) and (b), respectively. The gap energy at the L-point is rather well known (E_{gL} = 36 meV at room temperature [72]), whereas for the gap energy at the T-point E_{gT} values ranging from few ten to up to several hundred meV can be found in the literature [74, 75, 76]. The Fermi energy amounts to 56 meV, its value being defined with respect to the lower edge of the L-point conduction band [42].

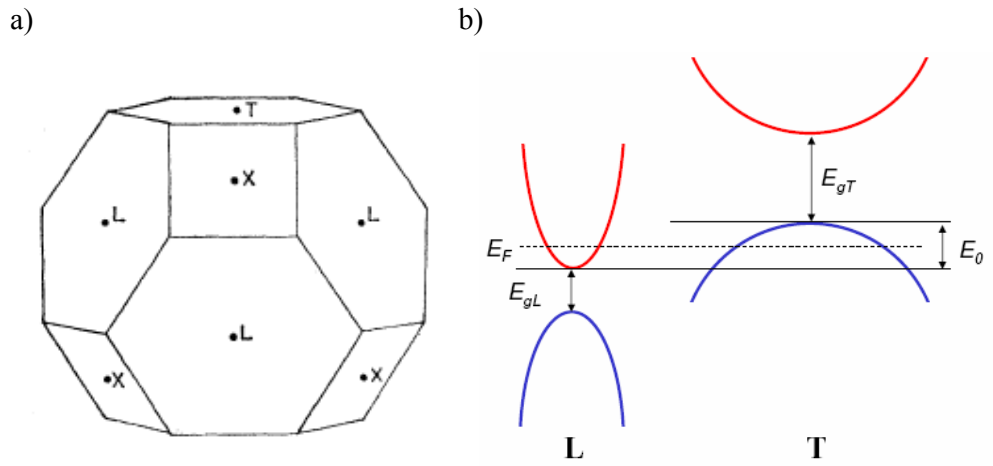

Figure 32: Schematics of a) the reduced Brillouin zone (taken from [73]) and b) the band structure of bismuth. E_F is the Fermi energy, E_0 is the band overlap, and E_{gL} and E_{gT} are the dircet band gaps at the L- and at the T-point, respectively.

Since band gap energies and band overlap are in the infrared range, direct and indirect transitions can be detected by infrared (IR) spectroscopy. The expected energies for the various electronic excitations are presented in Fig. 33. For calculations, E_{gT} is assumed to be about 200 meV {1610 cm^{-1}}. Since all states below the Fermi level are occupied and the wave-vector $\vec{k}$ has to remain constant in the case of direct transitions, the threshold of the excitation energy for direct transitions is composed of the corresponding energy gap and twice E_F. Hence, the energy thresholds for direct transitions at the L- and at the T-point amount to E_{LL} ~ 148 meV {1200 cm^{-1}} and E_{TT} ~ 300 meV {2420 cm^{-1}}, respectively. In the case of indirect transitions, $\vec{k}$ does not have to stay constant due to additional coupling to a phonon which changes the momentum of the excited charge carrier. According to the band structure of bismuth, three different indirect transitions are possible, namely from the valence band at the L-point to both valence and conduction band at the T-point, having the energies $E_{LV\text{-}TV}$ ~ 134 meV {1080 cm^{-1}} and $E_{LV\text{-}TC}$ ~ 332 meV {2680 cm^{-1}}, respectively. Additionally, electrons can be excited from the L-point conduction band to the T-point conduction band, and the threshold energy $E_{LC\text{-}TC}$ being ~ 198 meV {1600 cm^{-1}}. Because of the additional electron-phonon-coupling, indirect transitions are less probable than direct transitions. However, in Bi the Debye temperature T_D is rather low (about 120 K [77]), and room temperature offers sufficient energy in order to excite the necessary phonons. Note that all energies mentioned above are approximations. At finite temperatures, the Fermi level is broadened and electrons may be thermally excited to states above E_F. Hence, states below the Fermi level are vacant involving lower transition energies. Further, it has been assumed that the carrier masses are the same in the lower and the upper band which, especially in the case of the L-point, may be not valid because of the highly anisotropic band structure.

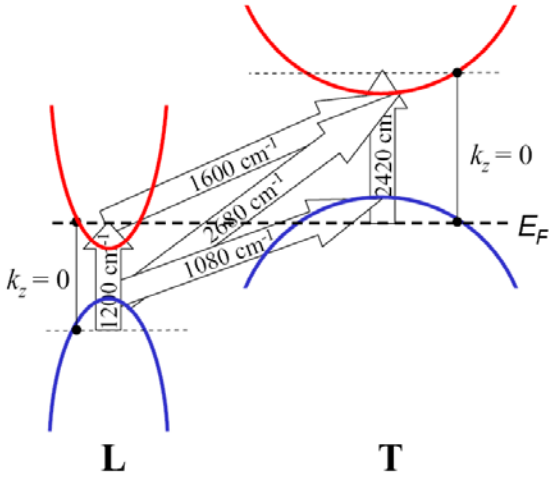

Figure 33: Schematic of the energy thresholds of transitions in bulk bismuth.

Since in conventional metals E_F is large compared to $k_B T$ at room temperature (~ 25 meV), temperature changes do not affect the energy of the Fermi level, whereas in Bi the Fermi energy amounts to less than 3 $k_B T$. E_F is therefore influenced by temperature variations being described by equation (11) where E_{F_0} is the Fermi energy at T = 0 K [78]. According to theoretical predictions, E_F increases from 26 to 56 meV when heating Bi up from 0 to 300 K. Thus, all band parameters are a function of T. The band overlap is expected to decrease from 98 to 38 meV and E_{gL} from 36 to 15 meV when the temperature is reduced from 300 to 0 K.

$$E_F = E_{F_0}\left[1 + \frac{\pi^2 k^2 T^2}{12 E_{F_0}^2}\right] \qquad \textbf{(11)}$$

IV.2 Band parameters of nanowires

IV.2.a Band structure as a function of wire diameter

Energy bands split up into subbands if the size of a specimen is in the range of the Fermi wavelength λ_F. Consequently, the edges of the energy bands shift against each other. In the simplest case, a nanowire can be modelled as a two-dimensional infinitely deep potential well. The energy of a particle possessing an effective mass m^* is given by the equation

$$E = \frac{\hbar^2}{2m^*}\left(k_x^2 + k_y^2\right) \qquad \textbf{(12)}$$

with

$$k_{x,y} = \frac{2\pi}{\lambda_{x,y}} \qquad \textbf{(13)}$$

Since electrons cannot escape from the well, the boundary condition requires nodes of the electron wave function at the wire surface involving the wire diameter d by $d = N \cdot \lambda/2$, where N is the number of the subband. These preconditions lead to an energy separation of the subbands given by equation (14).

$$\Delta E = \frac{N^2 \hbar^2 \pi^2}{m^* d^2} \tag{14}$$

According to the derivation above, the subbands are separated by an energy that is inversely proportional to both the square of the wire diameter d and the effective mass of the charge carriers m^*. The band edge, i.e. the ground state (N = 1) in the potential well, experiences an energy shift of

$$\Delta E = \frac{\hbar^2 \pi^2}{m^* d^2} \tag{15}$$

Because λ_F is large in bismuth (~ 40 nm), the splitting of the bands may be observed in nanowires of larger diameters than in conventional metals. Since the electron effective mass in Bi is very small (0.001 – 0.26 m_e), the energy separation of the subbands and the shift of the band edges are large.

At the L-point, the bands are highly nonparabolic due to the strong coupling between the L-electrons and L-holes. The dispersion relation for the L-point bands is described by the Lax two-band model, where $\vec{\alpha}$ denotes the effective mass tensor [79].

$$\frac{\hbar^2}{2} \vec{k} \vec{\alpha} \vec{k} = E(\vec{k}) \left(1 + \frac{E(\vec{k})}{E_{gL}} \right) \tag{16}$$

For interband transitions, transitions between the n-th valence subband to the n-th conduction subband are allowed, where $|\langle v|p|c\rangle|$ is the coupling between the valence subband v and conduction subband c, and m_e is the free electron mass. At the band edge (k = 0), the momentum matrix element for the different subband states is the same, i.e., as the band gap increases, $|\langle v|p|c\rangle|$ remains constant, and the effective mass increases [29].

$$\frac{1}{m^*} = \frac{1}{m_e} + \frac{2}{m_e^2}\frac{\left|\langle v|p|c\rangle\right|^2}{E_g} - \frac{12\hbar^2 k^2 \left|\langle v|p|c\rangle\right|^4}{E_g^3 m^2} \qquad \textbf{(17)}$$

Figure 34 displays the computed band-edge energies as a function of the nanowire diameter with respect to the energy of the band edge of the L-point conduction band in bulk Bi. For calculations, the values E_{gL} = 36 meV, E_0 = 98 meV, E_F = 56 meV, and E_{gT} = 200 meV are used. In Fig. 34(a), the electron effective mass is assumed to be constant, namely $m^* = 0.002\ m_e$, whereas in part (b) the Lax two-band model has been taken into account. The strong coupling of electrons and holes at the L-point leads to a smaller energy shift of the band edges at the L-point for a given wire diameter. In addition to the shift of the band edges, the Fermi energy increases with diminishing wire diameter. The rise of E_F occurs in order to obtain charge neutrality, i.e., for achieving the same number of electrons and holes. At a critical wire diameter d_c the lowest subband of the conduction and the highest subband of the valence band do not overlap anymore. Thus, bismuth nanowires undergo a transition from a semimetal to a semiconductor at d_c of about 35 nm and 70 nm for calculations with and without incorporating the dependence of m^* on the band gap, respectively. These values are in the same order of magnitude as the results obtained from computations by Lin et al. [26]. Note that d_c is a function of the crystalline orientation due to the highly anistropic Fermi surfaces, resulting in a dependence of the electron effective mass on the crystalline direction.

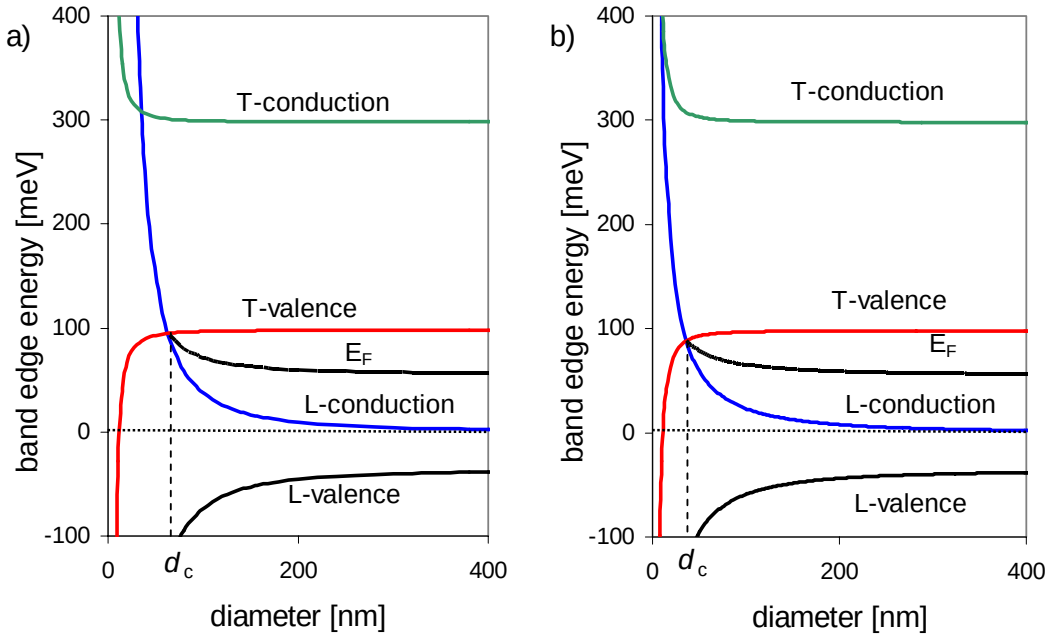

Figure 34: Energy of the band edges as a function of the wire diameter: a) $m^* = 0.002\ m_e$ = const, b) employing the Lax two-band model with $m^* = 0.002\ m_e$.

Due to the shift of the energy bands, the transition energies are also a function of the wire diameter (Fig. 35). The Lax two-band model has been considered using the same values as before. The excitation energy for direct transitions in the vicinity of the L-point and for indirect transitions from the L-point valence band to the T-point valence band increases with decreasing *d*. In contrast, the excitation threshold for direct transitions in the vicinity of the T-point as well as indirect transitions from the L-point conduction band to the T-point conduction band are reduced in energy caused by the balancing character of the Fermi level.

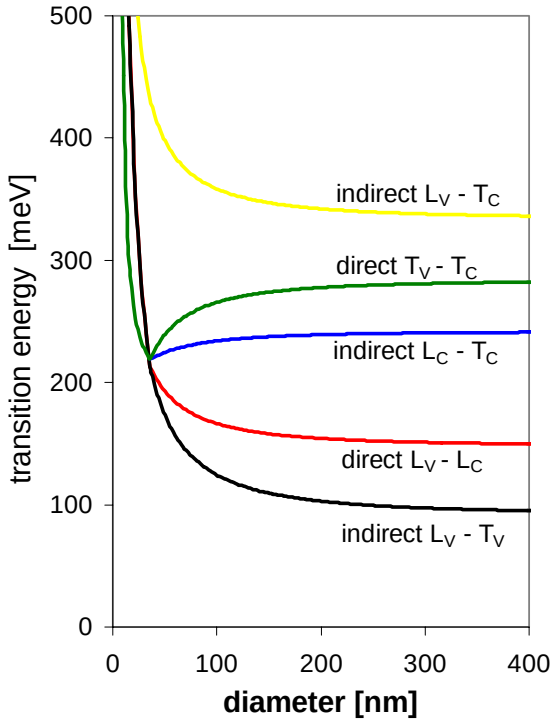

Figure 35: Transition energies as a function of wire diameter using the Lax two-band model with $m_e^* = 0.002\ m_e$.

IV.2.b Plasma frequency as a function of wire diameter

The reducing band overlap for decreasing wire diameter leads to a lower charge carrier density n in the conduction band. Since the plasma frequency ω_P is a function of the carrier concentration, it is expected that ω_P decreases with diminishing d. It is predicted to reduce from 41 meV {333 cm^{-1}} for bulk to about 26 meV {210 cm^{-1}} for wires of diameter 40 nm [30].

$$\omega_P = \sqrt{\frac{e^2 n}{m^* \varepsilon_0}} \qquad \textbf{(18)}$$

In equation (18), ε_0 is the vacuum permittivity.

In contrast to the argumentation above, the charge carrier density and hence the plasma frequency may rise with decreasing wire diameter due to the increase of the surface-to-volume ratio. At the surface, defects may act as dopants as, e.g., observed in Bi thin films where the carrier concentration increases with decreasing film thickness D [46]. The total charge carrier density is given by

$$n = n_i + \frac{n_S}{D} \qquad \textbf{(19)}$$

where n_i is the intrinsic charge carrier density of the pure material, and n_S is the density of additional surface charge states that, according to ref. [46], amounted to $2.75*10^{12}$ cm^{-2}. Surface defects acting as additional carriers may, on the one hand, inhibit the semimetal-to-semiconductor transition of Bi nanowires and, on the other hand, increase the plasma frequency.

IV.3 Experimental setup at ANKA

Infrared-spectroscopic microscopy on single nanowires was performed at the synchrotron light source ANKA (Forschungszentrum Karlsruhe). The synchrotron provides IR beams of both higher intensity and brilliance than conventional laboratory IR sources. The synchrotron beamline exploits the so-called edge radiation as the source rather than classical synchrotron radiation. The edge radiation is emitted by electrons when entering the magnetic field of the bending magnet. Each measurement thus requires less time and is characterized by an improved signal-to-noise ratio. Figure 36 displays a photograph of the experimental setup at ANKA, a sketch of the IR microscope, and a more detailed draft of the IRscope II of the Bruker company [80].

Wire samples are prepared by dissolving the template in dimethylformamide and, then, depositing the wires on a Si substrate which exhibits IR transmission of about 50 % at wavenumbers > 1000 cm^{-1}. The sample is placed under the objective of an optical microscope installed at the IR beam line. Single nanowires are visualized by means of the optical microscope. By introducing an aperture of diameter 8.3 μm in the focal plane of the microscope, single wires are selected. IR tranmission spectroscopy of single wires is performed in the frequency range between 700 and 7000 cm^{-1} with a Fourier transform infrared (FTIR) spectrometer (Bruker IFS 66v/S) into which the IR beam of the synchrotron light source is coupled, and with a mercury cadmium telluride (MCT) detector cooled by liquid nitrogen. In addition, a polarizer can be put into the IR beam either in front of or behind the sample acting as polarizer or analyzer, respectively.

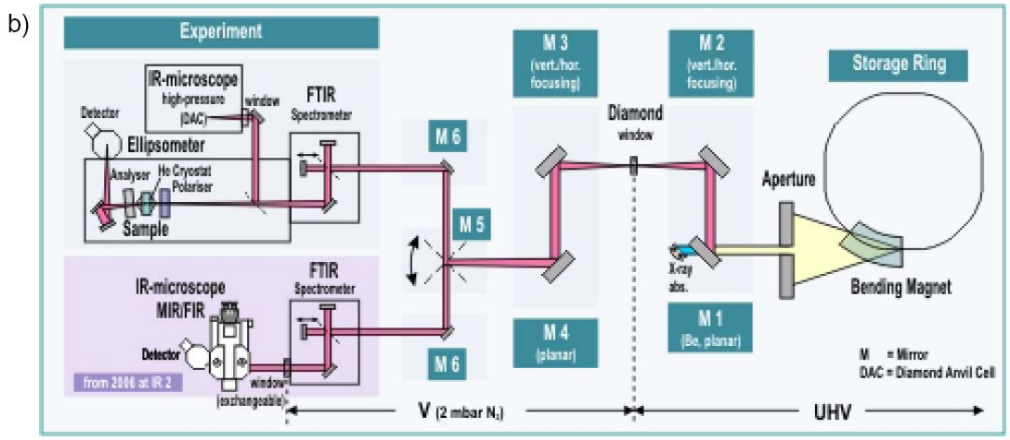

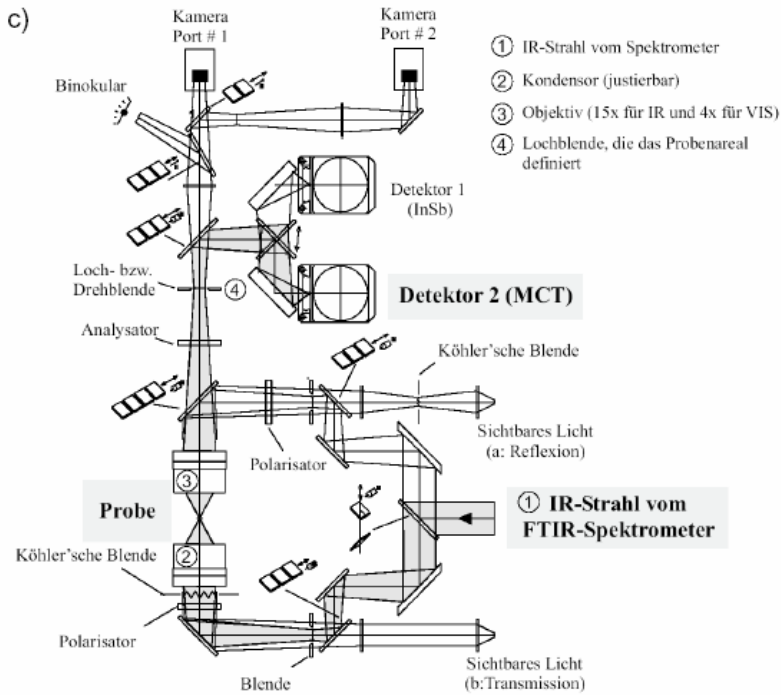

Figure 36: Experimental setup at ANKA: a) photograph, b) schematic (taken from [80], c) more detailed sketch of the IR scope II of the Bruker company taken from ref. [80].

In all cases, IR spectra are recorded at two positions: (1) on the wire, and (2) on a reference position of the bare substrate in close vicinity to the wire (see Fig. 37). To obtain the relative IR transmission $T_{rel}(\omega)$ of a single wire, the substrate intensity $I_{ref}(\omega)$ is substracted from the wire signal $I_{wire}(\omega)$ by

$$T_{rel}(\omega) = \frac{I_{wire}}{I_{ref}} \tag{20}$$

and the absorption spectra $A(\omega)$ are calculated by means of equation (21).

$$A(\omega) = 1 - T_{rel}(\omega) \tag{21}$$

The micrograph in Fig. 37 displays Bi nanowires of diameter 160 nm lying on a Si wafer. The two circles indicate the areas (1) and (2) under investigation. Although the wire diameter is well below the resolution limit of visible light, wires with d > 60 nm can be resolved easily by the optical microscope using an objective of magnification 36 because of the wire length of several micrometers. Smaller nanowires can hardly be located, making it problematic but not impossible to do IR spectroscopy on single wires with diameters of few ten nanometers.

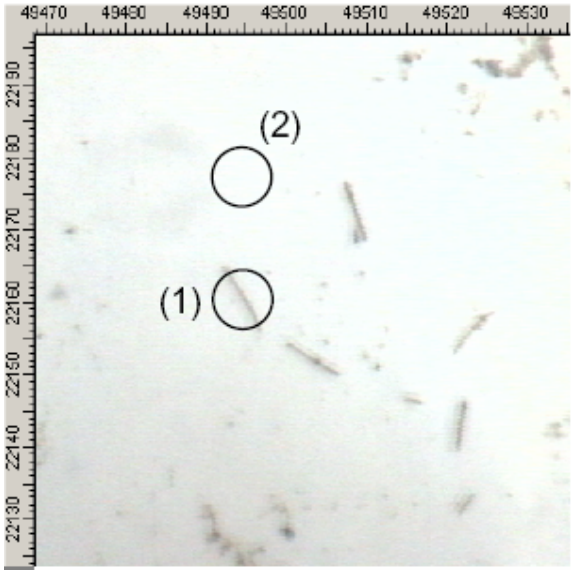

Figure 37: Optical microscopy image (65 x 70 µm^2) of bismuth nanowires with diameter 160 nm on a Si wafer. The two circles correspond to the locations where IR spectroscopy has been performed: (1) single wire and (2) reference position.

IV.4 Infrared spectroscopy on Bi nanowires

Fig. 38 presents IR-absorption spectra of wires with diameter 80 nm, measured on a single wire, on few nanowires lying on each other, and on a bunch of about ten wires. The spectra differ in intensities but, independent of the number of wires, they all exhibit the same absorption properties: (i) They show a strong absorption edge at ~ (1700 ± 100) cm^{-1} and an absorption maximum at ~ (4600 ± 100) cm^{-1}. The maximum intensity seems to be directly proportional to the number of wires. The wavenumber of the absorption onset is determined by extrapolating the strongest increase. The intersection of this tangent and zero absorption is taken as the onset energy. (ii) Additionally, a weaker absorption is observed to the left of the pronounced feature starting at ~ 1000 cm^{-1}.

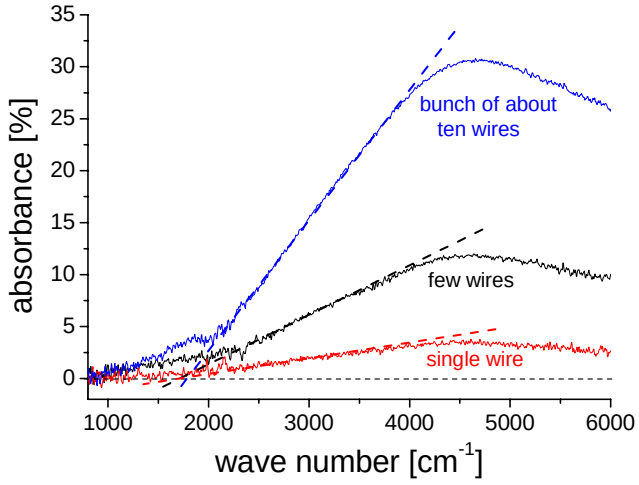

Figure 38: Infrared absorption spectra of bismuth nanowires with diameter of 80 nm on a Si substrate for a single wire, several wires, and about ten wires.

Figure 39 displays two absorption spectra which are normalized to the respective maximal absorption of a single wire with diameter 300 nm, recorded with light that is polarized parallel to the wire axis. The polarizer is placed in one case in front and in the other case behind the sample, serving thus as polarizer and analyzer, respectively. Both spectra exhibit an absorption onset at about 1000 cm^{-1}, indicating that the wires do not influence the direction of the electric field. The slight differences of the absorption spectra are attributed to instabilities of the electron beam in the ANKA ring, and hence to variations of the infrared beam.

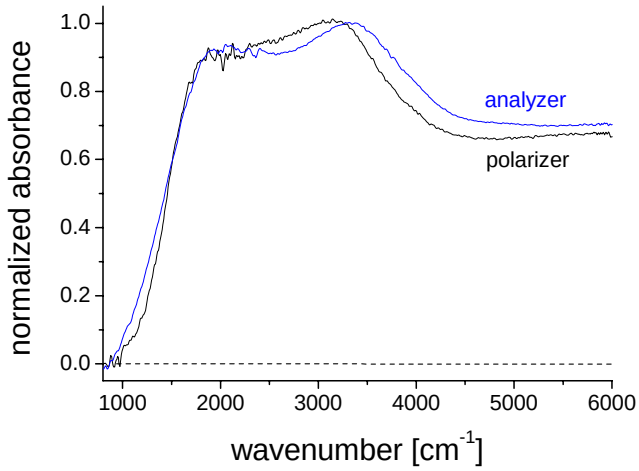

Figure 39: IR absorption of a single bismuth nanowire for light that is polarized parallel to the wire axis. The polarizer is placed in one case in front and in the other behind the sample, serving as polarizer and analyzer, respectively.

IV.4.a IR spectroscopy as a function of wire diameter

IR absorption spectra of single nanowires with diameters 400, 160, 120, 60, and 30 nm are displayed in Fig. 40(a) [81]. For the sake of clarity, several further spectra of wires with other diameters have been omitted in this diagram. To facilitate the comparison, the spectra are normalized to their maximal absorption. All wires were fabricated at 60 °C and applying -17 mV. Each spectrum shows an increase of absorption, passes through a maximum, and declines again. The wires with the largest diameters have the smallest decline. Only for the wire with d = 400 nm a second maximum is observed at higher wavenumbers, which for wires of smaller diameter may be out of the spectral range covered in this experiment. Likewise as in the figure 38, the strongest increase in absorption is extrapolated to zero absorption, and the intersection point is taken as absorption onset $w_A(d)$. The uncertainty in determining the frequency of the absorption edge is presumed to be ± 100 cm^{-1}. With decreasing wire diameter, the absorption onset shifts to higher wavenumbers. For wires with d > 150 nm, w_A is almost constant, while it experiences a strong blueshift for d < 150 nm (Fig. 40(b)). For instance, with respect to wires with d = 400 nm the absorption edge is blueshifted only by about 200 cm^{-1} for d = 160 nm, while the shift amounts to about 2200 cm^{-1} for d = 30 nm.

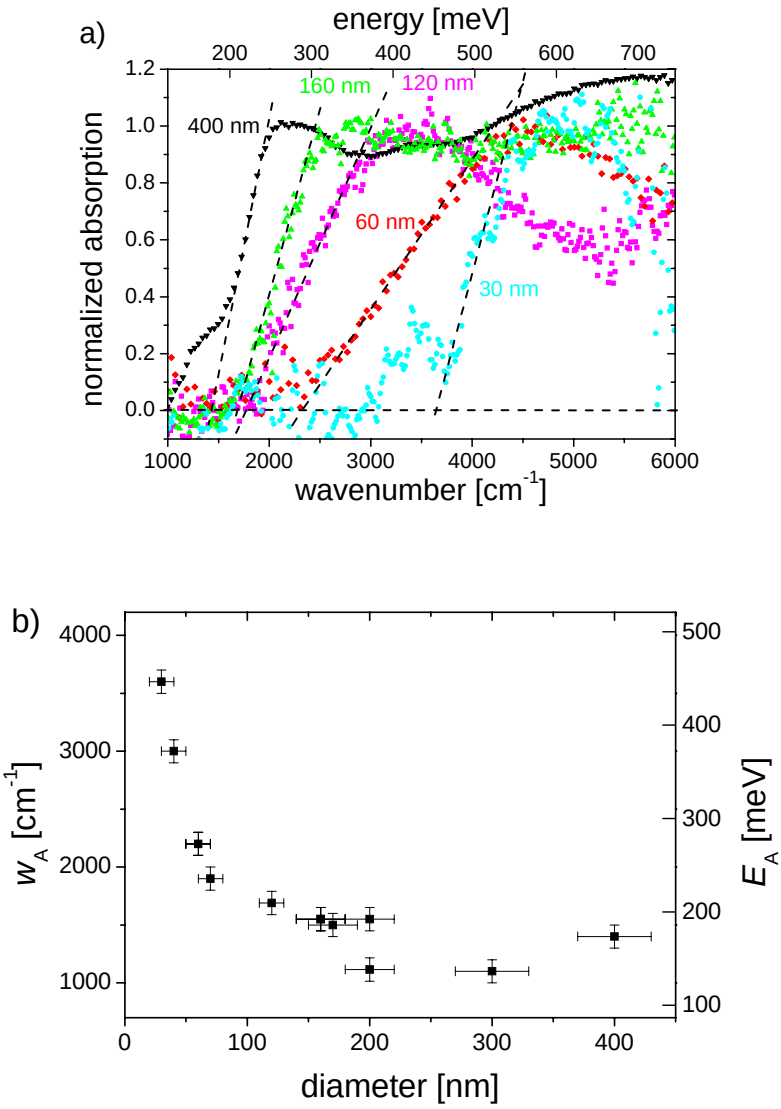

Figure 40: a) Normalized absorption spectra of single bismuth nanowires with diameters 400, 160, 120, 60, and 30 nm. For the sake of clarity, several further spectra of wires with other diameters have been omitted in this diagram. The dashed lines indicate the strongest increase of absorption for each spectrum. b) Wavenumber of the absorption edge as a function of wire diameter.

In the literature, several infrared spectroscopy studies on Bi thin films [82, 85] report on a blueshift of the IR absorption. Different authors ascribe the absorption either to the plasma frequency or the excitation of direct transitions. In the former case, the blueshift may be attributed either to strain in the specimen or to an increased carrier density, and in the latter case to quantum-size effects. Below, the different theoretical approaches are discussed in detail with respect to the data presented in this work.

Takaoka and Murase observed a blueshift of the IR absorption, measured on Bi thin films that were grown on BaF_2 substrates [82]. They observed that the blueshift increases with decreasing film thickness. The authors attributed the absorption to the plasma frequency and its blueshift to a lattice mismatch between Bi film and BaF_2 substrate. Stress effects are excluded for our wires because strain was evidenced neither by x-ray nor by electron diffraction. A blueshift of the plasma frequency could also be caused by an increase of the carrier density n. In order to obtain $w_p = \omega_P/(2\pi c) > 1000$ cm^{-1} with c being the velocity of light, the wires would have to be heavily n-doped to more than $3*10^{19}$ cm^{-3}. Further, this argument seems unrealistic because the concentration of dopants would have to increase with diminishing wire diameter. Possibly surface defects play an important role because they may increase n causing a blueshift of the plasma frequency where $\omega_P^2 \sim 1/D$ [46]. Assuming that the detected absorption is related to the plasma frequency, w_A^2 as a function of the inverse wire diameter is displayed in Fig. 41(a). The solid line represents the best linear fit, while the dashed lines serve as error estimate. The axis intercepts of the solid and dashed lines range between 10^4 and $4*10^5$ cm^{-2}, corresponding to a plasma frequency in bulk bismuth between 200 and 630 cm^{-1}. In the literature a value of about 330 cm^{-1} is found [30]. From the data of Fig. 41(a) and by means of equations (18) and (19), a surface defect density is deduced ranging from $2*10^{14}$ to $2*10^{15}$ cm^{-2}, which is more than two orders of magnitude higher than obtained by Komnik et al. for Bi thin films [46]. Bismuth contains $2.8*10^{22}$ atoms per cm^3 and thus, using a cube as the first approximation, it possesses $9*10^{14}$ surface atoms per cm^2. Hence, about every Bi atom has to be a defect. Such defects may be created during the dissolution of the template or by polymer residuals covering the wires. Additionally, it has been found by means of photoemission studies on bulk Bi that the surface zone is much more metal-like than bulk Bi, i.e., a higher carrier density is found at the surface [83, 84].

Lutskii and Kulik reported on IR absorption edges measured on Bi thin films that shifted to higher energies scaling with $1/D^2$ [85]. In contrast to the argumentation by means of the plasma frequency and surface defects, the authors ascribed the blueshift to an increasing band gap originating from subband splitting caused by quantum-size effects. In order to compare the data with this theoretical approach, the wavenumber of the absorption onset is plotted as a function of $1/d^2$. In Fig. 41(b), a constant electron effective mass is taken into account while Fig. 41(c) considers the Lax two-band model. From the slopes of the solid and dashed lines in part (b) and by means of equation (15), an electron effective mass of $m^* = (0.0056 \pm 0.001)\ m_e$ is deduced. For wires with large diameters, the absorption onset as a function of d^{-2} deviates from a linear behaviour. For bulk Bi, i.e., $1/d^2 = 0$, the axis intercept

ranges between 1100 and 1500 cm^{-1}. As can be seen from part (c), the deviation from a linear dependence for wires with large diameters may be ascribed to an electron effective mass that is a function of the band gap (Lax two-band model). For fitting an effective mass of 0.001 m_e was taken into account. At the L-point, the electrons possess sufficiently small effective masses. In addition, the threshold energy for direct transitions in the vicinity of the L-point in bulk Bi amounts to ~ 1200 cm^{-1} (~ 150 meV). Therefore, excitations in the vicinity of the L-point may explain the observed effect.

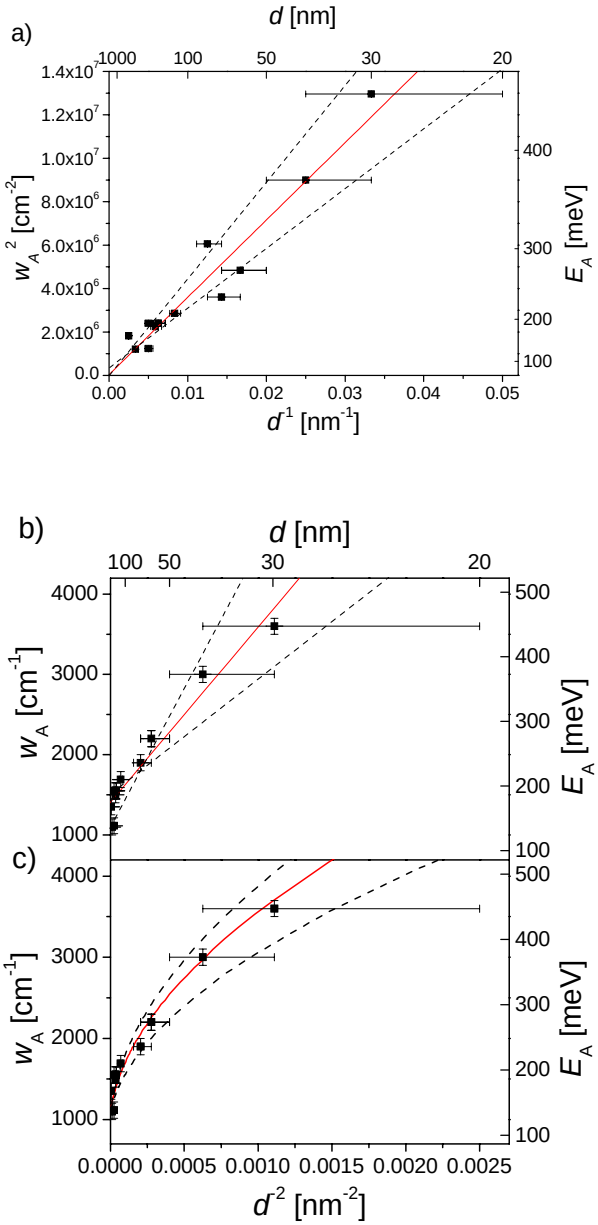

Figure 41: a) w_A^2 as a function of d^{-1}. b) w_A as a function of d^{-2} taking into account a constant electron effective mass while in c) the Lax two-band model is considered. The solid lines represent the respective best linear fits, and the dashed lines serve as approximation of the uncertainty. The uncertainty in determining the wavenumber of the absorption edge is estimated to ± 100 cm^{-1}.

In conclusion, infrared spectroscopic microscopy on single bismuth nanowires reveals an absorption whose onset is blueshifted with diminishing wire diameter. The absorption may be caused by excitation either of the plasma frequency or of direct transitions in the vicinity of the L-point. The observed blueshift is explained in the former case by surface defects that act as dopants, and thus increasing the charge carrier density and consequently ω_P. In the latter case, it is explained by quantum-size effects which shifts the band edges away from each other in energy.

Boyle and Rodgers reported on a pass band found in pure bismuth single crystals at 2 K for wavelengths between 20 μm {500 cm^{-1}} and 50 μm {200 cm^{-1}} [86]. The authors attributed the low-energy side to the plasma frequency and the high-energy side to a transition from lower lying states to the Fermi level. The incline of the recorded absorption spectra looks like a red edge of interband transitions, however, the value of $w_A \approx 1400$ cm^{-1} for the 400-nm wire seems to be high compared to results of thick-film transmittance studies. This certainly has a reason; the wire is much thinner than the film used in that work (~ 50 μm) [86], and neither the red tail of the interband absorption edge nor the blue tail of the plasma edge has been recorded. Therefore, it is more prabable that direct transitions in the vicinity of the L-point are reason for the absorption. Future experiments in the far-infrared regime where the plasma frequency of bulk Bi is located, should facilitate the determination whether the observed IR absorption originates from direct interband transitions or from ω_P.

In Fig. 42, the maximal absorption is plotted versus d^2. The data follow a linear dependence on d^2, i.e., the absorption maximum is directly proportional to the wire cross-section. Assuming that the aperture of the microscope was smaller than the length of the wires investigated, the effective length of all wire sections was the same and, hence, the maximal absorption is directly proportional to the wire volume. Some absorption data points have higher values than expected from the linear fit, which may be caused by three experimental uncertainties: (i) In the case of wires with a diameter of few ten nanometers, the limited resolution of the optical micropscope does not allow one to distingiush between one and two wires that are attached to each other. (ii) Some wires may be shorter than the aperture (8.3 μm) and, (iii) some wires may not be centered in the aperture so that the effective length may be smaller.

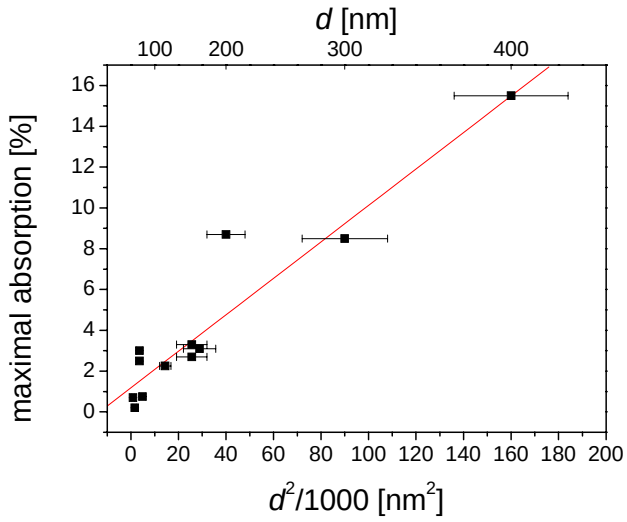

Figure 42:Maximal absorption of single bismuth nanowires as a function of d^2. The solid line represents the best linear fit.

IV.4.b IR spectroscopy as a function of beam polarization

Normalized infrared absorption spectra of single wires with diameters of 400, 120, and 60 nm for light that is polarized parallel and normal to the wire axis are presented in Figs. 43(a) and (b), respectively. Spectra of parallel polarized light reaches an almost constant value, whereas for normal polarized light the absorption passes through a maximum and declines again. In both cases, a blueshift of the absorption edge with diminishing wire diameter is observed, as is the case for unpolarized light. The absorption onset is located at higher energies in the case of light that is polarized normal to the wire axis compared to parallel polarized light.

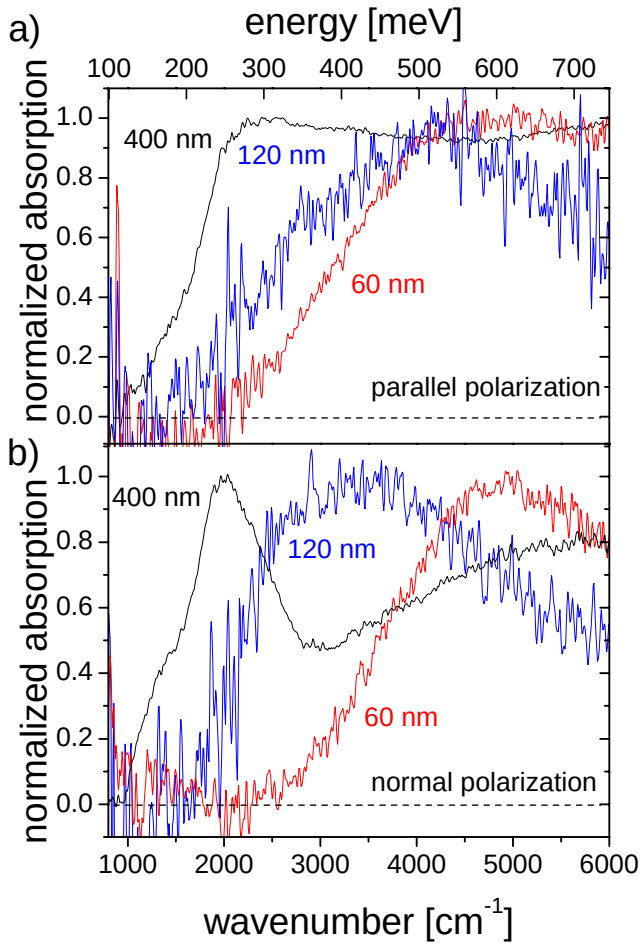

Figure 43: Normalized IR absorption spectra of single bismuth nanowires with diameters of 400, 120, and 60 nm for light that is polarized a) parallel and b) normal to the wire axis.

In Fig. 44, the blueshift of the absorption edge with respect to the onset for wires with diameter of 400 nm is displayed. It is larger for normal than for parallel polarized light. These findings may indicate the excitation of two different transitions by the two different polarizations of the incident IR light. These transitions are possibly due to direct transitions in the vicinity of the L-point and an indirect one from the L-point valence band to the T-point valence band. Surprisingly, some wires do not show any absorbance for light that is polarized normal to the wire axis. This may be explained by different crystalline orientations of the single wires.

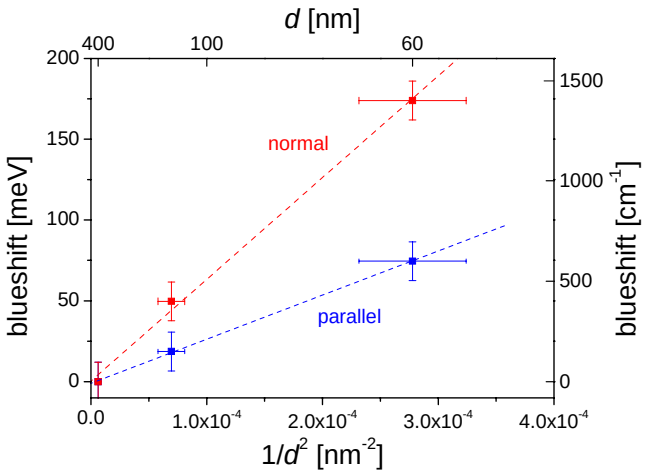

Figure 44: Blueshift of the absorption edge as a function of d^{-2} for normal and parallel polarized light.

Chapter V

ELECTRON ENERGY LOSS SPECTROSCOPY

V.1 Bulk and surface plasmons

Fast incident electrons as they are provided by transmission electron microscopes scatter inelastically from the electrons of a given sample. By Coulomb interaction the outer-shell electrons can undergo single-electron excitations, i.e., they are lifted to higher bound states, or the atoms are even ionised. As an alternative to single-electron excitations, outer-shell inelastic scattering may involve a collective oscillation of the electron density. This collective excitation is known as plasma resonance with a characteristic angular frequency ω_P [87]. In a first approximation, the plasma frequency is given by

$$\omega_P = \sqrt{\frac{e^2 n}{m\varepsilon_0}} \qquad \textbf{(22)}$$

where n is the charge carrier density and m the free electron mass.

In addition to bulk plasmons which are excited within the specimen, surface plasmons can be created at each exterior surface. These surface excitations are important in number only in very thin (< 20 nm) samples. The frequency of the surface plasmon ω_S depends on the

surroundings of the specimen, i.e., it is a function of the dielectric constant ε_D of the ambience:

$$\omega_S^2 = \frac{\omega_P^2}{1 + \frac{\varepsilon_D}{\varepsilon_0}} \tag{23}$$

In vacuum, the surface plasmon frequency amounts to $\omega_S = \omega_P / \sqrt{2}$.

The frequencies of bulk and surface plasmons are functions of the dielectric function ε [87]

$$\varepsilon = \varepsilon_1 + i\varepsilon_2 = \frac{\omega_P^2}{\omega_P^2 + \Gamma^2} = \frac{i\Gamma\omega_P^2}{\omega\left(\gamma^2 + \Gamma^2\right)} \tag{24}$$

where ε_1 and ε_2 are the real and imaginary parts of the dielectric function, Γ is a damping constant, and ω is the angular frequency of forced oscillations.

The conditions for the excitation of bulk and surface plasmons are $\varepsilon_1 = \varepsilon_2 = 0$ and $\varepsilon_1 = -1$, respectively [90]. If interband transitions occur at energies lower than the plasmon energy $E_P = \hbar\omega_P$, E_P is likely to increase above the free-electron value and vice versa [87].

For Bi, the surface plasmon condition ($\varepsilon_1 = -1$) is fullfilled at 6 eV, but $\varepsilon_2 = 3.5$ is relatively important. Thus, the main surface plasmon is observed at 11 eV where $\varepsilon_1 = -0.75$ and $\varepsilon_2 = 1.15$. In the same manner, the 14 eV bulk plasmon corresponds to $\varepsilon_1 = 0.06$ and $\varepsilon_2 = 0.5$ [88] which does not fit exactly to the classical resonance condition. The electron energy loss spectrum of a bismuth film is displayed in Fig. 45 [89] showing both plasmon resonances. At 0 eV energy loss, a pronounced feature is observed – the so-called zero-loss peak (ZLP). The ZLP represents all electrons that are not scattered in the specimen. At an energy loss of 24 eV, a resonance is observed caused by electrons from the atomic shell O4, 5 being lifted into the continuum, i.e., the atoms are ionised. According to P. Zacharias, two separate resonances occur at 24.6 and 27.8 eV, corresponding to the exciation of electrons from the O4 and O5 atomic shell, respectively [90]. Note that the thicker the specimen is, the more probable are multiple scattering events of the incident electrons. For instance, double plasmon excitations occur as a resonance at 2 $E_P = 28$ eV. Further, a faint structure at around 50 eV energy loss is observed that is caused most probably by photionization of the *5d* subshell [88].

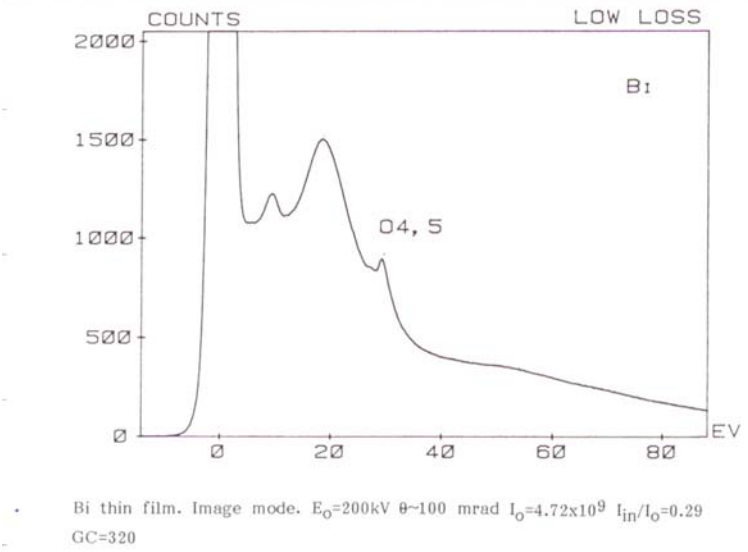

Figure 45: Typical electron energy loss spectrum of a bismuth thin film (taken from [89]).

Due to the boundary effect the probability for generating bulk plasmons is reduced if the thickness of the object under investigation is less than

$$\frac{\pi v}{2\omega_P} = \frac{\lambda_w}{4} \tag{25}$$

where λ_w represents the wavelength of potential and electron density oscillation at ω_P, which is caused behind a charged particle penetrating matter and which travels with velocity v.

EELS was performed at a transmission electron microscope (JEOL, JEM-3010) that operates at 300 kV and has a point resolution of 1.7 Å. The microscope is equipped with a Gatan imaging filter (GIF) for energy filtered images and acquisition as well as for analysis of EEL spectra. For 300 keV electrons in Bi, the boundary effect is expected for specimens of thickness < 17 nm.

V.2 Electron energy loss spectroscopy on Bi nanowires

In Fig. 46(a), an electron energy loss spectrum for wires of diameter 100 nm is displayed, showing the zero-loss peak at 0 eV energy loss. The energy resolution is given by the full width at half maximum (FWHM) of the ZLP which amounts in this case to about 2.4 eV. At finite energy loss, small peaks are observed in the spectrum. By deflecting the zero-loss electrons, the sensitivity of the detector is increased so that the plasma resonance can be resolved in more detail (Fig. 46(b)). It reveals resonances at about 15 and 28 eV as well as a broad feature between 40 and 100 eV energy loss. The dashed line indicates the background which is subtracted in order to receive the low-energy loss spectrum depicted in Fig. 46(c). This spectrum shows a pronounced resonance at around 15 eV which originates from plasmon excitations in Bi. The peak can be deconvoluted into two Gaussians with maxima at around 14.9 and 10.4 eV - originating from the excitation of bulk and surface plasmons, respectively. The FWHM amounts to 5.9 eV which is in good accordance with reference [88]. The feature between 24 and 32 eV energy loss is based on two different mechanisms. On the one hand, it arises from ionisation of outer-shell electrons in bismuth (O4,5 excitations) and, on the other hand, it is caused by plasma resonance excitations in carbon from the TEM grid. Additionally, energy losses of about 28 eV may occur due to double plasmon excitations in the Bi nanowire.

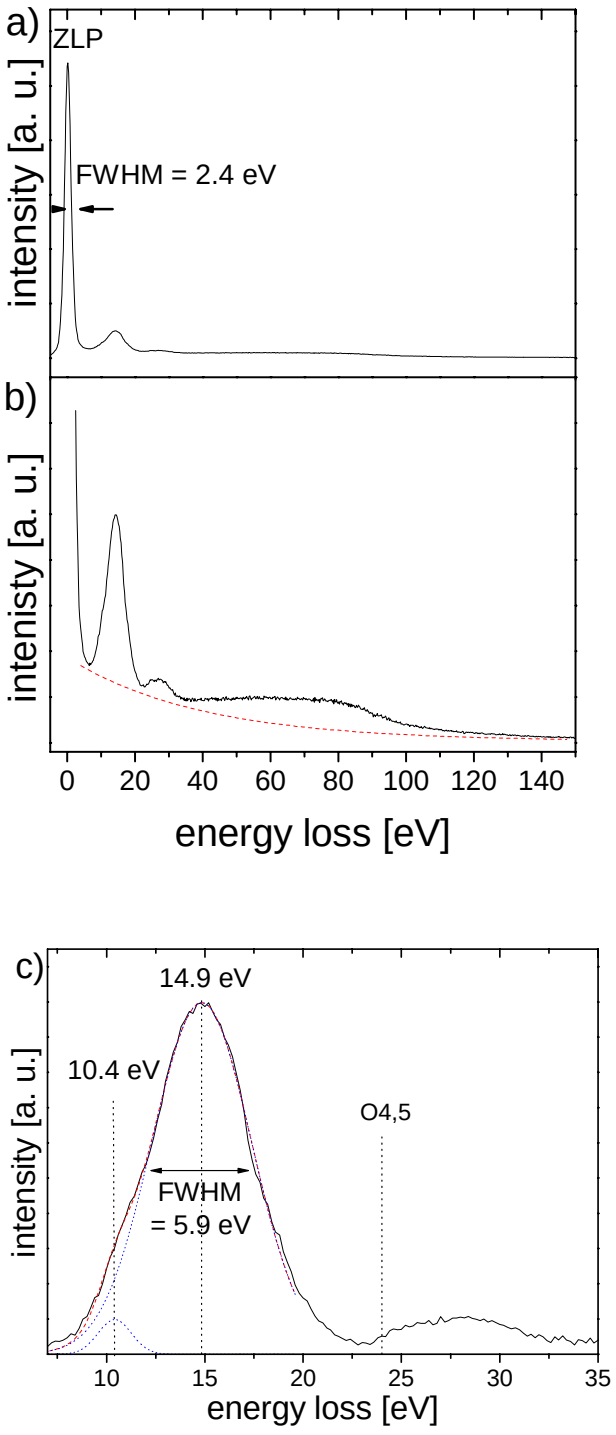

Figure 46: Electron energy loss spectrum of a bismuth nanowire with a diameter 100 nm a) with and b) without zero-loss peak. c) Low-energy loss spectrum, after subtracting the background, being indicated by the dashed line in part (b).

Electron energy loss spectra of wires of diameters 100, 70, and 30 nm, where the background was already subtratced, are presented in Fig. 47. The spectra are normalized to the energy loss at 24 eV. It is observed that the resonance originating from bismuth bulk plasmons is the more pronounced the thicker the wire under investigation is. This is expected since thicker wires possess more electrons due to their larger volume. Furthermore, wires of larger diameters show a stronger energy loss at about 30 eV, which could be caused by double plasmon excitation of the incident electrons. The probability for double plasmon excitations grows with increasing sample thickness.

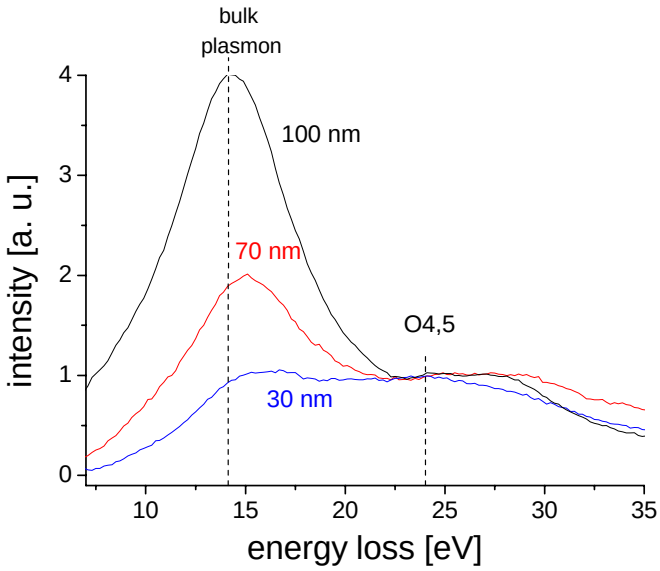

Figure 47: Electron energy loss spectrum of bismuth nanowires with diameter 100, 70, and 30 nm.

In Figs. 48(a), (b), and (c), the EEL spectra of the figure before are shown separately. Two Gaussians are fitted to the spectra, in order to subtract the influence of single-electron excitation at 24 eV and the excitation of the plasma resonance in carbon, and for obtaining both the energy and FWHM of the plasma resonance in Bi nanowires. In the case of the wires with diameter 70 and 30 nm, no significant contribution from the 10 eV surface plasmon of bulk bismuth was found. E_P amounts to 14.4, 15.2, and 14.8 eV for wires of diameters 100, 70, and 30 nm, respectively. With respect to the energy resolution amounting to ~ 2 eV, no change of the volume plasmon energy can be observed. The same is true for the width of the resonance ranging from 5.5 to 6 eV. In contrast, Sander et al. [91] observed a blueshift of about 1 eV of the bulk plasmon energy for Bi nanowires with diameter 35 nm compared to 90-nm diameter wires. This is surprising, because in metallic and semiconductor

nanostructures a blueshift is expected for wires of diameters less than 10 nm. The authors offer several possible origins: quantum-size effects, localized strain, and interface effects.

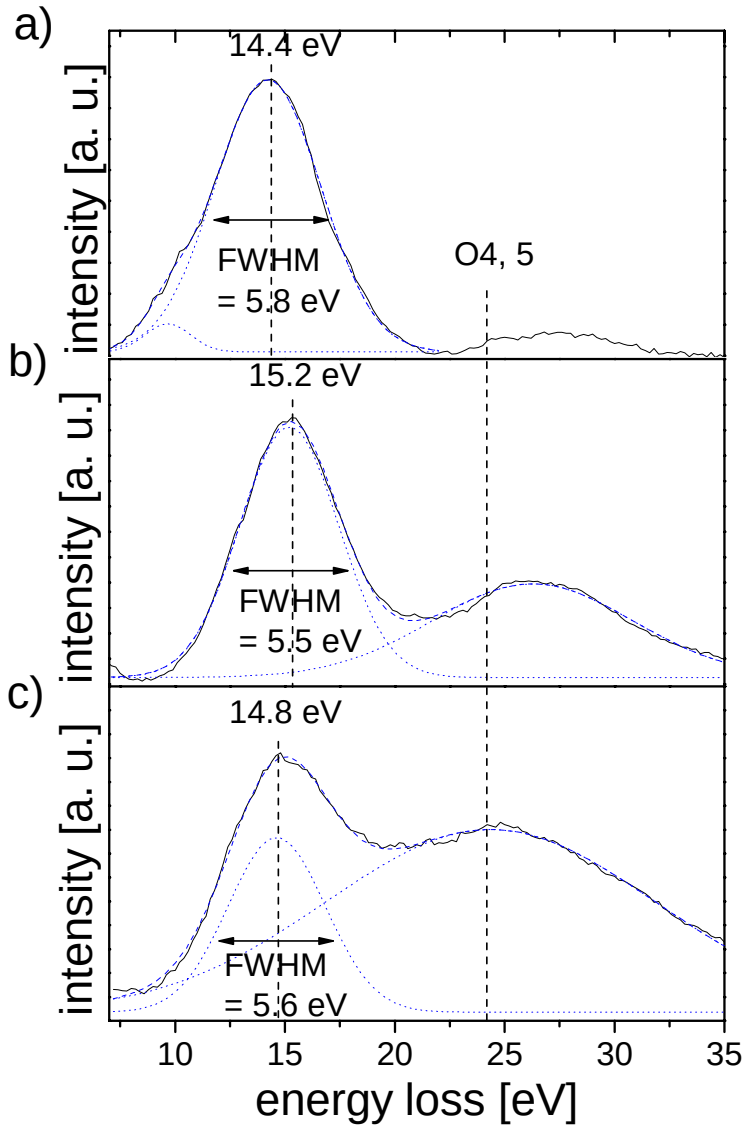

Figure 48: Electron energy loss spectrum of bismuth nanowires with diameter a) 100, b) 70, and c) 30 nm. Two Gaussians are fitted to the spectra in order to derive both the position and width of the plasma resonance.

Chapter VI

FINITE-SIZE EFFECTS

VI.1 Finite-size effects

The electrical resistance R of a cylindrical solid is given by

$$R = \frac{1}{\sigma} \cdot \frac{4L}{\pi \cdot d^2} \tag{26}$$

where σ is the material-dependent specific electrical conductivity, d is the diameter, and L is the length of the cylinder. σ is a function of the mobility as well as of the density of the charge carriers in the conduction band. In the case of bismuth, two kinds of carriers – electrons and holes – contribute to the electrical current. In equation (27), μ and ν are the mobilities, and n and p are the concentrations of electrons and holes, respectively [92].

$$\sigma = e\left[n(T)\mu(T) + p(T)\nu(T)\right] \tag{27}$$

The carrier mobility is a function of the carrier effective mass and the mean scattering time τ.

$$\mu = \frac{e\tau}{m^*} \tag{28}$$

Due to the highly anisotropic Fermi surfaces, the carrier effective masses and, hence, mobility and specific electrical conductivity depend on the crystalline orientation.

When the size of an object is comparable to the mean free path l_e of the conduction electrons, finite-size effects - also called mesoscopic effects - occur. They include, in particular, electron scattering from the wire surface as well as from grain boundaries. In the following sections, the influence of these scattering effects on the electrical conductivity are discussed.

VI.1.a Electron scattering from nanowire surface

In the 1930s, K. Fuchs developed a theory in order to treat the influence of electron scattering processes at the surface of thin films on the electrical transport properties [1]. About two decades later, R.B. Dingle extended this theory to wires having a circular cross-section [2]. Both theories are based on the assumption of spherical Fermi surfaces. According to Dingle, electron scattering from the wire surface contributes to the electrical resistivity and depends on the ratio k of wire diameter and electron mean free path

$$k = \frac{d}{l_e} \tag{29}$$

as well as on the specularitiy ε of the scattering processes. The smaller k is, the more electrons may travel from one to the other side of the wire, being thus scattered from the surface. In order to point out the effect of the specularity on the electron momentum, completely specular ($\varepsilon = 1$) and diffuse ($\varepsilon < 1$) scattering are sketched in Fig. 49. In the former case the electron momentum $\vec{p}$ along the wire axis is unaffected, whereas in the latter one the component of $\vec{p}$ parallel to the cylindrical axis changes. Thus, for $\varepsilon = 1$ the electrical conductivity is not affected, at least if the Fermi surface does not deviate from a spherical shape. In the following paragraphs, the influence of the specularity for $\varepsilon \neq 1$ on the electrical conductivity is discussed in more detail.

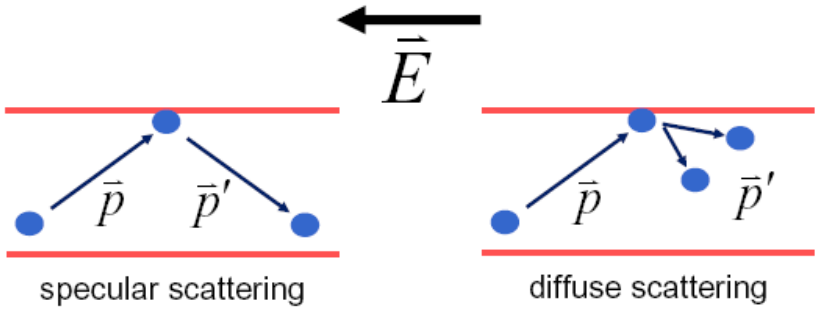

Figure 49: Schematic of specular and diffuse scattering of electrons from the wire surface. *E* is the applied electrical field.

Equation (30) shows that the conductivity is a function of both the current density passing along the wire $j(r)$ and the current density in bulk material j_0

$$\frac{\sigma}{\sigma_0} = \frac{\int_0^d j(r)dr}{\int_0^d j_0 \cdot r \cdot dr} = \frac{2}{d^2}\int_0^d \frac{j(r)}{j_0} \cdot r \cdot dr \qquad (30)$$

where r is the distance of the electron to the longitudinal symmetry axis of the cylinder.

Classically, the bulk current density is a function of the electrical field E and the charge carrier properties, namely density n, charge q, mean scattering time τ, and mass m.

$$j_0 = E \cdot \sigma = \frac{n \cdot q^2 \cdot E \cdot \tau}{m} \qquad (31)$$

In the most general case, the ratio of the current densities in nanowires and bulk material is expressed by equation (32) that is given in cylindrical polar coordinates, where v is the velocity of the electron.

$$\frac{j(r)}{j_0} = 1 - \frac{6}{\pi}(1-\varepsilon)\sum_{v=0}^{\infty}\varepsilon^v \int_0^{\pi/2} d\theta \cos^2\theta \sin\theta \int_0^{\pi/2} d\phi \cosh\left(\frac{r\sin\phi}{l_e \sin\theta}\right)\exp\left(-\frac{(2v+1)\left(d^2 - r^2\cos^2\phi\right)^{\frac{1}{2}}}{l_e \sin\theta}\right) \qquad (32)$$

In order to obtain the conductivity ratio, this expression has to be integrated over the radial dimension of the wire resulting in

$$\frac{\sigma}{\sigma_0} = 1 - \frac{12}{\pi}(1-\varepsilon)^2 \sum_{\nu=1}^{\infty} \nu \varepsilon^{\nu-1} \int_0^1 \sqrt{1-x^2}\, S_4(\nu k x)\, dx \qquad \textbf{(33)}$$

with

$$S_n = \int_0^{\pi/2} \exp\left(-\frac{u}{\sin\theta}\right) \cos^2\theta \sin^{n-3}\theta\, d\theta \qquad \textbf{(34)}$$

and

$$S_{n-1} = -\frac{\partial S_n}{\partial u}. \qquad \textbf{(35)}$$

Equation (33) may be approximated for the cases that the wire diameter is either much larger or much smaller compared to the electron mean free path.

k >> 1:

$$\frac{\sigma}{\sigma_0} \approx 1 - \frac{3}{4k}(1-\varepsilon) + \frac{3}{8k^3}(1-\varepsilon)^2 \sum_1^{\infty} \frac{\varepsilon^{\nu-1}}{\nu^2} \qquad \textbf{(36)}$$

k << 1:

$$\frac{\sigma}{\sigma_0} = \frac{1+\varepsilon}{1-\varepsilon} k - \frac{3k^2}{8}\left[\frac{1+4\varepsilon+\varepsilon^2}{(1-\varepsilon)^2}\left(\ln\frac{1}{k} + 1.059\right) - (1-\varepsilon)^2 \sum_1^{\infty} \nu^3 \varepsilon^{\nu-1} \ln\nu\right] - \frac{2k^3}{15}\frac{1+11\varepsilon+11\varepsilon^2+\varepsilon^2}{(1-\varepsilon)^2} \qquad \textbf{(37)}$$

In the following, the approximations are evaluated for two special cases, namely that the scattering from the wire surface is completely diffuse ($\varepsilon = 0$) or partially specular ($\varepsilon = 0.5$).

$k >> 1$, $\varepsilon = 0$:

$$\frac{\sigma}{\sigma_0} = 1 - \frac{3}{4k} + \frac{3}{8k^3} \cdots \quad \textbf{(38)}$$

$k << 1$, $\varepsilon = 0$:

$$\frac{\sigma}{\sigma_0} = k - \frac{3k^2}{8}\left(\ln\frac{1}{k} + 1.059\right) - \frac{2k^3}{15} \quad \textbf{(39)}$$

$k >> 1$, $\varepsilon = 0.5$:

$$\frac{\sigma}{\sigma_0} = 1 - \frac{0.375}{k} + \frac{0.109}{k^3} \quad \textbf{(40)}$$

$k << 1$, $\varepsilon = 0.5$:

$$\frac{\sigma}{\sigma_0} = 3k - 11.22k^2\left(\log\frac{1}{k} - 0.245\right) - 9.74k^3 \quad \textbf{(41)}$$

The specific electrical resitivity of nanowires compared to the bulk value is presented in Fig. 50 as a function of the specularity of the electron scattering processes, and of the ratio of wire diameter and electron mean free path. ρ/ρ_0 reveals a strong increase for $k < 1$, i.e. $d < l_e$. For wires with diameters much bigger than the electron mean free path ($k > 10$), electron scattering from the wire surface has almost no effect on the resistivity. The more scattering processes are diffuse, the more pronounced is the resistivity increase. Since in bismuth $l_e \sim$ 100 nm at room temperature, the wire resistance should be affected by surface scattering for wires with diameters less than 200 nm.

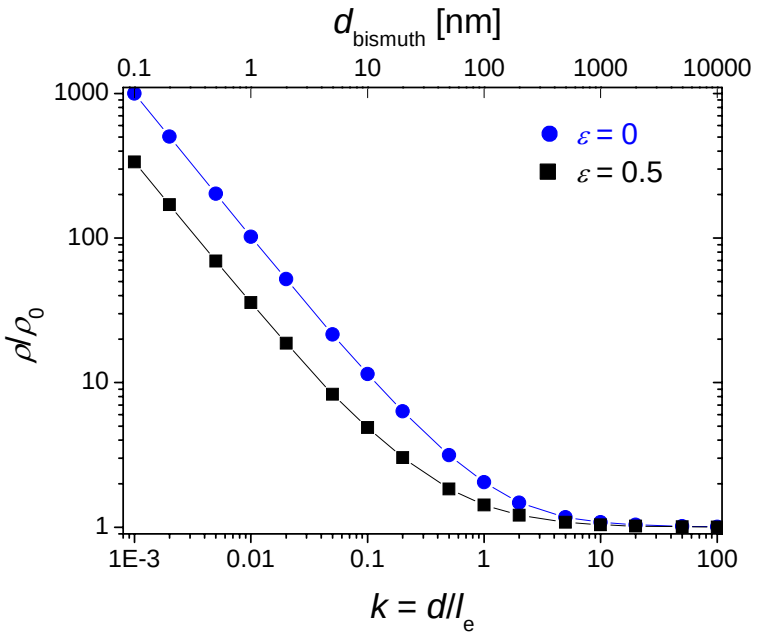

Figure 50: Specific electrical resistivity of nanowires compared to the bulk value as a function of $k = d/l_e$ and specularity ε.

It has to be pointed out that the calculations above are only valid for spherical Fermi surfaces. P.J. Price [93] as well as F.S. Ham and D.C. Mattis [94] found that there is a size dependence of the electrical conductivity even for specular scattering, if the energy surfaces are non-spherical. In particular, the conductivity of progressively thinner single crystals reaches a limiting value, which is a function of both the shape of the energy surfaces and orientation with respect to the crystalline axis. The saturation of the conductivity for specular scattering is in contrast to the case of diffuse reflection, where the conductivity decreases monotonically with diminishing sample size for both the spherical and non-spherical energy surfaces. J.E. Parrott [95], and M. Barati and E. Sadeghi [96] extended the theories for thin films and nanowires, provided by K. Fuchs and R.B. Dingle, to non-spherical Fermi surfaces. In their approaches, they take into account the angle θ between the direction of the electron motion and the boundary normal. It is assumed that below a critical angle θ_0 the electron scattering is totally specular, while above θ_0 the scattering becomes completely diffuse. This very simple approach leads to an effective conductivity that approaches a constant value for sufficiently thin specimen, whereas the theories of Dingle and Fuchs predict a continuously decreasing conductivity. For bismuth nanowires oriented normal to the trigonal axis, as is the case for the wires presented in this work, the conductivity can be written as

$$\sigma_{zz} = \frac{\sigma_0 \alpha_1}{\sqrt{\det \alpha}} \left[1 - \frac{6}{k} \int_{\mu_0}^{1} \exp\left(-\frac{k}{2\mu} \right) \left[1 - \exp\left(-\frac{k}{2\mu} \right) \right] \mu^2 \sqrt{1-\mu^2}\, d\mu \right] \qquad \textbf{(42)}$$

where $\mu = \sin\theta$, and α is the reciprocal mass tensor [96]. The conductivity ratio $\sigma_{zz}/\sigma_{zz}^{bulk}$ as a function of the critical angle of incidence and k is displayed in Fig. 51. It reaches unity for wire radii being large compared to the mean free path. In this case, $\sigma_{zz}/\sigma_{zz}^{bulk}$ is independent of μ_0 while it decreases rapidly for diminishing k. The deviation from the bulk conductivity is strongly affected by the critical angle of incidence. The ratio approaches 0.05 for $k = 0.02$ and $\mu_0 = 0.1$, i.e., $\theta_0 = 5.7°$. As the value of μ_0 rises, electron scattering from the wire surface becomes more specular, and hence less size-effect is expected in the conductivity of the wire. A small value of the critical angle of incidence indicates a big amount of diffuse scattering processes, and thus a pronounced size effect is expected. However, for increasing wire diameters the relative contribution of diffuse scattering processes to the electron-phonon interaction diminishes, so that the size effect of wires, whose radius is large compared to l_e, becomes negligible, also for large μ_0.

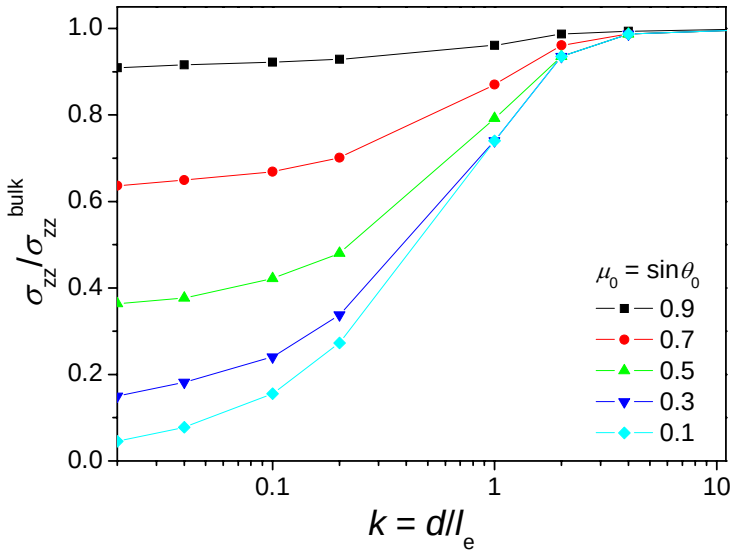

Figure 51: Conductivity ratio as a function of $k = d/l_e$ and critical angle of incidence $\mu_0 = \sin\theta_0$ [96].

VI.1.b Electron scattering from grain boundaries

In the 1970s, A.F. Mayadas and M. Shatzkes investigated theoretically the influence of grain boundaries on the electrical resistance of thin films [43]. Grain boundaries can be regarded as potential barriers which have to be overcome by the electrons. In the simplest case, the potential $V(x)$ can be described by a δ-function where S is the potential height and x_n the position of the n-th potential barrier.

$$V(x) = S\sum_n \delta(x - x_n) \tag{43}$$

The electrons may be scattered from the potential barriers being schematically depicted in Fig. 52. The scattering processes lead to a higher specific electrical resistivity.

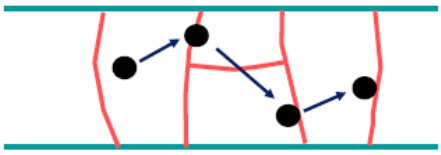

Figure 52: Schematic of electron scattering from grain boundaries.

The influence on the resistivity depends on three parameters – the mean grain size D, the electron mean free path, and the reflectivity $\mathscr{R}$ of the grain boundaries, i.e., the fraction of electrons that is scattered from them. In bulk material the effect of grain boundaries on the resistivity is negligible because the grains are much larger than the electron mean free path. In the case of thin films and nanowires, the grain size becomes important since D is comparable to l_e. The three parameters that determine the influence of the scattering at grain boundaries – $\mathscr{R}$, D, and l_e – are combined in the coefficient α [43].

$$\alpha = \frac{m}{\hbar^3 d}\frac{S^2}{k_F}2\tau = \frac{l_e}{D}\frac{\mathscr{R}}{1-\mathscr{R}} \tag{44}$$

Figure 53 displays α vs. $\mathscr{R}$. The coefficient α increases if the wire is built up by grains that are small compared to l_e, possessing very low-reflecting boundaries, or when it consists

of larger grains that exhibit highly reflecting boundaries. For instance, α amounts to 1 for grains with sizes of $l_e/D = 0.1$ and $l_e/D = 10$, reflecting 90 % and 10 % of the charge carriers, respectively.

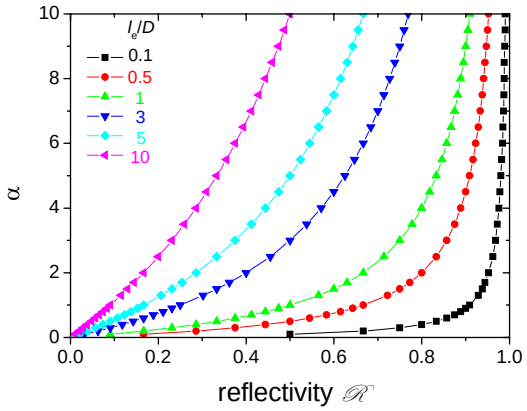

Figure 53: Coefficient α as a function of the grain boundary reflectivity for various l_e/D.

The influence of the electron scattering from grain boundaries on the electrical resistivity is given by equation (45) which is exclusively a function of α.

$$\frac{\sigma_g}{\sigma_0} = \frac{\rho_0}{\rho_g} = 3\left[\frac{1}{3} - \frac{1}{2}\alpha + \alpha^2 - \alpha^3 \ln\left(1 + \frac{1}{\alpha}\right)\right] \qquad \textbf{(45)}$$

The relation between α and ρ/ρ_0 is depicted in Fig. 54, showing that the specific electrical resistivity increases with rising α. The increase can be caused either by smaller grains or by grain boundaries with higher reflectivity as mentioned above. For instance, in the cases that α amounts to unity and ten, the resistivity rises by a factor of two and fourteen, respectively.

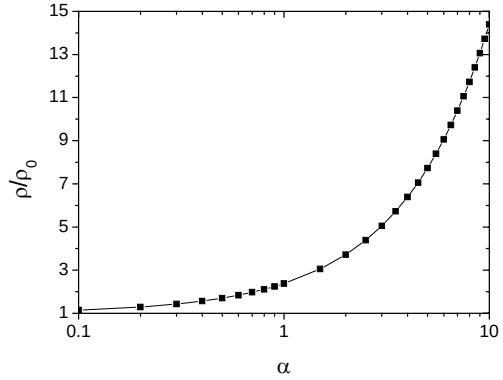

Figure 54: Specific electrical resistivity of a nanowire as a function of coefficient α which is determined by the grain boundary reflectivity.

VI.2 Experimental techniques

Transport properties of bulk Bi [97] as well as of thin films [9, 46] have been extensively studied in the past. Measurements on Bi nanowires were in most cases performed on wire arrays embedded in alumina matrices and thus did not provide absolute values of the wires' specific electrical resistivity [12, 13, 21, 98]. Only few works reported on the examination of transport properties of single wires. On the one hand, single wires have been prepared by an electron beam writing technique on Si substrates. This method does not allow one to tailor the wire crystallinity. These wires exhibited a resistivity five times larger than the bulk value. The authors attributed this observation to very small mean grain sizes [17]. On the other hand, wire arrays have been fabricated by pressure injection in alumina templates. In order to have access to a single wire, the matrix was subsequently removed by strong acids, and a single wire was contacted lithographically [25]. This method provides the possibility of performing four-point measurements in order to obtain the contact resistance. However, during matrix dissolution a thick oxide coating is formed, thus preventing reliable resistance measurements.

VI.2.a Contacting single nanowires electrically

In this work, single Bi nanowires, which are created as described in Chapter II, are left embedded in the template, thus preventing both their oxidation and possible chemical reactions with a solvent. Single wires are created under three different deposition conditions: (I) T = 30 °C, U = -50 mV, (II) T = 50 °C, U = -25 mV, and (III) T = 60 °C, U = -17 mV. In each case, the deposition is continued until a cap of several micrometers in size is formed on top of the wire. In order to determine the electrical resistance of a single wire, the cap is coated by a second gold layer [18, 99] and subsequently the sample (PC membrane with embedded wire) is placed between two macroscopic copper plates. The upper electrode is caved in its centre for avoiding direct pressure on the nanowire cap. The experimental setup is schematically displayed in Fig. 55.

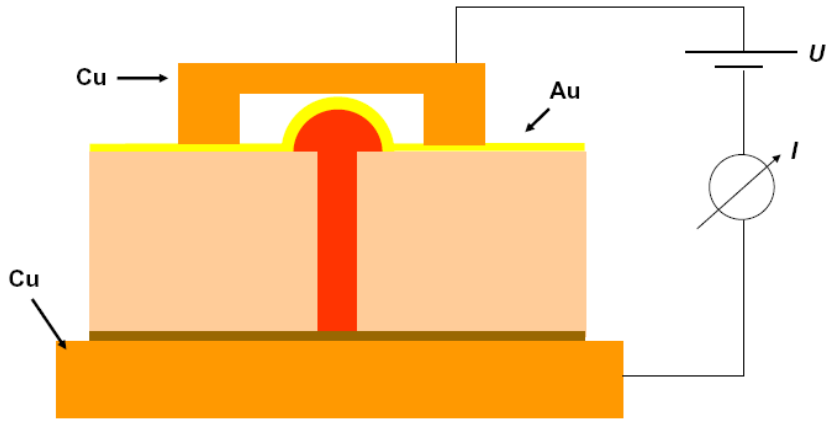

Figure 55: Scheme of the experimental setup for contacting single bismuth nanowires.

VI.2.b Experimental setup for resistivity measurements at low T

Experiments on the resistance of single wires as a function of the temperature are performed in a vacuum chamber that is equipped with a cryostat. In the first section, an overview of both the vacuum chamber and cryostat is presented. A more detailed description of the cooling system can be found in the dissertation of M. Thier [100]. The second part focuses on the sample holder used for measurements of the electrical resistance of single bismuth nanowires as a function of temperature, and the third section deals with the cooling process of the sample holder.

VI.2.b.i Cryostat

The experimental setup for low-temperature measurements consists of a vacuum chamber and an inverted liquid-helium flow cryostat, being presented in the photograph of Fig. 56(a). Part (b) shows a scheme of the cryostat whose central parts consists of a double-walled tube with a spacing at the tube ending. At the upper end, the experimental platform is installed. Liquid helium is transferred from the dewar to the cryostat by a helium lifter which is immersed into the dewar, a double-walled corrugated tube, and a cooling finger which is introduced into the cryostat, so that the experimental copper platform is right above the evaporation nozzle of the cooling finger. In order to transfer the liquid gas to the cryostat, an over-pressure of 100 – 300 mbar is needed which is directly produced by the evaporation of

liquid helium when the helium lifter is cooled to 4.2 K after introducing it into the dewar. This over-pressure is maintained during the whole measurement by using gaseous helium from a bottle connected to the dewar. The liquid-helium flux and therefore the cooling power of the system is regulated by the over-pressure and by a needle valve at the helium lifter. In order not to consume too much helium, the double-walled corrugated tube has to be thermally isolated from the environment. For this purpose, the spacing is evacuated down to 10^{-5} mbar. The liquid helium evaporates at the nozzle of the cooling finger, i.e., just below the experimental platform which is cooled by this process. The gaseous helium flows through the outer tube of the cryostat to a valve where it leaves the system. The cold gas serves additionally for cooling a radiation shield surrounding the cryostat.

Since the vacuum chamber is at room temperature, it emits the corresponding black body radiation. In order to isolate the sample from this radiation, it is shielded by an aluminium cylinder that is covered by twenty additional layers of special isolating foils. While the outermost foil is exposed to the 300 K radiation of the chamber, the next foil is heated up only by 150 K radiation, and so on. The radiation shield is connected to the shielding of the cryostat which is cooled by the back flowing cold gaseous helium. Hence, this shield possesses a temperature well below 100 K. On the bottom of the experimental platform next to the evaporation nozzle of the cooling finger, a Si diode is placed in order to control the cooling power of the cryostat.

In order to isolate the experimental setup thermally from the environment and for preventing ice-formation when cooling down, the surrounding chamber is evacuated by both a rotation pump and a turbo pump. Pressures $< 10^{-5}$ mbar are reached already after one hour of evacuation. While cooling down, the vacuum improves since the cooled surfaces act as a cooling trap so that pressures of less than 10^{-7} mbar are possible.

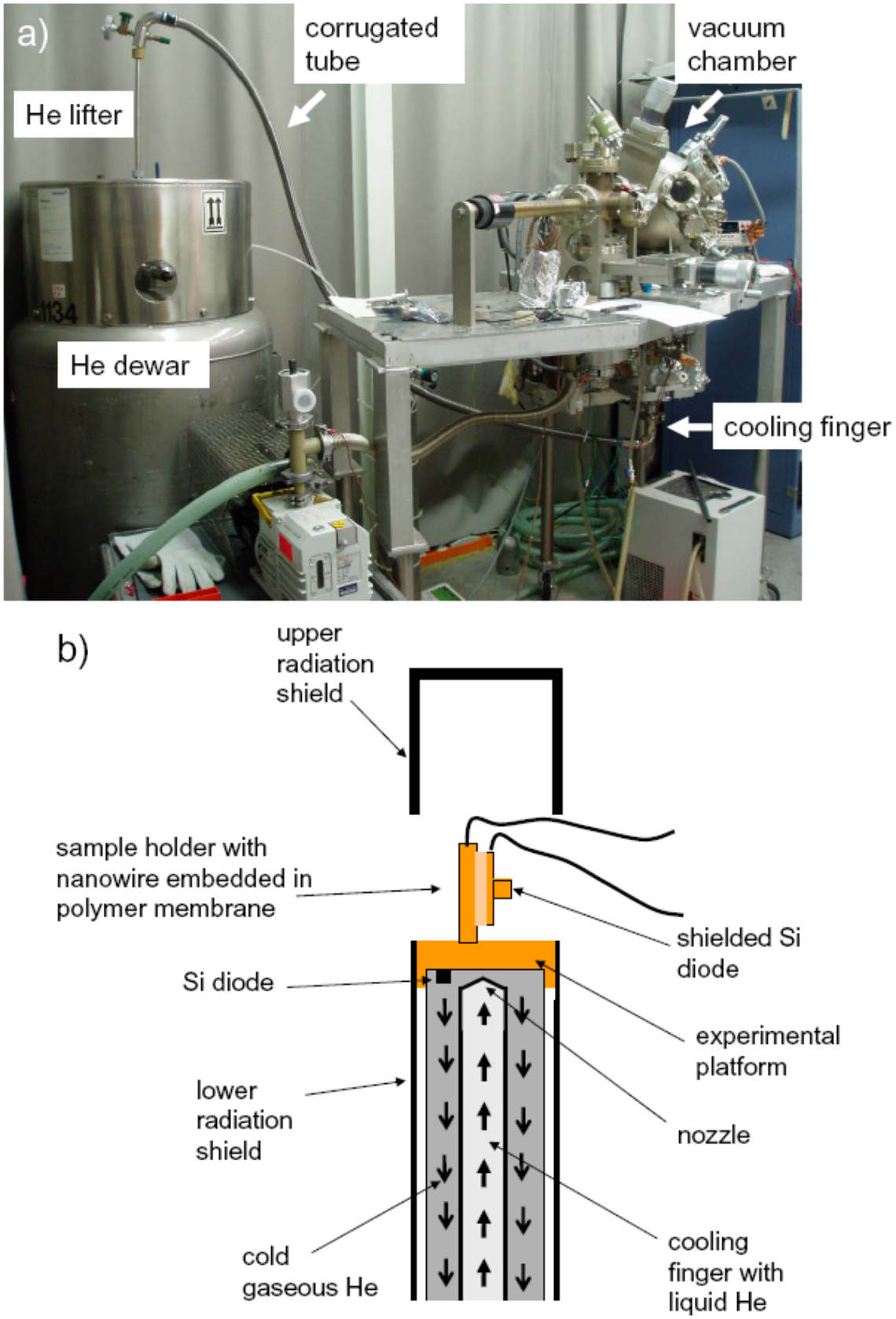

Figure 56: a) Photograph of the vacuum chamber with inverted liquid-helium cryostat, helium lifter, and helium dewar. b) Schematic of the cryostat.

VI.2.b.ii Sample holder

The sample holder (Fig. 57(a)) employed for contacting and measuring the electrical resistance as a function of T consists of two copper electrodes that are thermally coupled to each other via four sapphire crystals. In order to minimise the thermal resistance, the different interfaces are covered by thermally conductive paste. For maintaining a reliable electrical contact, the electrodes are tightly bolted using nylon screws. Since both the sapphire crystals and nylon screws are electrically insulating materials, the electrical current is conducted only by the nanowire. The temperature of the sample is measured by a Si diode which is placed at the point most distant from the cryostat, on top of one of the copper plates. It is shielded separately by a copper cap being cooled via the sample holder (see Fig. 57(b)). This additional shielding minimizes the uncertainties of the temperature measurement. Without this separate shielding, the temperature measured at the diode is about 15 K higher than the sample temperature at $T_{sample} \sim 20$ K, representing an enormous relative error.

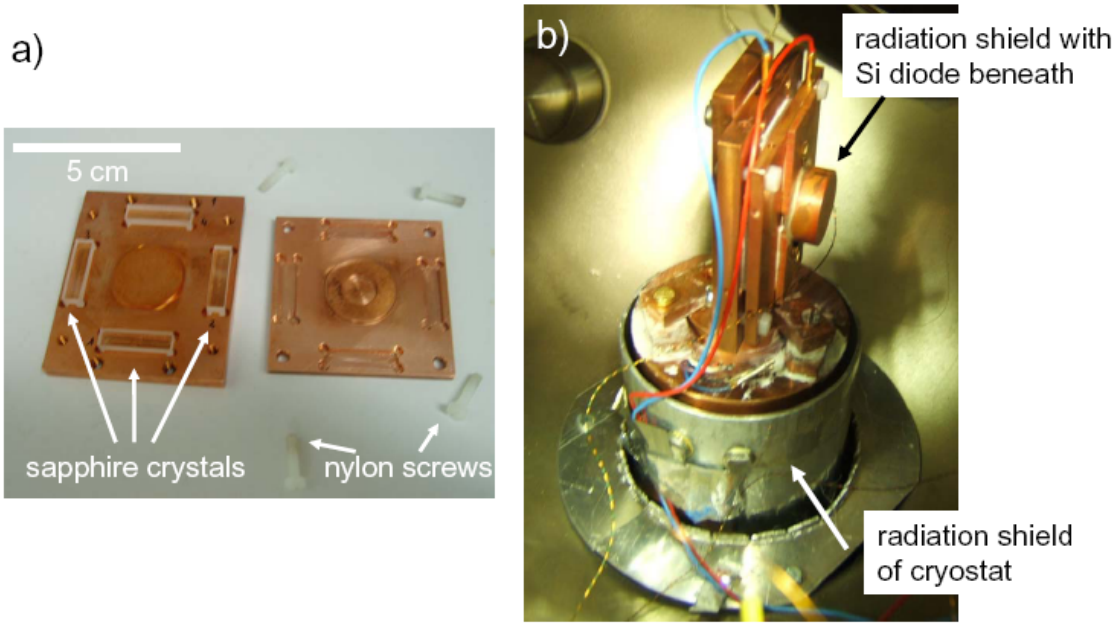

Figure 57: a) Sample holder for measurements of the electrical resistance of single bismuth nanowires as a function of temperature. b) Sample holder mounted on top of the cryostat.

The electrical resistance of the sample is measured by means of a Keithley 2400 SourceMeter. This instrument as well as the thermal couple are read out by a LabVIEW program, so that resistance versus temperature curves can be displayed during the experiment. The SourceMeter has a voltage and current resolution of 1 μV and 1 pA, respectively. In order not to harm the wire by too high current densities or Joule heat, currents of only few

microampères are applied. This leads to current densities of the order of 10^3 A cm^{-2} for wires with a diameter of few hundred nanometers. The thermal power is of the order of a few nanowatt depending on the wire resistance. This power and the small dimensions of the wires lead to a heating rate of few millikelvin per second. This energy can be easily either emitted by radiation or transported by thermal conductivity so that the applied thermal power is negligible for the experiments.

VI.2.b.iii Analysis of cooling process

In order to obtain reliable data of the resistance as a function of T, no temperature gradient should exist along the wires. On the one hand, temperature gradients involve potential differences that originate from thermoelectric voltage. On the other hand, they prevent the determination of the exact temperature of the wire. In order to minimize such gradients, the thermal coupling between cryostat and sample holder has to be as good as possible. Additionally, the shielding should protect the sample against heating by thermal radiation. In order to determine the quality of the thermal coupling and the efficiency of the radiation shield, the cooling as well as the heating process are analyzed. For this purpose, the temperatures of the Si diodes next to the cooling finger and on top of the sample holder are recorded simultaneously. Figures 58(a) and (b) present the temperature as a function of time during the cooling and heating cylces, respectively. The heating process is performed passively, i.e., the sample is heated up exclusively by thermal radiation. The cooling process lasts about 20 min, reaching a minimum temperature of about T_{min} = 20 K at the sample holder. The temperature of the sample holder follows the temperature of the experimental platform with a very small delay, indicating a very good thermal coupling between cryostat and sample holder. In the case of such fast cooling processes, temperature gradients between experimental platform and sample holder of up to 50 K are observed. The duration of the warming up is much longer than the cooling processes. Almost a full day is needed to reach room temperature indicating that the experimental setup is shielded well against heat radiation. The temperature gradient during the heating cycle is negligible, being in the order of a few Kelvin. In order to minimize the error of the temperature measurement and to avoid thermoelectric voltages during the experiments, resistance versus temperature curves are recorded while warming up the sample.

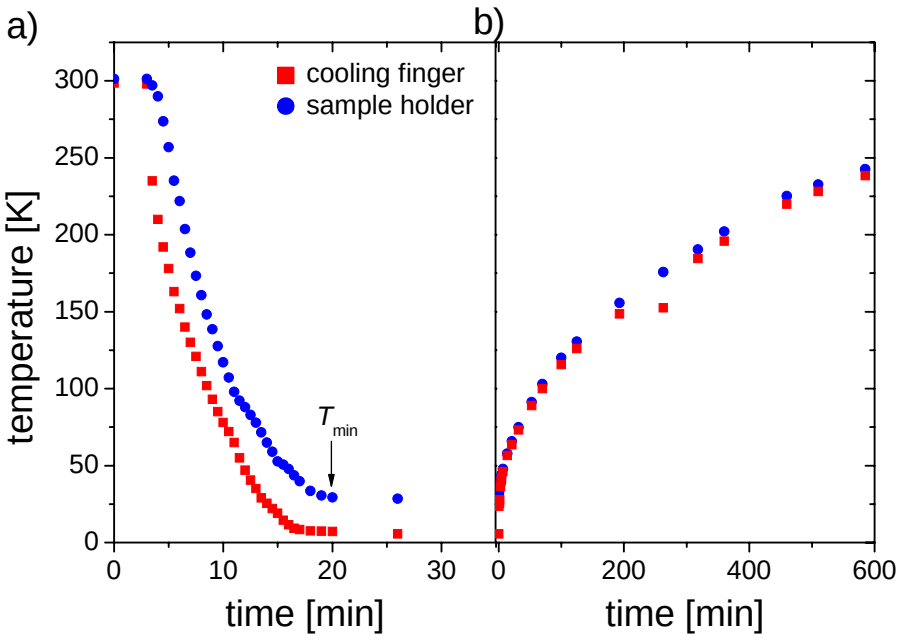

Figure 58:Temperature next to the cooling finger where liquid helium evaporates, and on top of the sample holder at the most distant point to the cryostat during a) cooling and b) heating cycle.

VI.3 Electrical transport properties of single bismuth nanowires

SEM images of caps grown on top of single Bi nanowires of similar diameter which were deposited under the conditions (I), (II), and (III) are depicted in Figs. 59(a), (b), and (c). These micrographs reveal that the size of the grains building up the caps increases from wires of type (I) to (III). These findings agree with investigations on wire arrays which revealed that the crystals increase in size for depositions at higher temperature and lower overpotential (see Chapter III).

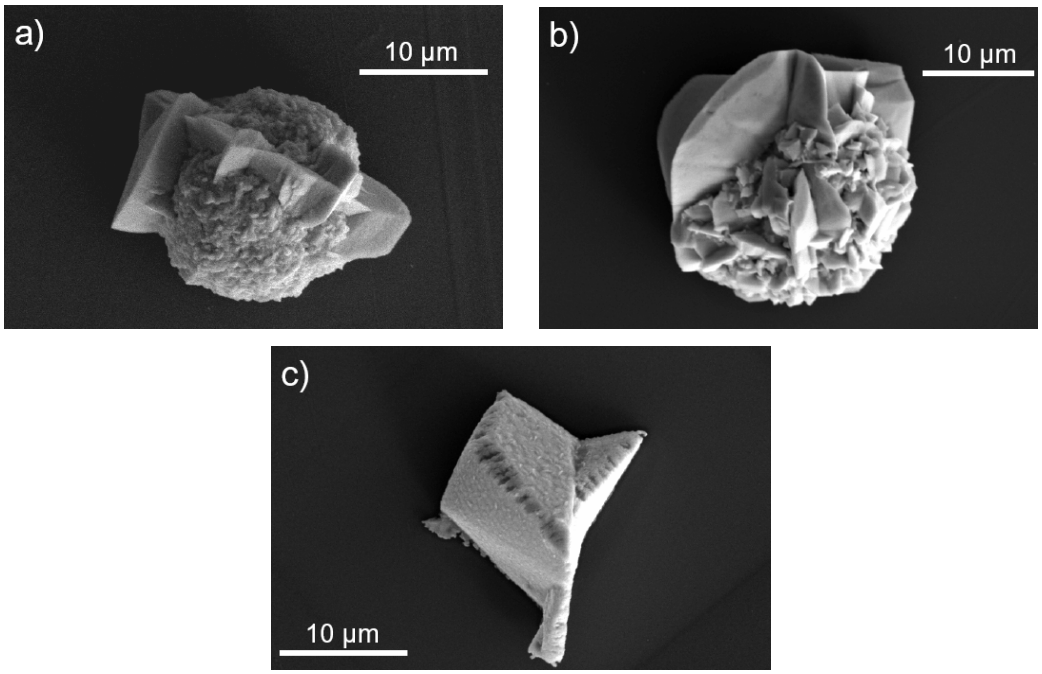

Figure 59: SEM micrographs of caps grown on top of single bismuth nanowires. a) *T* = 30 °C, *U* = -50 mV, *d* = 270 nm, b) *T* = 50 °C, *U* = -25 mV, *d* = 310 nm, c) *T* = 60 °C, *U* = -17 mV, *d* = 205 nm.

VI.3.a Wire resistance at room temperature

Fig. 60(a) displays the electrical resistance as a function of diameter of single Bi nanowires with diameters ranging from 100 nm to 1 µm. The wires have been fabricated under the three conditions mentioned before: (I) full squares, (II) open squares, and (III) full circles. The errors of *d* originate from the uncertainties of the determination of the pore diameter, i.e., the errors of the template thickness, the specific electrical conductivity of the 1M KCl solution, and the measured current. The solid curve represents the resistance for the

nanowires calculated by means of equation (26), using the specific electrical resistivity of bulk bismuth (ρ_{bulk} = 114 μΩ cm at 300 K). The dotted curve takes into account totally diffuse electron scattering from the wire surface. The resistance of all wires is significantly higher than both predictions, i.e., well above the solid and the dotted curves. Over the whole range of diameters, wires grown at 60 °C and -17 mV possess the lowest resistance, increasing for wires fabricated at 50 °C and -25 mV, and being the highest for wires deposited at 30 °C and -50 mV.

The specific electrical resistivity ρ ($\rho = 1/\sigma$) for each wire was calculated using equation (26). Both the ρ and ρ/ρ_{bulk} values as a function of d are displayed in Fig. 60(b). For each kind of wires, the corresponding mean resistivity $<\rho>$ was calculated. The $<\rho>$ values for wires of type (I), (II), and (III) are represented by the dashed, dash-dotted, and dash-double-dotted lines. The mean values were used for calculating the corresponding curves in part (a). $<\rho>$ amounts to 850, 440, and 315 μΩ cm for wires prepared under condition sets (I), (II), and (III). The corresponding ρ/ρ_{bulk} is about 7.5, 3.8, and 2.8. One can see that the scattering of the data around the respective $<\rho>$ is the largest for wires of type (I) and the smallest for type (III). Fig. 60(b) also shows $\rho(d)$ (dotted curve) for totally diffuse electron scattering from the wire surface ($\varepsilon = 0$). Obviously, this scatter mechanism alone accounts neither for the high specific electrical resistivities that the nanowires display nor for the difference of ρ for wires deposited under different conditions. To explain the data, electron scattering from inner grain boundaries has to be included. According to the Mayadas-Shatzkes model, a higher density of grain boundaries, i.e., smaller mean grain sizes D, causes an increase of ρ (see chapter V.I.b). As seen before, the mean grain size of crystals forming the wire caps increases for wires of type (I) to (III). Thus, electron scattering from grain boundaries is pronounced more strongly in wires created at lower temperature and higher overpotential. This correlation agrees qualitatively with the measurements of the electrical resistance.

The specific electrical resistivity of wires created at 30 °C and -50 mV decreases with diminishing wire diameter. This observation is ascribed to the fact that the texture for thinner wires is more pronounced. With reducing wire cross-section, the probability for simultaneous growth of different crystals become smaller, and thus the number of grain boundaries diminishes involving a lower specific electrical resistivity for wires of smaller diameter.

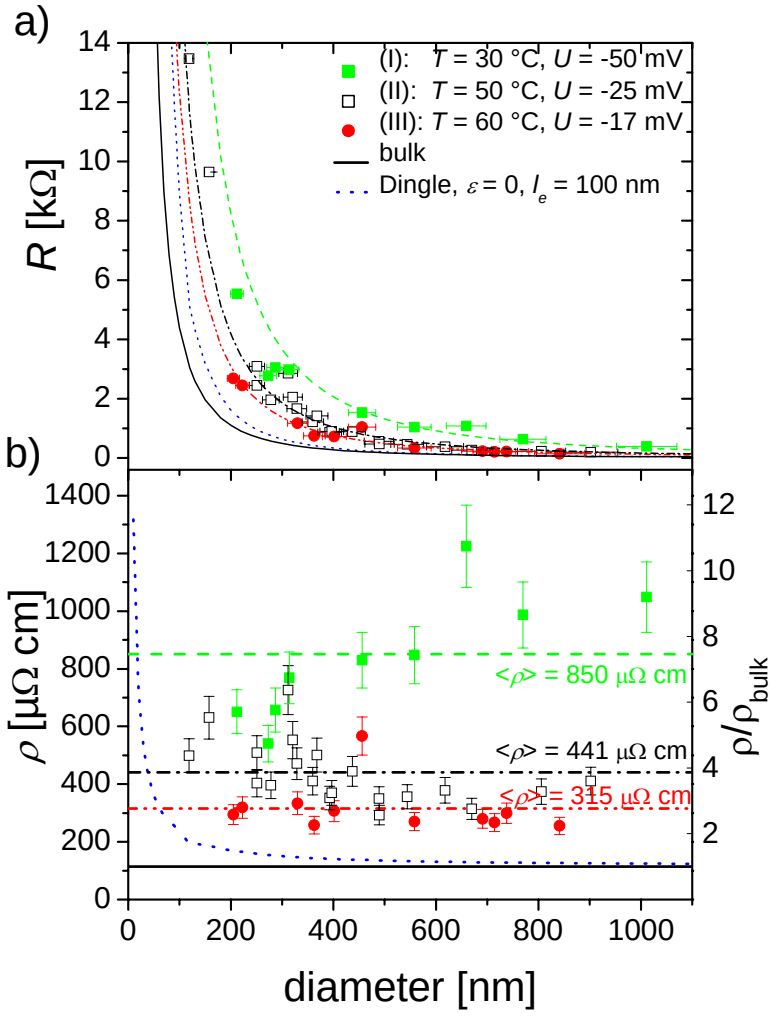

Figure 60: a) Electrical resistance *R* and b) specific electrical resistivity ρ as well as resistivity ratio ρ/ρ_{bulk} as a function of *d* of single bismuth nanowires fabricated under three different conditions, where *T* and *U* were: (I) 30 °C, -50 mV (■), (II) 50 °C, -25 mV (□), and (III) 60 °C, -17 mV (●). The solid line represents the classical behaviour while the dotted curve takes into account totally diffuse electron scattering from the wire surface. The other lines in part (b) represent the mean specific electrical resistivity <ρ> of the respective type of wires being used to calculate the corresponding curves in part (a): (I) dashed, (II) dash-dotted, and (III) dash-double-dotted.

Neglecting electron scattering from the wire surface ($d/l_e > 2$), the Mayadas-Shatzkes model provides α to be 4.5, 2.1, and 1.3 for the different types of wires (I), (II), and (III). The absolute grain size cannot be deduced from α because the grain boundary reflectivity is unknown. Assuming the same reflectivity for all wires, the relative grain size is 1 : 1.6 : 3.5 for the three kinds of wires. This means that the averaged grain size increases by a factor of more than three for single-crystalline wires compared to the wires consisting of the smallest grains.

In the case of $\mathscr{R}$ = 0.5, the grain sizes are about 22, 47, and 77 nm for the respective wire types (I), (II), and (III). These mean grain sizes are far below the mean distances of grain boundaries observed in nanowires of d < 100 nm by transmission electron microscopy. It can be concluded that either the mean grain size reduces with increasing wire diameter or the reflectivity of grain boundaries is higher than 50 %. Assuming a reflectivity of 90 %, the mean grain sizes amount to 210, 410, and 715 nm, i.e., they would be almost one order of magnitude larger compared to the case of $\mathscr{R}$ = 0.5. For instance, C. Durkan and M.E. Welland found reflectivities of 90 % in the case of polycrystalline, rectangular Au nanowires [101]. In contrast to such high reflectivities, $\mathscr{R}$ has been found to be about 0.5 in copper nanowires [102], being a factor of two higher than in bulk Cu ($\mathscr{R}$ = 0.24) [43].

In summary, single Bi wires with diameters ranging from 100 to 1000 nm were fabricated by employing three different deposition conditions and were subsequently electrically contacted. For each type of wire a discrete resistivity is found which increases for wires created at lower temperature and smaller overpotential. The increase of ρ is attributed to smaller mean grain sizes and thus a higher density of grain boundaries from which electrons are scattered. These findings are in qualitative agreement with the theoretical model of A.F. Mayadas and M. Shatzkes describing electron scattering at grain boundaries.

VI.3.b Electrical transport properties as a function of temperature

VI.3.b.i Electrical resistance

As shown in equation (27), the specific electrical conductivity is a function of carrier mobility as well as the carrier concentration, where both depend on T. When cooling down bulk bismuth from room temperature to 4 K, the charge carrier density decreases by a factor of about ten and, in addition, the mean free path increases from 100 nm to 400 µm [25], hence the carrier mobility rises by more than three orders of magnitude. In bulk Bi, the gain in mobility is more dominant than the effect of the reduction of the charge carrier concentration resulting in a monotonic decrease of the resistivity with diminishing T [96]:

$$\rho(T)\left[\mu\Omega\, cm\right] = 3.88 \cdot T\left[K\right] \qquad \textbf{(46)}$$

Fig. 61(a) presents the resistance as a function of temperature of single Bi nanowires that were fabricated at 60 °C and -17 mV, thus possessing large grains. For all diameters, the $R(T)$ curves are non-monotonic, displaying a maximal resistance R_{max} at a certain temperature T_{max}. R_{max} rises and T_{max} diminishes with increasing wire diameter.

$R(T)$ curves for nanowires grown at 30 °C and -50 mV, i.e. wires consisting of small grains, are shown in Fig. 61(b). The resistance is also a non-monotonic function of the temperature, and R_{max} and T_{max} possess the same dependence as in the case of single-crystalline wires. The curve corresponding to the wire with a diameter of 320 nm does not follow this tendency. Both R_{max} and T_{max} display the values expected for single-crystalline wires. Since the electrochemical deposition is performed without reference electrode, the real cathode overpotential could vary so that the crystal size of a certain wire may differ from the expected.

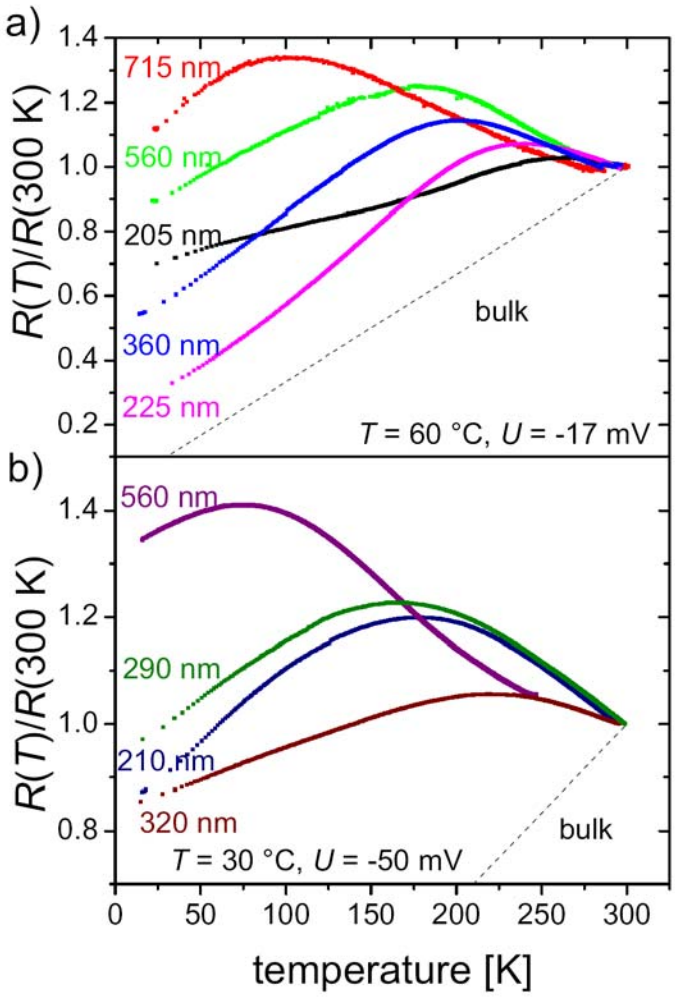

Figure 61: Electrical resistance as a function of *T* of single Bi nanowires with various *d* deposited a) at 60 °C and -17 mV (large grains) and b) at 30 °C and -50 mV (small grains). The dashed line corresponds to the electrical resistance of bulk bismuth.

Resistance versus temperature curves obtained on three single wires with similar diameter (210, 225, and 280 nm), but each of them possessing a different crystallinity, are presented in Fig. 62(a). In the three cases, the $R(T)$ behaviour is non-monotonic, and both R_{max} and T_{max} are a function of the wire crystallinity. The wire consisting of the smallest grains posseses the highest R_{max} occurring at the lowest T_{max}, while the wire constructed by the largest grains exhibits the lowest R_{max} which is present at the highest T_{max}. Hence, the data implies that T_{max} shifts to lower temperatures for nanostructures formed by grains of smaller size. The dependence of T_{max} on the wire diameter for the three different types of wire is summarized in Fig. 62(b). The data can be plotted linearly. However, more data points are necessary for a quantitative analysis of the slopes which amount to -0.32, -0.39, and -0.28 K/nm for the wires of types (I), (II), and (III).

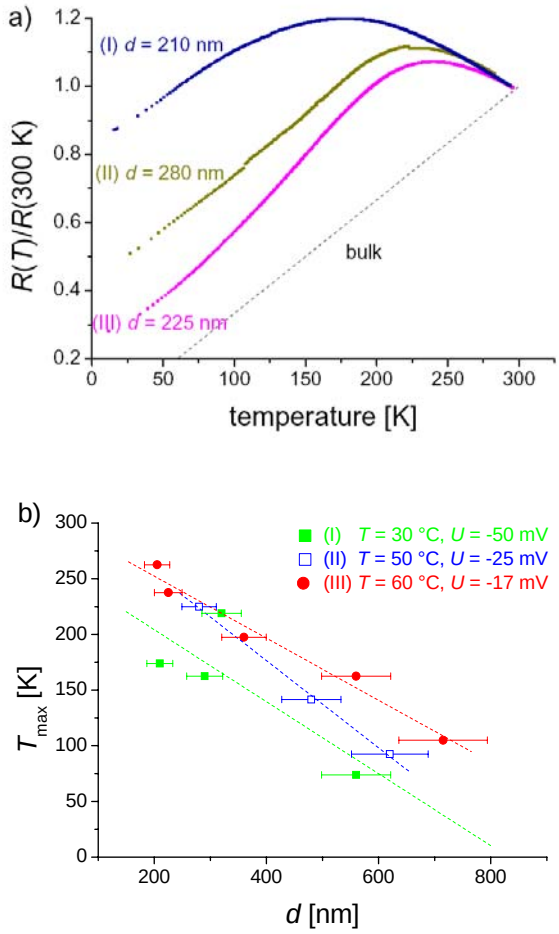

Figure 62: a) Electrical resistance as a function of T of single Bi nanowires with similar diameter grown under condition sets (I), (II), and (III). The dashed line corresponds to the electrical resistance of bulk bismuth. b) T_{max} as a function of d for the three different types of wires consisting of small (■), medium sized (□), and large grains (●). The dashed lines represent the corresponding best linear fits.

Figure 63 displays the specific electrical resistivity vs. temperature of single wires prepared under condition (III) with diameters ranging from 205 to 715 nm. The value of the specific resistivity maximum varies within ± 20 %.

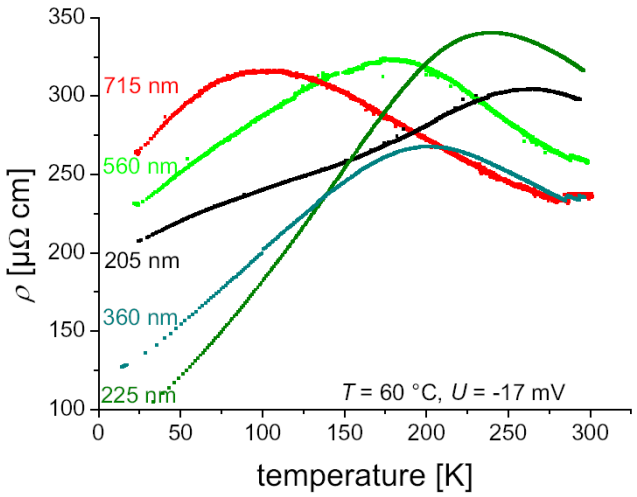

Figure 63: Specific electrical resistivity as a function of temperature of single bismuth nanowires consisting of large grains with various diameters.

A non-monotonic $R(T)$ behaviour has been previously measured on bulk samples of bismuth alloys [97, 103], on Bi nanowires [20, 71], and on Bi thin films [9, 46]. In the case of bulk bismuth alloys, the resistance maximum is a function of the amount of impurities. For instance, in the case of Bi-Pb and Bi-Sn bulk alloys, both the specific electrical resistivity increases and its maximum shifts to higher temperatures for larger impurity concentration. In the case of Bi-Sn alloys, the maximum shifts from ~ 170 K to ~ 280 K, and ρ increases simultaneously by a factor of two when the amount of Sn is raised from 0.04 to 0.2 % [104]. In the case of nanowires and thin films, the non-monotonic behaviour has been attributed to finite-size effects. In contrast to the non-monotonic behaviour, wires of diameter 200 nm to 2 μm showed a monotonic resistance increase for decreasing temperature, which the authors ascribed to the strong polycrystallinity of their wires [22]. From both the results obtained by Liu et al. [22] and the findings presented in this work, it is concluded that the maximum of the $R(T)$ curves shifts to lower temperatures with decreasing mean grain size. This leads to a negative temperature coefficient over the whole temperature range under investigation for wires consisting of sufficiently small grains. This interpretation is supported by measurements on poly- and single-crystalline Bi wires of diameter 70 nm which exhibited a monotonic and non-monotonic $R(T)$ behaviour, respectively [20].

VI.3.b.ii Carrier mobility

The carrier mobility for nanowires as a function of the temperature is derived by using equation (27). The temperature dependence of the charge carrier density is taken into account under three hypotheses: (i) the charge carrier densities for electrons n and holes p are equal, and (ii) $n(T)$ is the same for wires with $d \geq 200$ nm as for bulk bismuth. (iii) The electron and the hole mobilities differ very little from each other, and this difference does not change with the temperature [46]. The data for bulk Bi was taken from ref. [12] leading to the following equation

$$\frac{n(T)}{n(300\ \mathrm{K})} = 0.15 \cdot \exp\left(\frac{T}{158}\right) - 0.057 \qquad \textbf{(47)}$$

where $n(300\ \mathrm{K}) = 3*10^{18}\ \mathrm{cm}^{-3}$ and the temperature is given in Kelvin.

Figures 64(a), (b), and (c) display the charge carrier mobility of different types of bismuth nanowires as a function of temperature. At room temperature the mobility for nanowires amounts to 0.1 to 0.5 $\mathrm{m}^2/(\mathrm{Vs})$, being a factor of two to ten smaller than for bulk Bi. It mainly depends on the wire crystallinity. The mobility increases with diminishing T. The rise is smaller for nanowires than for bulk bismuth. The carrier mobility for wires consisting of medium-sized and large grains shows a cross-over at about 200 K. For $T > 200$ K the mobility slightly increases with increasing diameter, whereas for $T < 200$ K it decreases for larger d. For wires consisting of small grains, the mobility is larger in thinner wires over the whole temperature range under investigation. At few ten Kelvin the mobility saturates for all nanowires as was found in previous works for both Bi thin films [45, 105] and nanowire arrays [21]. The saturation value of μ is a function of both the wire diameter and crystallinity. At 20 K the mobility for nanowires is one to two orders of magnitude smaller than for bulk Bi. The mobility is higher for wires that consist of larger grains. In the case of wires of the same type, μ is the higher the smaller the diameter is.

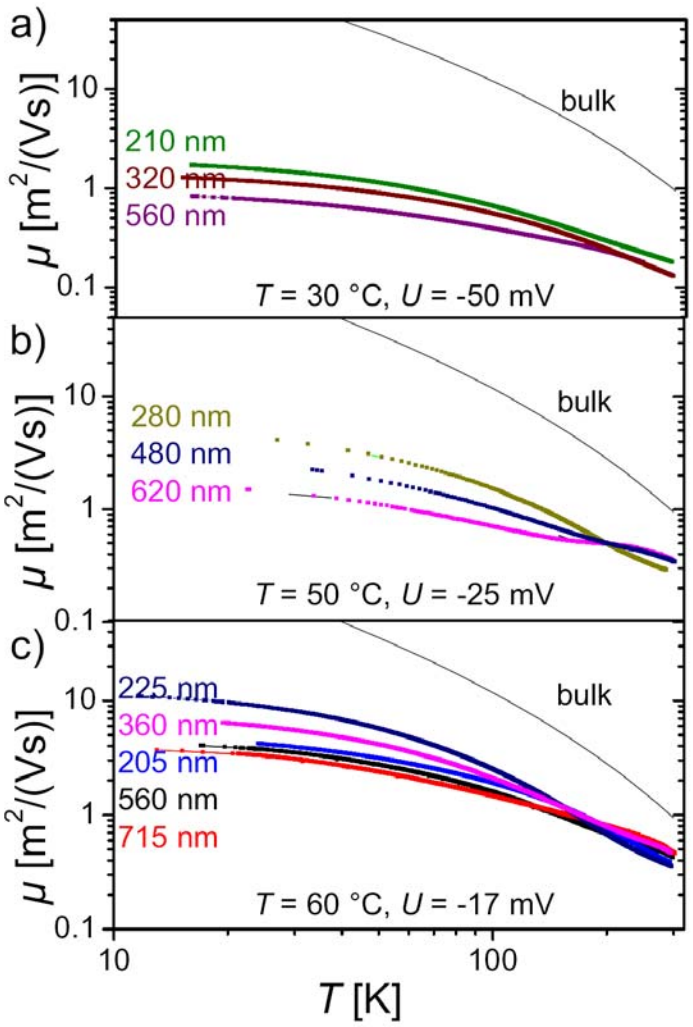

Figure 64: Mobility of charge carriers as a function of temperature for bismuth nanowires consisting of grains of different size: a) small, b) medium sized, and c) large grains. The solid line corresponds to the carrier mobility in bulk Bi.

By means of Matthiessen's rule, the total wire mobility is derived by summing up the inverse of several contributions [20]

$$\mu^{-1} = \sum_i \mu_i^{-1}$$
$$\mu_{wire}^{-1} = \mu_{phonon}^{-1} + \mu_{imp}^{-1} + \mu_{defect}^{-1} + \mu_{boundary}^{-1} \quad \textbf{(48)}$$

where μ_{phonon}, μ_{imp}, μ_{defects}, and μ_{boundary} represent electron-phonon coupling, and the influence of electron scattering from charged impurities, from neutral defects, and from boundaries, respectively. Electron scattering from neutral defects and boundaries is assumed

to be independent of T. The temperature dependence of the respective mobilities is the following [20, 106] with N_I being the density of charged impurities.

$$\mu_{phonon} \sim (m^*)^{-5/2} T^{-3/2} \quad \textbf{(49a)}$$

$$\mu_{imp} \sim (m^*)^{-1/2} N_I^{-1} T^{3/2} \quad \textbf{(49b)}$$

In bulk Bi, electron-phonon coupling determines the charge carrier mobility. This implies that the lower mobility, observed for nanowires compared to bulk material, originates from additional scattering processes at impurities, defects, and/or boundaries. For Bi thin films, the saturation of μ was ascribed to finite-size effects [105]. Further, in previous experiments it has been shown that the electron scattering at the surface of metallic wires (e.g. Cu, Ag) is diffuse [107], while in the case of bismuth it is specular [108, 109]. This may be explained by the fact that the electron wavelength in metals is of the order of the atomic spacing, and hence surface roughness on the atomic scale involves diffuse scattering, whereas such surface irregularities cannot be resolved by charge carriers in Bi due to their long λ_F leading to specular reflection. Thus, in conclusion, the limitation of the mobility is mainly ascribed to electron scattering at grain boundaries.

As already mentioned before, one can observe at low temperatures that the mobility is the higher, the smaller the diameter is for nanowires of similar crystallinity. This increased μ may be attributed to the grain size. For given deposition conditions, there may be only one crystal growing in the cross-section of a wire with sufficiently small diameter, while for thicker wires several grains may be present in the wire cross-section. Therefore, for wires of smaller d, less scattering at grain boundaries occurs. This explanation is in agreement with our results obtained by x-ray diffraction, showing a texture increase for decreasing d (see Chapter III) [68].

Likewise, higher mobilities for wires of smaller diameter may originate from scattering from charged impurities whose density decreases with decreasing d. But, one has to keep in mind that charged impurities would also affect the charge carrier density n in the wires. The increase of the mobility observed for smaller diameters could also be an artifact originating from taking into account for the calculations a too small charge carrier density. In order to increase n in wires of smaller diameter, a larger density of impurities would be necessary. However, an increased N_I would result in a reduction of μ due to electron scattering. Depending on both the carrier effective mass and the density of impurities one of the effects

may dominate. Additional charge carriers may also originate from surface defects that increase the total charge carrier density with decreasing wire diameter [46], fitting qualitatively to the observed mobility behaviour at 20 K as a function of d. This consideration should also be valid for room temperature. Contrariwise, for wires of type (II) and (III) a reducing mobility with decreasing diameter is observed. Hence, surface charge states are no appropriate explanation for the observed $\mu(T)$ behaviour.

In Fig. 65, the resistivity ratio between wires and bulk Bi ρ_{wire}/ρ_{bulk} corresponding to μ_{bulk}/μ_{wire} is presented as a function of the inverse temperature. The resistivity ratio can be well described by a T^{-1}-law for $T \leq 100$ K independent of both the wire diameter and crystallinity. The slope becomes the less, the smaller the diameter and the larger the mean grain size.

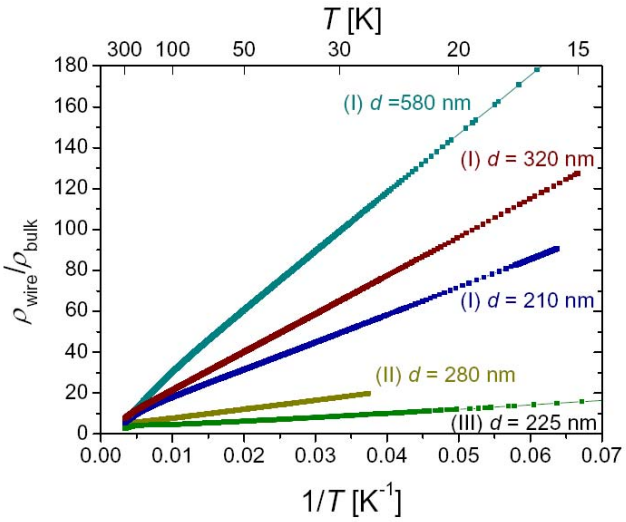

Figure 65: Resitivity ratio ρ_{wire}/ρ_{bulk} as a function of T^{-1} for bismuth nanowires of different crystallinities and diameters. ρ_{wire}/ρ_{bulk} corresponds to the mobility ratio μ_{bulk}/μ_{wire}.

In general, mobilities can be well described by $T^{-\alpha}$ laws, where the temperature coefficient for bulk Bi amounts to $\alpha_{bulk} = 2.5$ [92]. These proportionalities lead to a temperature scaling of the resistivity ratio that is given in equation (50):

$$\frac{\rho_{wire}}{\rho_{bulk}} = \frac{\mu_{bulk}}{\mu_{wire}} = \frac{T^{-\alpha_{bulk}}}{T^{-\alpha_{wire}}} = T^{-\alpha_{bulk}+\alpha_{wire}} \qquad \textbf{(50)}$$

The ratio ρ_{wire}/ρ_{bulk} that sclaes with T^{-1} implies that $\alpha_{wire} = \alpha_{bulk} - 1 = 1.5$. Thus the carrier mobility for nanowires scales with $\mu_{wire} \sim T^{-3/2}$. For thin films the mobility was found be proportional to T^{-1}, at least for temperatures above the Debye temperature, and that α increases with rising temperature [92].

In equation (51), the mobility ratio is presented as a function of the carrier effective mass and of temperature, where A, B, and C are pre-factors. The formula was determined using $\mu_{bulk} \sim T^{-5/2}$ and the temperature dependences of the different mobilities given in equations (49a) and (49b).

$$\begin{aligned}\frac{\mu_{bulk}}{\mu_{wire}} &= 1 + \frac{\mu_{bulk}}{\mu_{imp}} + \frac{\mu_{bulk}}{\mu_{defect}} + \frac{\mu_{bulk}}{\mu_{boundary}} \\ &= 1 + A(m^*)^{-1/2} N_I T^{-4} + (B + C) T^{-5/2}\end{aligned} \tag{51}$$

In order to obtain $\mu_{bulk}/\mu_{wire} \sim T^{-1}$ at low temperatures, either the electron effective mass has to be strongly affected by the temperature or scattering from boundaries has to be a function of T, depending on which effect dominates. However, the band structure of bismuth is expected to remain almost unchanged for $T < 80$ K [110] and hence, the electron effective mass should be nearly constant. Since the influence of the scattering processes on the resistivity depends on the electron mean free path which is affected by the temperature, the effect itself should be a function of T in contrast to the presumptions at the beginning. The increased slope of μ_{bulk}/μ_{wire} for wires containing larger grains and for wires of the same type possessing smaller d may be ascribed to a higher number of both the defects and grain boundaries. This would also explain the increased mobility observed for diminishing diameters for wires of the same type.

In conclusion, measurements of the electrical resistance as a function of the temperature on single bismuth nanowires reveal a non-monotonic $R(T)$ behaviour that originates from a limited increase of the charge carrier mobility caused by finite-size effects. The mobility is the higher the larger the grains are because of the lower density of the grain boundaries, i.e. less electron scattering from grain boundaries. In addition, wires of the same type show an increased carrier mobility for smaller diameters because of less grain boundaries from which electrons are scattered. Further, the resistivity ratio ρ_{wire}/ρ_{bulk} scales with T^{-1} for temperatures below 100 K. The different scalings above and below 100 K may be ascribed to a temperature dependence either of the carrier effective mass or to scattering from defects and boundaries.

Chapter VII

MAGNETORESISTANCE

VII.1 Influence of magnetic fields

In a magnetic field charged particles, such as the charge carriers in our Bi wires, experience the Lorentz force. The cylindrical wire axis be oriented along the z-axis. For magnetic fields oriented along the *z*-axis, i.e., ($\vec{H} \parallel \vec{E}$), the Lorentz force $\vec{F}$ splits up into two independent components, namley eE_z along the z-axis and $e \cdot \left(v \times H_z / c \right)$ which is always perpendicular to the z-axis.

$$\vec{F} = e \cdot \left(\vec{E} + \frac{1}{c} \left(\vec{v} \times \vec{H} \right) \right) \qquad \textbf{(52)}$$

e is the elementary charge, *c* the velocity of light, and *v* the velocity of the particle.

If the velocity of the electrons at the Fermi surface is v_F and the magnetic field is applied along the *z*-axis, electrons travelling at an angle θ to the *z*-axis will move on helical paths where the projections on the *x*-*y*-plane are circles of radius

$$r = r_0 \sin\theta = \frac{m^* v_F c}{eH} \sin\theta \qquad \textbf{(53)}$$

here, m^* is the carrier effective mass and $r_0 = m^* v_F c/(eH)$, i.e. r_0 the radius of the circle for $\theta = 90°$.

A magnetic field induces a higher resistance, the so-called magnetoresistance (MR). The fundamental quantity for MR is $\omega_c \tau$ where τ is the mean scattering time, i.e., the mean time between two scattering events, and ω_c is the cyclotron frequency.

$$\omega_c = \frac{eB}{m^*} \tag{54}$$

Strong magnetoresistances are obtained when the electrons complete a full helix turn before they are scattered. In contrast to conventional metals, $\omega_c \tau$ in bismuth is rather large because the mean scattering time is long and the cyclotron mass is small, resulting in a pronounced magneotresistance. At lower temperatures, τ increases and thus $\omega_c \tau$ rises. Hence, the magneotresistance becomes more pronounced at lower T.

Several decades ago, R.G. Chambers [111] developed a theory in order to treat the behaviour of the electric resistance of thin wires in a magnetic field. At low fields with $r_c > d/2$, more carriers scatter from the wire walls than without magnetic field, involving a resistance increase. As the field increases to a critical field strength where $r_c < d/2$, scattering from the wall is decreased. Thus, the resistance diminishes because the mobility increases. The maximum magnetoresistance should very roughly occur at a magnetic field where

$$r_c = \frac{d}{2} = \frac{p_F}{eH} = \frac{\hbar k_F}{eH} \tag{55}$$

with p_F and k_F being the Fermi momentum and Fermi wavevector of the charge carriers.

The value of r_c and thus the effect of the magnetic field is independent of whether $\vec{H}$ is parallel or anti-parallel to the electrical current. According to R.G. Chambers, the conductivity of a thin wire in a longitudinal magnetic field is given by the following equation

$$\frac{\sigma}{\sigma_0} = 1 - \frac{4}{3\pi s} \int_s ds \int_0^{2\pi} d\phi \int_0^{2\pi} d\theta \cos^2\theta \sin\theta \exp\left(-\psi \frac{r_0}{l_e}\right) \tag{56}$$

where θ is the angle between the direction of the carrier motion and the z-axis, ϕ the azimuthal angle around the z-axis, s the cross-sectional area of the conductor, ψ the angle traversed by the charge carrier, and l_e the mean free path.

Explicit solutions of the upper formula are only possible for large fields. For magnetic fields where $d \geq 10r_0$ the specific electrical conductivity of a thin wire can be expressed by equation (57) where d is the wire diameter.

$$\frac{\sigma}{\sigma_0} = 1 - \frac{3}{4\frac{d}{l_e}\left(1+\frac{1}{4}\left(\frac{l_e}{r_0}\right)^2\right)}\left[1+\frac{1}{8}\left(\frac{l_e}{r_0}\right)^2\left(1-\exp\left(-2\pi\frac{r_0}{l_e}\right)\right)\right] \qquad \textbf{(57)}$$

Unfortunately, for the most interesting regime, $d \sim r_0$, R.G. Chambers could not obtain a simple and valid formula.

Figure 66 shows ρ/ρ_0 plotted against $d/(2r_0) = (edH)/(2m^*v_Fc)$, where the values have been taken from Chambers' work [111]. For large magnetic fields, ρ/ρ_0 becomes dependent only on $d/(2r_0)$, i.e., independent of the electron mean free path. According to the calculations by Chambers, longitudinal magnetoresistance is less important for wires of diameter equal to or larger than the electron mean free path. In the case of wires of diameters less than l_e, the wire resistivity becomes strongly affected by the magnetic field.

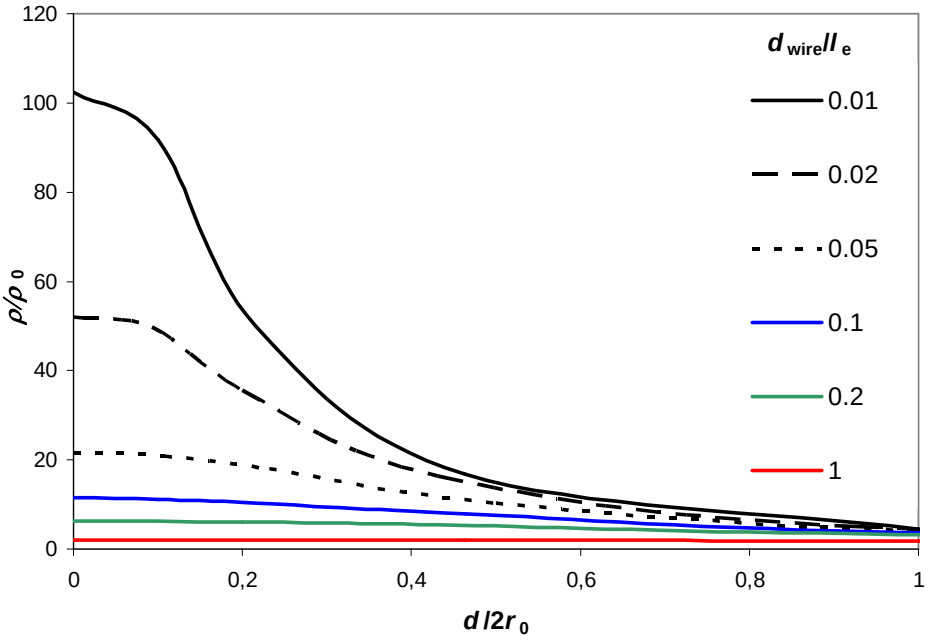

Figure 66: Resistivity ratio of longitudinal magnetoresistance as a function of both $d/(2r_0)$ and d/l_e.

While for $\vec{H} \parallel \vec{E}$ the magnetoresistance is expected to decrease for sufficiently high magnetic fields, in transverse arrangement, i.e., $\vec{H} \perp \vec{E}$, the magnetoresistance is expected to increase monotonically with the magnetic field. For ideal semimetals the transverse magnetoresistance scales with H^2 as long as $\omega_c \tau << 1$. Because of the long mean free path and very small electron effective mass, the condition $\omega_c \tau << 1$ breaks down in bulk Bi at rather weak magnetic fields. At 4 K, a deviation from the quadratic behaviour was found in bulk Bi at 4 Oe, while for Bi thin films this scaling was valid up to 1 kOe at T = 12 K [9, 112]. The higher magnetic field at which the H^2-scaling breaks down for thin films was attributed to a reduced mean free path that was mainly caused by crystal imperfections.

Besides the classical effetcs discussed above, the surfaces on which electrons in solid state materials travel in ***k***-space are quantized in magnetic fields. The electrons travel on so-called Landau tubes which are schematically depicted in Fig. 67 [9].

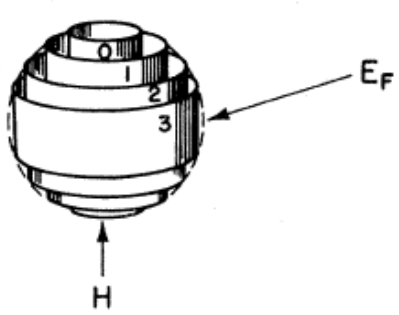

Figure 67: Schematic of the quantization of the Fermi sphere to Landau tubes in a magnetic field (taken from ref. [9]).

When increasing the magnetic field strength, the Landau tubes are inflated. The inflation involves that one Landau tube after another crosses the Fermi level. Since above E_F any state may be occupied at low temperatures, Landau levels that cross the Fermi level are emptied. Hence, by amplifying B the quantum number of the highest occupied states decreases by one at certain values of the magnetic field strength. The transport of electrons to lower levels is permitted because their degeneration grows with increasing magnetic field. At such moments, the mean free energy of the system is smaller than in the case when the Landau tube traverses the Fermi level. At sufficiently low temperatures and for a sharp Fermi edge, the system exhibits its smallest mean free energy just when a Landau level crosses E_F. With increasing magnetic field the free energy grows until the next Landau level is depleted.

Hence the mean free energy oscillates as a function of B [77]. By measuring the period of ΔB the cross-section of the Fermi surface S_F can be directly obtained.

$$\Delta B = \frac{2\pi e}{\hbar S_F} B^2 \Leftrightarrow \Delta\left(\frac{1}{B}\right) = \frac{2\pi e}{\hbar S_F} \quad \textbf{(58)}$$

The electrical conductivity originates from adding infinitesimally small energy portions to electrons in an electric field and additional scattering by both phonons and impurities. These scatter processes cause an energy broadening of the Landau states so that the electrons may receive supplementary energy from the outer field. When such a broadened Landau state crosses the Fermi level, it is depleted, and thus the conductivity decreases, i.e., oscillations of the electron density in the vicinity of E_F become directly observable in the electrical conductivity of the system. These oscillations are known as “Shubnikov-de Haas effect”. Since the density of states (DOS) vanishes between two Landau levels, the conductivity becomes infinitesimally small in the case of a magnetic field range, in which both Landau levels are sufficiently far below and above the Fermi energy. The conductivity shows a sharp band when the density of states traverses E_F. At sufficiently low temperatures, this sharp band corresponds to the broadened DOS [77].

VII.2 Experimental setup at the EPFL

Very first experiments in magnetic fields up to 9 kOe on bismuth nanowire arrays at different temperatures were performed at the Ecole Polytéchnique Fédérale de Lausanne (EPFL) in collaboration with Dr. habil. Laurent Gravier. For this purpose, nanowire arrays with an area density of 10^7 to 10^8 cm^{-2} were deposited employing two different conditions, namely (i) 60 °C and -17 mV and (ii) 30 °C and -50 mV. The depositions were continued until caps were formed on top of the wires. In order to minimise the number of electrically contacted wires, only an area of 1 mm^2 is covered by gold. The sample, i.e., the wires embedded in the polycarbonate membrane, is glued on a copper electrode of a printed circuit board using silver conducting paste. Subsequently, a gold strip is fixed on the gold surface on top of the sample, connecting the upper Au electrode to a second copper lead on the circuit (see Fig. 68(a) and (b)).

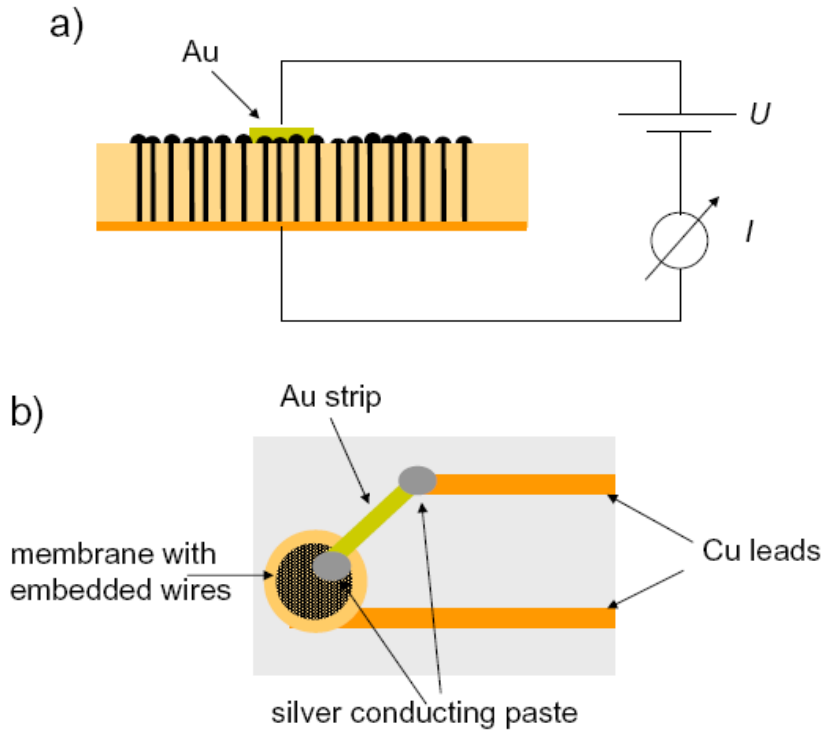

Figure 68: Schematics of a) the electrical contacting method used at the EPFL and b) top view of the printed circuit board on which the sample is placed for electrical contact.

In order to perform experiments at various temperatures and magnetic fields, the sample is mounted in a cold head cryostat which can be cooled down to 15 K. The cryostat is equipped with magnetic coils that provide magnetic fields up to 10 kOe at a current of 60 A (Fig. 69). The power supply provides a stable current and hence a stable magnetic field. The magnetic field strength is measured outside of the cryostat by means of a Hall probe. The magnetic field strength at the sample is calculated by multiplying the measured field strength with a correction factor.

Experiments as a function of the magnetic field were performed by sweeping the magnetic field strength from minus to plus 10 kOe and back. $R(H)$ curves are recorded for two distinct orientations of the magnetic field with respect to the wire axis - normal and parallel to the longitudinal cylinder axis of the wires.

Figure 69: Photograph of the cryostat with attached magnetic coils used for magnetoresistance measurements as a function of *T* at the EPFL in Lausanne.

VII.3 Magnetoresistance of bismuth nanowire arrays

The longitudinal and transverse magnetoresistances (LMR and TMR), i.e., [$R(H)$ - $R(0)$]/$R(0)$, of nanowires with diameter 200 nm at 20 K as well as at room temperature are displayed in Fig. 70. The wires were deposited at 60 °C and -17 mV and, thus, consisted of large grains. All magnetoresistance curves are symmetric with respect to change of sign of the magnetic field. Further, the magnetoresistances increase with rising magnetic field where TMR increases stronger than LMR. While the former decreases with increasing temperature, the latter is almost unaffectd by the change in T.

The symmetry of the longitudinal magnetoresistance with respect to $H = 0$ implies that LMR is not influenced by the sign of H, i.e., whether H is parallel or anti-parallel to the electrical current. In the transverse geometry all carriers are in cyclotron motion and, thus, contribute to the magnetoresistance. In contrast, for LMR only a small fraction of the carriers contributes to the MR because H is along the electrical current [113]. This leads to a more pronounced transverse than longitudinal magnetoresistance. The increasing TMR at lower temperature is ascribed to the fact that the mean scattering time rises for smaller T, involving an increase of the fundamental quantity $\omega_c\tau$. However, this argument does not hold for LMR.

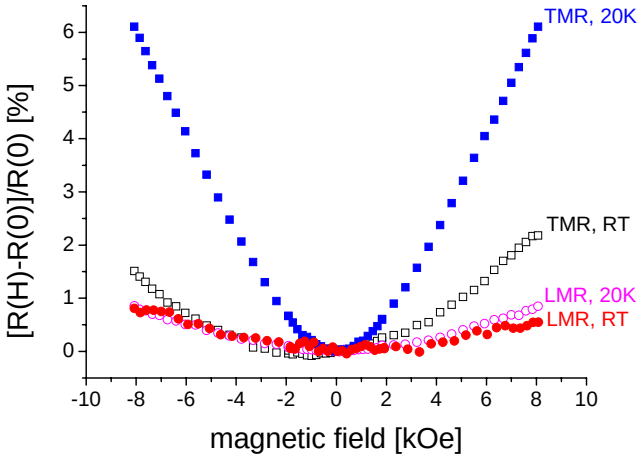

Figure 70: Transversal and longitudinal magnetoresistance at room temperature and at 20 K of bismuth nanowires of diameter 200 nm deposited at 60 °C and -17 mV.

Longitudinal and transverse magnetoresistance at 20 K of nanowires of various diameters and grain sizes are presented in Figs. 71(a) and (b), respectively. For all wires holds TMR > LMR, independent of wire diameter and grain size. Both magnetoresistances rise with

increasing wire diameter. TMR becomes stronger pronounced for wires consisting of bigger grains, whereas in the case of LMR no difference on the grain size is observed for wires of d = 200 nm.

Because of additional scattering processes from the wire surface, τ is reduced for wires of smaller diameter and, thus, MR decreases. The fact that the longitudinal magnetoresistance for wires of diameter 200 nm is independent of the mean grain size implies that the effect of electron scattering from the wire surface on the magnetoresistance surpasses the influence of grain boundaries. Because the charge carriers are forced to helical paths, they are scattered from the wire surface before they experience a scattering process from a grain boundary. According to R.G. Chambers, LMR should diminish when the radius of the electron helices becomes smaller than the wire radius. Such a decrease is not observed for the wires under investigation, i.e., the radius of the electron helices are probably larger than 200 nm for $H \leq 9$ kOe.

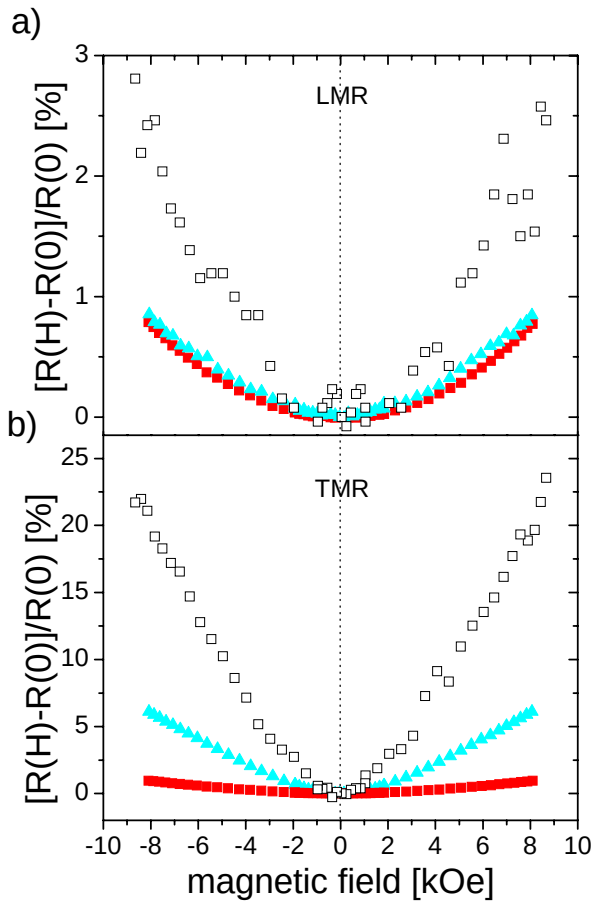

Figure 71: a) Longitudinal and b) transverse magnetoresistance as a function of the magnetic field at 20 K of Bi nanowires of various diameters and consisting of different grain sizes: (□) T = 60 °C, U = -17 mV (large grains), d = 440 nm, (▲) T = 60 °C, U = -17 mV (large grains), d = 200 nm, (■) T = 30 °C, U = -50 mV (small grains), d = 200 nm

The transverse magnetoresistance at 20 K as a function of H^2 is presented in Fig. 72. Part (a) displays TMR over the whole measurement range while part (b) focuses on magnetic fields up to 3 kOe. TMR deviates from a direct proportionality to H^2 that is indicated by the dashed lines in Fig. 72(b). The deviation from this behaviour is a function of wire diameter as well as mean grain size. For wires of d = 440 nm, the H^2-scaling breaks down already at magnetic fields of less than 2 kOe, whereas this behaviour is valid to higher magnetic fields for wires of smaller diameter. Further, the breakdown of this scaling occurs at higher magnetic fields for wires of similar diameter but consisting of smaller grains. It appears at ~ 2.5 and ~ 3 kOe for wires with diameter 200 nm consisting of large and small grains, respectively.

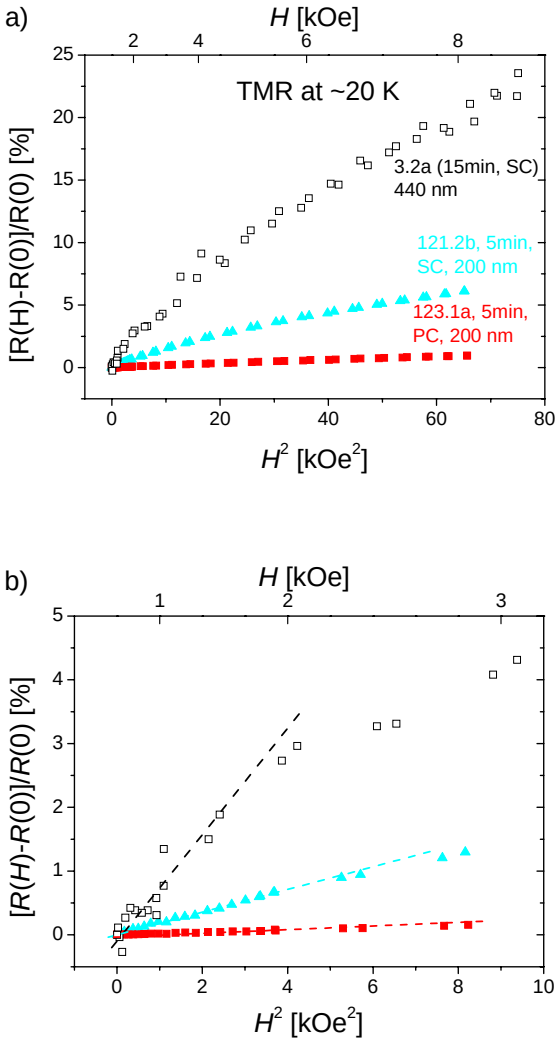

Figure 72: Transverse magnetoresistance as a function of H^2 at 20 K of bismuth nanowires of various diameters and crystallinity: (□) T = 60 °C, U = -17 mV, d = 440 nm, (▲) T = 60 °C, U = -17 mV, d = 200 nm, (■) T = 30 °C, U = -50 mV, d = 200 nm

As mentioned before, the breakdown of the H^2-scaling occurs for ideal semimetals when $\omega_c\tau$ becomes larger than unity, i.e. the charge carriers may complete a full turn before they are scattered. As the cyclotron frequency is not a function of wire diameter and grain size, the findings indicate that the mean scattering time is longer for both wires of larger diameter and wires consisting of larger grains. The larger τ for these wires originates from less scattering from the wire surface and from grain boundaries.

Measurements of the electrical resistance as a function of the magnetic field show magneotresistances that grow with increasing wire diameter and decreasing temperature. Since MR is the more pronounced the larger $\omega_c\tau$ is, both observations are explained by an increasing electron mean free path. For all temperatures and wire diameters, TMR > LMR. In addition, at low magnetic fields TMR scales with H^2. The breaking down of the proportionality occurs at the weaker fields the larger the wire diameter is and the larger the mean grain size is because of less electron scattering.

SUMMARY AND OUTLOOK

Nanostructures attracted an enormous interest in the recent past due to both the proceeding miniturization and investigation of new physcial phenomena. In particular, bismuth nanowires were investigated because of the material's unique electronic properties - large electron mean free path, long Fermi wavelength, small electron effective mass, and high thermopower.

In the present work, bismuth nanowires are deposited electrochemically in ion track-etched polymer membranes. These templates allow the variation of the area density of nanopores from a single pore up to 10^9 pores per cm^2. The influence of the deposition conditions on both the morphology and crystallinity of bismuth nanowires is investigated. Potentiostatically grown wires exhibit a <110> texture. The preferential orientation increases with diminishing overpotential, higher temperature, and smaller wire diameter. These findings are attributed to a higher mobility of the ad-atoms at lower overpotentials and elevated temperatures. Depending on the mobility, the ad-atoms may either build up already existing crystals or act as starting nucleii for a new grain. Higher mobilities lead to a more pronounced texture. Further, it is found that for larger pore diameters the deposition current density increases, involving a smaller ad-atom mobility and, thus, a less distinct wire texture. Wires fabricated by applying reverse pulses exhibit a <100> texture which becomes more pronounced for shorter pulses and higher anodic potentials. The XRD results are confirmed by TEM, showing single-crystalline wires with grains of several micrometers in length oriented along the <110> axis. The morphology of the caps grown on top of the wires is a strong indication for the wire crystallinity.

Infrared spectroscopy on single Bi nanowires performed at the electron synchrotron of ANKA reveal an absorption whose onset is blueshifted with diminishing wire diameter. The blueshift is explained either by a shift of energy bands caused by quantum-size effects or by surface defects that act as dopants involving an increase of the plasma frequency. Spectroscopy in the far-infrared (FIR) regime is expected to shed more light on these effects.

The plasma frequency of pure bulk Bi is located in this energy range and amounts to ~ 41 meV. In case that it will be detected for nanowires by FIR spectroscopy, the absorption observed in this work originates from quantum-size effects. In that case, measurements in the far-infrared regime may visualize the development of the subband splitting. In addition, the influence of the temperature on the absorption should be investigated because charge carriers originating from dopants or surface defects are independent of T, in contrast to the intrinsic charge carrier density of bismuth. Thus, IR spectroscopy as a function of temperature will help to clarify the origin of the observed absorption.

Electron energy loss spectroscopy determines the bulk and surface plasmon frequencies at ~ 15 and ~ 11 eV, respectively. For wires with diameter few ten nanometers no significant contribution of the surface plasmon to the electron energy loss is found. Further, no blueshift or broadening of the volume resonance is observed for wires with diameter 30 nm. Such effects are expected for specimen sizes of less than 10 nm.

Electrical transport properties of nanoobjects whose size is comparable to the electron mean free path are affected by finite-size effects – electron scattering from both the surface and grain boundaries. The influence of these effects on the electrical resistance of bismuth nanowires is investigated. For this purpose, single wires of diameters ranging from 100 to 1000 nm are fabricated and subsequently electrically contacted while they are left embedded in the template. Leaving the wires embedded avoids both their oxidation and possible chemical reactions with a template solvent. The electrical resistivity is a function of the wire crystallinity. It rises with increasing grain boundary density, i.e., smaller mean grain size, because of additional electron scattering processes. Examination of the electrical resistance as a function of temperature provides a non-monotonic $R(T)$ behaviour caused by finite-size effects. In bismuth the charge carrier density reduces, while the mobility rises with lowering temperature. In bulk Bi, the gain in mobility surpasses the decrease in charge carrier density, whereas the mobility for nanowires is limited by electron scattering processes from both the wire surface and grain boundaries. The combination of reducing carrier concentration and limited increase of the mobility leads to the observed non-monotonic $R(T)$ behaviour. The highest carrier mobilities were obtained for nanowires fabricated at 60 °C and -17 mV. The mobility at 20 K is one to two orders of magnitude smaller than in bulk material.

First measurements of resistance vs. magnetic field on wire arrays yielded the result that the magnetoresistance becomes more pronounced for larger wire diameters and lower temperatures. The fundamental ratio of MR is given by the product of the cyclotron frequency and the electron mean scattering time. Thus, the rise of the magnetoresistance is attributed to

an increasing mean free path. At low magnetic fields the transverse magnetoresistance scales with H^2. The break down of the proportionality is a function of wire diameter and grain size. The field at which the break down occurs is the weaker, the larger the wire diameter and the mean grain size are, the reason being less electron scattering. Further measurements of the magnetoresistance should be performed, covering a bigger variety of wire diameters as well as grain sizes. Besides the variation of the wire properties, such investigations should include a larger range of the magnetic field strength. In addition, in longitudinal alignment Shubnikov-de-Haas oscillations should become observable at sufficiently high magnetic field strengths. This effect allows the study of the structure of the Fermi surface. Further, magnetoresistance measurements should be performed on single wires in order to obtain absolute values of the electrical transport properties.

Likewise, future work should concentrate on thermal transport and thermopower (Seebeck coefficient) of nanowires consisting of pure bismuth and also of bismuth alloys - especially Bi_2Te_3. Today, the best thermoelectric devices are based on bismuth telluride which exhibits a figure of merit of about unity at room temperature. An enhanced figure of merit has been predicted for bismuth nanowires due to quantum confinement and additional doping, the latter being the case for Bi_2Te_3.

Since thermal stability of nanowires is indispensable for future devices, the behaviour of wires at elevated temperatures should also be examined. For instance, metallic nanowires (Cu, Au) of diameter few ten nanometers fragment at temperatures of some hundred degrees Kelvin below the melting temperature of bulk material.

ACKNOWLEDGEMENT

At this point I would like to thank all people who contributed to the success of this work:

- Prof. Dr. R. Neumann for giving me the opportunity to perform the doctoral work in the Materials Research Department at GSI and for his supervision of my doctoral work. Additionally, for the possibility to attend several interesting international workshops, conferences, and summer schools.
- Prof. Dr. A. Pucci from the Kirchhoff-Institut für Physik of Heidelberg University for acting as a referee for this dissertation.
- Dr. M.E. Toimil-Molares for all her help and support during the doctoral work as well as for reading and correcting this and many other manuscripts.
- Dr. C. Trautmann for introducing me into the ion irradiation at the Materials Research irradiation site X0 and for explaining the ion-matter interaction.
- Dr. N. Chtanko for giving support especially in questions related to the etching of latent tracks in polymer foils.
- From the Institute for Material Science of the University of Technology Darmstadt, I am grateful to Dr. G. Miehe for imaging and investigating the wires by means of TEM and SAED, to Dr. J. Brötz and Dipl.-Ing. F. Maurer for XRD measurements, and to Dr. N. Benker for EELS.
- Prof. Dr. A. Pucci, Dr. habil. G. Fahsold, and their group from the Kirchhoff-Institut für Physik of the Heidelberg University for the collaboration concerning infrared spectrosopy at ANKA.
- Dr. P.Yu. Apel from the Joint Institute for Nuclear Research in Dubna, Russia, for his support related to the etching of single latent tracks in polymer foils.
- Dr. habil. L. Gravier from the EPFL in Lausanne, Switzerland, for the collaboration with the electrical measurements as a function of magnetic fields.
- Dipl.-Phys. B. Schiedt for many fruitful discussions.

- I am grateful to the beamline scientists Dr. Y.-L. Mathis, Dr. B. Gasharova, and Dr. D. Moss for many fruitful discussions as well as to M. Süpfle for technical support at the IR beamline at ANKA.
- C. Schröder and M. Marquardt as well as E. Schubert from GSI for their technical support.
- Dipl.-Phys. K.-O. Voss for writing a LabVIEW program for cryogenic experiments.
- The whole group of the Materials Research Department of GSI for the very convenient working conditions.
- Last but not least, I would like to thank my parents and my brother for their unrestricted support during the studies as well as during my doctoral work.

REFERENCES

[1] K. Fuchs, *The conductivity of thin metallic films according to the electron theory of metals*, Proc. Cambridge Philos. Soc. 34 (1938) 100

[2] R.B. Dingle, *The elctrical conductivity of thin wires*, Proc. Roy. Soc. A 201 (1950) 545

[3] F. Patolsky, C.M. Lieber, *Nanowire nanosensors*, Materials Today (April 2005) 20

[4] M. Ding, H. Kim, A.I. Akinwande, *Observation of valence band electron emission from n-type silicon field emitter arrays*, Appl. Phys. Lett. 75 (1999) 823

[5] F. Maurer, A. Dangwal, D. Lysenkov, G. Müller, M.E. Toimil-Molares, C. Trautmann, J. Brötz, H. Fuess, *Field emission of copper nanowires grown in polymer ion-track membranes*, accepted by Nucl. Instr. and Meth. B

[6] V.B. Sandormiskiĭ, *Quantum size effects in a semimetal film*, Sov. Phys. JETP 25 (1967) 101

[7] F. Völklein, E. Kessler, *Analysis of the lattice thermal conductivity of thin films by means of a modified Mayadas-Shatzkes model: The case of bismuth films*, Thin Solid Films 142 (1986) 169

[8] M.E. Toimil Molares, A.G. Balogh, T.W. Cornelius, R. Neumann, C. Trautmann, *Fragmentation of nanowires driven by Rayleigh instability*, Appl. Phys. Lett. 85 (2004) 5337

[9] N. Garcia, Y.H. Kao, M. Strongin, *Galvanomagnetic studies of bismuth films in the quantum-size-effect region*, Phys. Rev. B 5 (1972) 2029

[10] Z. Zhang, J.Y. Ying, M.S. Dresselhaus, *Bismtuh quantum-wire arrays fabricated by a vacuum melting and pressure injection process*, J. Mater. Res. 13 (1998) 1745

[11] T.E. Huber, K. Celestine, M.J. Graf, *Magntoquantum oscillations and confinement effects in arrays of 270-nm-diameter bismuth nanowires*, Phys. Rev. B 67 (2003) 245317

[12] J. Heremans, C.M. Thrush, Y.-M. Lin, S. Cronin, Z. Zhang, M.S. Dresselhaus, J.F. Mansfield, *Bismuth nanowire arrays: Synthesis and galvanomagneitic properties*, Phys. Rev. B 61 (2000) 2921

[13] X.F. Wang, J. Zhang, H.Z. Shi., Y.W. Wang, G.W. Meng, X.S. Peng, L.D. Zhang, J. Fang, *Fabrication and temperature dependence of the resistance of single-crystalline Bi nanowires*, J. Appl. Phys. 89 (2001) 3847

[14] X.F. Wang, L.D. Zhang, J. Zhang, H.Z. Shi, X.S. Peng, M.J. Zheng, J. Fang, J.L. Chen, B.J. Gao, *Ordered single-crystalline Bi nanowire arrays embedded in nanochannels of anodic alumina membranes*, J. Phys. D: Appl. Phys. 34 (2001) 418

[15] A.J. Yin, J. Li, W. Jian, A.J. Bennett, J.M. Xu, *Fabrication of highly ordered metallic nanowire arrays by electrodeposition*, Appl. Phys. Lett. 79 (2001) 1039

[16] Y. Gao, H. Niu, C. Zeng, Q. Chen, *Preparation and characterization of single-crystalline bismuth nanowires by a low-temperature solvothermal process*, Chem. Phys. Lett. 367 (2003) 141

[17] P. Chiu, I. Shih, *A study of the size effect on the temperature-dependent resistivity of bismuth nanowires with rectangular cross-section*, Nanotechnology 15 (2004) 1489

[18] M.E. Toimil Molares, N. Chtanko, T.W. Cornelius, D. Dobrev, I. Enculescu, R.H. Blick, R. Neumann, *Fabrication and contacting of single Bi nanowires*, Nanotechnology 15 (2004) S201

[19] D.A. Glocker, M.J. Skove, *Field effect and magnetoresistance in small bismuth wires*, Phys. Rev. B 15 (1977) 608

[20] Y.-M. Lin, S.B. Cronin, J.Y. Ying, M.S. Dresselhaus, J.P Heremans, *Transport properties of Bi nanowire arrays*, Appl. Phys. Lett. 76 (2000) 3944

[21] Z. Zhang, X. Sun, M.S. Dresselhaus, J.Y. Ying, J. Heremans, *Electronic transport properties of single-crystal bismuth nanowire arrays*, Phys. Rev. B 61 (2000) 4850

[22] K. Liu, C.L. Chien, P.C. Searson, *Finite-size effects in bismuth nanowires*, Phys. Rev. B 58 (1998) 14681

[23] T.E. Huber, K. Celestine, M.J. Graf, *Magnetoquantum oscillations and confinement effects in arrays of 270-nm diameter bismuth nanowires*, Phys. Rev. B 67 (2003) 245317

[24] K. Hong, F.Y. Yang, K. Liu, D.H. Reich, P.C. Searson, C.L. Chien, F.F. Balakirev, G.S. Boebinger, *Giant positive magnetoresistance of Bi nanowire arrays in high magnetic fields*, J. Appl. Phys. 85 (1999) 6184

[25] S.B. Cronin, Y.-M. Lin, O. Rabin, M.R. Black, J.Y. Ying, M.S. Dresselhaus, P.L. Gai, J.-P. Minet, J.-P. Issi, *Making electrical contacts to nanowires with a thick oxide coating*, Nanotechnology 13 (2002) 653

[26] Y.-M. Lin, X. Sun, M.S. Dresselhaus, *Theoretical investigation of thermoelectric transport properties of cylindrical Bi nanowires*, Phys. Rev. B 62 (2000) 4610

[27] J.P. Heremans, C.M. Thrush, D.T. Morelli, M.-C. Wu, *Thermoelectric power of bismuth nanocomposites*, Phys. Rev. Lett. 88 (2002) 216801

[28] T.E. Huber, M.J. Graf, C.A. Foss Jr., P. Constant, *Thermopower of Bi nanowire array composites*, Mat. Res. Soc. Symp. 626 (2000) Z14.2.1

[29] M.R. Black, Y.-M. Lin, S.B. Cronin, O. Rabin, M.S. Dresselhaus, *Infrared absorption in bismuth nanowires resulting from quantum confinement*, Phys. Rev. B 65 (2002) 195417

[30] M.R. Black, M. Padi, S.B. Cronin, Y.-M. Lin, O. Rabin, T. McClure, G. Dresselhaus, P.L. Hagelstein, M.S. Dresselhaus, *Inter-subband transitions in bismuth nanowires resulting from quantum confinement*, Appl. Phys. Lett. 77 (2000) 4142

[31] D. Gitsu, T. Huber, L. Konopko, A. Nikolaeva, *Longitudinal magnetoresistance in single crystal wires of pure and doped bismuth in wide range of diameters*, Phys. Stat. Sol. (a) 196 (2003) 137

[32] Y.-M. Lin, M.S. Dresselhaus, *Determination of carrier density in Te-doped Bi nanowires*, Appl. Phys. Lett. 83 (2003) 3567

[33] L. Li, G. Li, Y. Zhang, Y. Yang, L. Zhang, *Pulsed electrrodeposition of large area, ordered $Bi_{1-x}Sb_x$ nanowire arrays from aqueous solutions*, J. Phys. Chem. B 108 (2004) 19380

[34] Y.-M. Lin, O. Rabin, S.B. Cronin, J.Y. Ying, M.S. Dresselhaus, *Semimetal-semiconductor transition in $Bi_{1-x}Sb_x$ alloy nanowires and their thermoelectric properties*, Appl. Phys. Lett. 81 (2002) 2403

[35] E. Ferain, R. Legras, *Track-etch templates designed for micro- and nanofabrication*, Nucl. Instr. and Meth. B 208 (2003) 115

[36] C.R. Martin, *Nanomaterials: A membrane-based synthetic approach*, Science 266 (1994) 1961

[37] M.E. Toimil Molares, V. Buschmann, D. Dobrev, R. Neumann, R. Scholz, I.U. Schuchert, J. Vetter, *Single-crystalline copper nanowires produced by electrochemical deposition in polymeric ion track membranes*, Adv. Mat. 13 (2001) 62

[38] C.E. Mortimer, *Chemie – Das Basiswissen der Chemie*, Georg Thieme-Verlag Stuttgart, 5. Auflage, 1987

[39] P. de Marcillac, N. Coron, G. Dambier, J. Leblanc, J.-P. Moalic, *Experimental detection of a-particles from the radioactivce decayof natural bismuth*, Nature 422 (2003) 876

[40] P. Hofmann, *The surfaces of bismuth: Structural and electronic properties*, University of Aarhus (2005)

[41] H. Stöcker, *Taschenbuch der Physik*, Verlag Harri Deutsch, 2998

[42] C.F. Gallo, B.S. Chandrasekhar, P.H. Sutter, *Transport properties of bismuth single crystals*, J. Appl. Phys. 34 (1962) 144

[43] A.F. Mayadas, M. Shatzkes, *Electrical-resistivity model for polycrystalline films: the case of arbitrary reflection at external surfaces*, Phys. Rev. B 1 (1970) 1382

[44] R.T. Isaacson, G.A. Williams, *Alfvén-wave propagation in solid-state plasmas. III. Quantum oscillations of the Fermi surface of bismuth*, Phys. Rev. 185 (1969) 682

[45] C.A. Hoffman, J.R. Meyer, F.J. Bartoli, A. DiVenere, X.J. Yi, C.L. Hou, H.C. Wang, J.B. Ketterson, G.K. Wong, *Semimetal-tosemiconductor transition in bismuth thin films*, Phys. Rev. B 48 (1993) 11431

[46] Yu.F. Komnik, E.I. Bukhshtab, Yu.V. Nikitin, V.V. Andrievskii, *Features of temperature dependence of the resistance of thin bismuth films*, Sov. Phys. JETP 33 (1971) 364

[47] H.J. Goldsmid, *Thermoelectric Refrigeration*, Plenum New York (1964)

[48] J.P. Heremans, C.M. Thrush, D.T. Morelli, M.-C. Wu, *Thermoelectric power of bismuth nanocomposites*, Phys. Rev. Lett. 88 (2002) 216801

[49] W. Demtröder, *Experimentalphysik 3 – Kern-, Teilchen- und Astrophysik*, Springer-Verlag Berlin Heidelberg (1998)

[50] R.L. Fleischer, P.B. Price, R.M. Walker, *Nuclear tracks in solids – principles & applications*, University of California Press (1975)

[51] www.srim2003.org

[52] Y. Sun, Z. Zhu, Z. Wang, Y. Jin, J. Liu, M. Hou, Q. Zhang, *Swift heavy ion induced amorphisation and chemical modification in polycarbonate*, Nucl. Instr. and Meth. B 209 (2003) 188

[53] F. Dehaye, E. Balanzat, E. Ferain, R. Legras, *Chemical modifications induced in bisphenol A polycarbonateby swift heavy ions*, Nucl. Instr. and Meth. B 209 (2003) 103

[54] D. Albrecht, P. Armbruster, R. Spohr, M. Roth, K. Schaupert, H. Stuhrmann, *Small angle scattering from oriented latent nuclear tracks*, Nucl. Instr. and Meth. B 2 (1984) 702

[55] V. Picq J.M. Ramillon, E. Balanzat, *Swift heavy ions on polymers: Hydrocarbon gas release*, Nucl. Instr. and Meth. B 146 (1998) 496

[56] N. Chtanko, M.E. Toimil Molares, Th. Cornelius, D. Dobrev. R. Neumann, *Etched single-ion-track templates for single nanowire synthesis*, J. Phys. Chem. B 108 (2004) 9950

[57] P.Yu. Apel, A.P. Akimenko, I.V. Blonskaya, T. Cornelius, R. Neumann, R. Spohr, K. Schwartz, C. Trautmann, *Etching of nanopores in polycarbonate irradiated with swift heavy ions at 15 K*, Nucl. Instr. and Meth. B 245 (2006) 284

[58] D.H. Francisco, L. Vanni, O.A. Bernaola, G. Saint Martin, A. Filevich, *Radial variation of track damage in polycarbonate*, Nul. Instr. and Meth. B 218 (2004) 461

[59] F. Petersen, W. Enge, *Energy loss dependent transversal etching rates of heavy ion tracks in plastic*, Rad. Meas. 25 (1995) 43

[60] E. Ferain, R. Legras, *Track-etched membrane: dynamics of pore formation*, Nucl. Instr. and Meth. B 84 (1994) 331

[61] P.Yu. Apel, I.V. Blonskaya, A.Yu. Didyk, S.N. Dimitriev, O.L. Orelovitch, D. Root, L.I. Samoilova, V. Vutsadakis, *Surfactant-enhanced control of track-etch pore morphology*, Nucl. Instr. and Meth. B 179 (2001) 55

[62] D. Fink, K.K. Dwivedi, M. Müller, S. Ghosh, V. Hnatowicz, J. Vacik, J. Cervena, *On the penetration of etchant into tracks in polycarbonate*, *Radiat*. Meas. 32 (2000) 307

[63] D. Dobrev, R. Neumann, *Electrodeposition of Bi single crystals in pores of polymer ion track membranes*, GSI Scientific Report 2002 (2003) 147

[64] Gmelin, *Handbuch der anorganischen Chemie – Wismut, Ergänzungsband*, Springer-Verlag Berlin Heidelberg, 8. Auflage (1974)

[65] M. Paunovic, M. Schlesinger, *Fundamentals of electrochemical deposition*, Wiley-Interscience (1998)

[66] J.-C. Puippe, F. Leaman, *Theory and practice of pulse plating*, American Electroplaters and Surface Finishers Society (1986)

[67] N. Chtanko, M.E. Toimil-Molares, T.W. Cornelius, D. Dobrev, R. Neumann, *Ion-track based single-channel templates for single-nanowire contacting*, Nucl. Instr. and Meth. B 236 (2005) 103

[68] T.W. Cornelius, J. Brötz, N. Chtanko, D. Dobrev, G. Miehe, R. Neumann, M.E. Toimil Molares, *Controlled fabrication of poly- and single-crystalline bismuth nanowires*, Nanotechnology 16 (2005) S246

[69] M.E. Toimil Molares, J. Brötz, V. Buschmann, D. Dobrev, R. Neumann, R. Scholz, I.U. Schuchert, C. Trautmann, J. Vetter, *Etched heavy ion tracks in polycarbonate as templates for copper nanowires*, Nucl. Instr. and Meth. B 185 (2001) 192

[70] STOE Peak File C85-1330.pks

[71] M. Gurvitch, *Resistivity anomaly in thin Bi wires: Possibility of a one-dimensional quantum size effect*, J. Low Temp. Phys. 38 (1980) 777

[72] M.R. Black, P.L. Hagelstein, S.B. Cronin, Y.M. Lin, M.S. Dresselhaus, *Optical absorption from indirect transition in bismuth nanowires*, Phys. Rev. B 68 (2003) 235417

[73] R. Hartman, *Temperature dependence of the low-field galvanomagnetic coefficients of bismuth*, Phys. Rev. 181 (1969) 1070

[74] R.T. Bate, N.G. Einspruch, *Galvanomagnetic studies of Sn-doped Bi. I. Positive Fermi energies*, Phys. Rev. 153 (1967) 796

[75] R.T. Isaacson, G.A. Williams, *Alfvén-wave propagation in solid-state plasmas. III. Quantum oscillations of the Fermi surface of bismuth*, Phys. Rev. 185 (1969) 682

[76] J.P. Omaggio, J.R. Meyer, C.A. Hoffmann, A. DiVenere, X.J. Yi, C.L. Hou, H.C. Wang, J.B. Ketterson, G.K. Wong, J.P. Heremans, *Magneto-optical determination of the T-point energy gap in bismuth*, Phys. Rev. B 48 (1993) 11439

[77] C. Kittel, *Einführung in die Festkörperphysik*, Müchen; Wien: Oldenbourg (2002)

[78] V. Damodara Das, N. Soundararajan, *Size and temperature effects on the Seebeck coefficient of thin bismuth films*, Phys. Rev. B 35 (1987) 5990

[79] B. Lax, J.G. Mavroides, H.J. Zeiger, R.J. Keyes, *Infrared magneotreflection in bismuth. I. High fields*, Phys. Rev. 5 (1960) 241

[80] *http://ankaweb.fzk.de*

[81] T.W. Cornelius, M.E. Toimil-Molares, R. Neumann, G. Fahsold, R. Lovrincic, A. Pucci, S. Karim, *Quantum size effects manifest in infrared spectra of single bismuth nanowires*, Appl. Phys. Lett. 88 (2006) 103114

[82] S. Takaoka, K. Murase, *Studies of far-infrared properties of thin bismuth films on BaF_2 substrate*, J. Phys. Soc. Japan 54 (1985) 2250

[83] M. Hengsberger, P. Segovia, M. Garnier, D. Purdie, Y. Baer, *Photoemission study of the carrier bands in Bi(111)*, Eur. Phys. J. B 17 (2000) 603

[84] S. Agergaard, Ch. Søndergaard, H. Li, M.B. Nielsen, S.V. Hoffmann, Z. Li, Ph. Hofmann, *The effectof reduced dimensionality on a semimetal: the electronic structure of the Bi(110) surface*, New Journal of Physics 3 (2001) 15

[85] V. N. Lutskii, L. A. Kulik, *Features of optical characteristics of bismuth films under conditions of quantum size effect*, JETP Lett. 8 (1968) 80

[86] W.S. Boyle, K.F. Rodgers, *De Haas-van Alphen type oscillations in the infrared transmission of bismuth*, Phys. Rev. Lett. 2 (1959) 338

[87] R.F. Egerton, *Electron energy-loss spectroscopy in the electron microscope*, Plenum Publishing Corporation, second edition (1996)

[88] C. Wehenkel, B. Gauthé, *Electron energy loss spectra and optical constants of bismuth*, Solid State Communications 15 (1974) 555

[89] C.C. Ahn, O.L. Krivanek, *EELS-Atlas*, Gatan Inc. (1982) Pleasanton, USA

[90] P. Zacharias, *Bestimmung optischer Konstanten von Wismut im Energiebereich von 2 bis 40 eV aus Elektronen-Energieverlustmessungen*, Optics Communications 8 (1973) 142

[91] M.S. Sander, R. Gronsky, Y.M. Lin, M.S. Dresselhaus, *Plasmon excitation modes in nanowire arrays*, J. Appl. Phys. 89 (2001) 2733

[92] Yu.F. Komnik, V.V. Andrievskii, *Kinetic properties of bismuth thin films*, Sov. J. Low Temp. Phys. 1 (1975) 51

[93] P.J. Price, *Anisotropic conduction in solids near surfaces*, IBM Res. Dev. J. 4 (1960) 152

[94] F.S. Ham, D.C. Mattis, *Electrical properties of thin-film semiconductors*, IBM Res. Dev. J. 4 (1960) 143

[95] J.E. Parrott, *A new theory of the size effect in electrical conduction*, Proc. Phys. Soc. 85 (1965) 1143

[96] M. Barati, E. Sadeghi, *Study of ordinary size effect in the electrical conductivity of Bi nanowires*, Nanotechnology 12 (2001) 277

[97] L. Shubnikow, W.J. de Haas, *Die Abhängigkeit des elektrischen Widerstandes von Wismutheinkristallen von der Reinheit des Metalles*, Proc. Acad. Sci. Amst. 327 (1930) 33

[98] K. Liu, C.L. Chien, P.C. Searson, K. Yu-Shang, *Structural and magneto-transport properties of electrodeposited bismuth nanowires*, Appl. Phys. Lett. 73 (1998) 1436

[99] T.W. Cornelius, *Herstellung und Charakterisierung von Wismut-Nanodrähten*, Diploma thesis, University of Heidelberg (2003)

[100] M. Thier, *Aufbau eines Rastertunnelmikroskops zum Betrieb im Ultrahochvakuum bei variablen Temperaturen bis 4.2 K*, Dissertation, University of Heidelberg (1996)

[101] C. Durkan, M.E. Welland, *Size effects in the electrical resistivity of polycrystalline nanowires*, Phys. Rev. B 61 (2000) 14215

[102] W. Steinhögl, G. Schindler, G. Steinlesberger, M. Engelhardt, *Size-dependent resistivity of metallic wires in the mesoscopic range*, Phys. Rev. B 66 (2002) 75414

[103] N. Thompson, *Electrical resistance of bismuth alloys*, Proc. Roy. Soc. A 155 (1936) 111

[104] B. Abeles, S. Meiboom, *Galvanomagnetic effects in bismuth*, Phys. Rev. 101 (1956) 544

[105] D.L. Partin, J. Heremans, D.T. Morelli, C.M. Thrush, C.H. Olk, T.A. Perry, *Growth and characterization of epitaxial bismuth films*, Phys. Rev. B 38 (1988) 3818

[106] W. Greulich (Hrsg.), *Lexikon der Physik*, Spektrum Akademischer Verlag GmbH Heidelberg (1998)

[107] R.G. Chambers, *The anomalous skin effect*, Proc. Roy. Soc. London A 215 (1952) 481

[108] G.E. Smith, *Anomalous skin effect in bismuth*, Phys. Rev. 115 (1959) 1561

[109] A.N. Friedman, S.H. Koenig, *Size effects for conduction in thin bismuth crystals*, IBM Res. Dev. J. 4 (1969) 158

[110] M.P. Vecchi, M.S. Dresselhaus, *Temperature dependence of the band paramters of bismuth*, Phys. Rev. B 10 (1974) 771

[111] R.G. Chambers, *The conductivity of thin wires in a magnetic field*, Proc. Roy. Soc. A 202 (1950) 378

[112] R.N. Zitter, *Small-field galvanomagnetic tensor of bismuth at 4.2 K*, Phys. Rev. 127 (1962) 1471

[113] F.Y. Yang, K. Liu, C.L. Chien, P.C. Searson, *Large magnetoresistance and finite-size effects in electrodepoisted single-crystal Bi thin films*, Phys. Rev. Lett. 82 (1999) 3328